

## Durham E-Theses

---

# *Use of Graded Laser Scanning to Generate Efficient Boundary Element Meshes*

BINGRU YANG

### How to cite:

---

YANG, BINGRU (2011) Use of Graded Laser Scanning to Generate Efficient Boundary Element Meshes. Masters thesis, Durham University.

### Use policy

---

The full-text may be used and/or reproduced, and given to third parties in any format or medium, without prior permission or charge, for personal research or study, educational, or not-for-profit purposes provided that:

- a full bibliographic reference is made to the original source
- a <https://etheses.durham.ac.uk/id/eprint/887/> is made to the metadata record in Durham E-Theses
- the full-text is not changed in any way

The full-text must not be sold in any format or medium without the formal permission of the copyright holders.

Please consult the [full Durham E-Theses policy](#) for further details.

# **Use of Graded Laser Scanning to Generate Efficient Boundary Element Meshes**

**Bing Ru Yang**

A thesis submitted for the degree of  
Master of Science



School of Engineering and Computing Sciences  
University of Durham

2011

# **Use of Graded Laser Scanning to Generate Efficient Boundary Element Meshes**

Bing Ru Yang

School of Engineering and Computing Sciences, Durham University

A thesis submitted for the degree of Master of Science

2011

## **Abstract**

This thesis presents an approach which combines a reverse engineering technique with boundary element stress analysis, by generating a graded mesh to improve the simulation efficiency. A rectangular metal plate, a bar of a circular cross section, a gas turbine blade and a steam turbine blade were scanned at different resolutions using a (non-contact) laser scanner measurement to obtain the point clouds. Meshes of each object were generated in Rapidform and directly used in a boundary element stress analysis. In addition, the steam turbine blade was scanned using different scanning resolutions. From this, a graded mesh model of the blade was generated and then efficient boundary element stress analyses were performed. An application of a freeform surface reconstruction of a blade surface is also given. Also, several Matlab programs were written to repair the edges and the cylindrical surface of the meshes.

Key works: reverse engineering, laser scanning, freeform surface reconstruction, graded mesh generation, boundary element stress analysis, RE and BEM integration.

## **Declaration**

The work in this thesis is based on research carried out in the Mechanics Group, School of Engineering and Computing Sciences, United Kingdom. No part of this report has been submitted elsewhere for any other degree or qualification and it is all my own work unless referenced to the contrary in the text. Part of the work has appeared in the following publication:

Yang, B. R., Wang, Q., Trevelyan, J. and Crouch, R. S. (2010). An application of freeform surface modelling by laser scanning technique and reverse engineering. *Proc. 8th International Conference on Manufacturing Research*, pp: 192-197, ed. V.I. Vitanov and D. Harrison.

**Copyright © 2011 by Bing Ru Yang.**

“The copyright of this thesis rests with the author. No quotations from it should be published without the author’s prior written consent and information derived from it should be acknowledged”.

# Acknowledgements

This is my opportunity to say a few words of thanks to all the people have helped and supported me throughout my thesis.

Firstly many thanks must give to my supervisors Prof Jon Trevelyan, Prof Roger Crouch and Dr Qing Wang who brought support, advice, enthusiasm and vast experience to this research. I am very grateful for Jon's help on the boundary element method, BEASY code and simulation results. Special thanks also give to Roger especially for seeing the project through to the end, helpful discussion on the stress analysis result and giving comments on the works. I also would to thank Qing for her advice and help on the measurement technique.

Thanks also give to: Prof Valentin Vitanov for his caring about this project; Dr Grant Ingram and Dr Simon Hogg for their support on the measurement component and CFD knowledge; Colin, Lee and Phillip in the mechanical workshop for their helps on the equipment and produced rapid prototyped models; Paul form Metris UK for his delivering measurement technique at the beginning of the project.

I also would like to thank all my friends in Durham, thanks for their helps and spending a wonderful time together in Durham.

Last but not least, I wish to thank my parents for their love and support. Without all these people's help, this thesis would have been impossible for me.

# Contents

Abstract.....	i
Declaration.....	ii
Acknowledgements.....	iii
List of Figures.....	viii
List of Tables.....	xii
Nomenclature.....	xiii
1 Introduction and Structure of the Thesis.....	1
1.1 Introduction.....	1
1.2 Structure of the Thesis.....	2
2 Literature Review.....	5
2.1 Review of Reverse Engineering Technique.....	5
2.1.1 Measurement Technique.....	7
2.1.2 Polygon Mesh Generation.....	10
2.1.3 Segmentation and Surface Fitting.....	11
2.2 Review on Computational Stress Analysis Technique.....	12
2.3 Integration of Reverse engineering, CAD and FEM/BEM.....	13
3 Theory.....	15
3.1 Boundary Element Method.....	15
3.1.1 Boundary Integral Equation.....	15
3.1.2 The Fundamental Solution.....	18
3.1.3 Shape Functions.....	19
3.1.4 Matrix method.....	21

3.2	NURBS Surface .....	23
3.3	Statistics Theory for Measurement .....	24
3.3.1	Normal Distribution .....	24
3.3.2	Root Mean Square.....	25
3.3.3	Standard Deviation and Variance .....	25
4	Experimental Technique .....	27
4.1	Leica Laser Scanner .....	27
4.2	Spatial Analyzer .....	32
4.3	System Calibration .....	33
4.4	Scanning Method.....	34
4.4.1	Metrology Scan.....	34
4.4.2	Pseudo Vision Scan.....	35
4.4.3	Automatic Scan.....	36
4.5	Measurement Strategy .....	36
4.6	Point Clouds Alignment.....	40
4.7	Scan Results .....	43
5	Boundary Element Mesh Generation.....	46
5.1	Point Cloud Pre-processing.....	47
5.1.1	Noise Reduction.....	47
5.1.2	Smoothing.....	48
5.2	Meshing Strategies for Surface Representation and Boundary Element Analysis .....	50
5.2.1	Meshing for Freeform Surface Reconstruction.....	51
5.2.2	Meshing for Boundary Element Stress Analysis .....	53

5.3	Mesh Results .....	60
6	Freeform Surface Reconstruction .....	64
6.1	Freeform Surface Fitting .....	64
6.2	Accuracy Evaluation of Surface Fitting Result.....	67
6.3	Repeatability Test.....	73
7	BEASY Input File Generation.....	75
7.1	Structure of BEASY input file .....	75
7.2	Repair Solution.....	76
7.2.1	Bar of Circular Cross Section .....	77
7.2.2	Steam Turbine Blade.....	79
7.3	Boundary Conditions.....	79
7.3.1	Rectangular Metal Plate .....	79
7.3.2	Bar of Circular Cross Section .....	80
7.3.3	Steam Turbine Blade.....	81
8	Computational Boundary Element Stress Analysis .....	86
8.1	Euler-Bernoulli Beam Theory and Timoshenko Beam Theory .....	86
8.2	Rectangular Metal Plate Stress Analysis.....	87
8.2.1	Euler-Bernoulli Beam Theory.....	87
8.2.2	Boundary Element Simulation.....	88
8.3	Circular Bar stress analysis .....	91
8.3.1	Timoshenko Beam Theory.....	91
8.3.2	Boundary Element Simulation.....	92
8.4	Steam Turbine Blade Stress Analysis .....	95
8.5	Accuracy.....	99

8.5.1	Element Distortion .....	99
8.5.2	Error Estimation.....	100
8.6	Result Discussion and Conclusion.....	100
9	Conclusions and Recommendations .....	104
9.1	Conclusions .....	105
9.2	Recommendations .....	107
	References.....	108
Appendix 1	Rapidform Polygon Mesh File.....	114
Appendix 2	Matlab Code for Cylinder Repair .....	115
Appendix 3	BEASY Input File.....	120
Appendix 4	Paper Published in ICMR2010 .....	123

# List of Figures

Figure 1.1 Project framework.....	3
Figure 2.1 Reverse engineering in product design cycle.....	5
Figure 2.2 Main processes of RE.....	6
Figure 2.3 Overview RE process of turbine blade.....	6
Figure 2.4 Data capturing method.....	7
Figure 2.5 Evaluation of some measuring techniques.....	9
Figure 2.6 Schematic illustrations .....	13
a. a boundary element mesh	
b. a finite element mesh	
Figure 3.1 Dirac delta function .....	17
Figure 3.2 Local coordinate system for interpolation over the element.....	20
Figure 3.3 Control point and control polygon of a NURBS surface.....	23
Figure 4.1 Laser scanner system integration.....	29
Figure 4.2 A combination of local and reflected energy, measure $\Delta f$ instead of $\Delta t$ .....	30
Figure 4.3 Visible red laser pointing to the surface of a tooling ball.....	31
Figure 4.4 Measurement coordinates of laser scanner system.....	32
Figure 4.5 Software interface.....	33
Figure 4.6 Metrology scan within perimeter.....	35
Figure 4.7 Angle of Azimuth direction and scanning times.....	37
Figure 4.8 Modified scanning plan after considering the angle issue.....	38
Figure 4.9 Angle of Elevation direction.....	39
Figure 4.10 Fix a gas turbine using vice.....	39
Figure 4.11 Fine scan of important features.....	40
Figure 4.12 Using tooling balls as coordinate reference.....	41
Figure 4.13 Point clouds alignment for a sample turbine blade (point cloud 1 – green, point cloud 2 – orange,	

point cloud 3 – red, point cloud 4 – blue, point cloud 5 - purple).....	42
Figure 4.14 Point cloud of the rectangular metal plate (2 by 2mm grid on top and bottom surface, 1 by 1mm grid on sides).....	43
Figure 4.15 Point cloud of the bar of circular cross section (2 by 2mm grid).....	44
Figure 4.16 Point cloud of the gas turbine blade (1 by 1mm grid).....	44
Figure 4.17 Point cloud of the steam turbine blade (Graded point cloud, 1 by 1mm on the fillet, 2 by 2mm around the middle of the blade, 3 by 3mm on tip).....	44
Figure 5.1 Examples of noisy points.....	48
Figure 5.2 Smoothing of blade airfoil section.....	49
a. Original data and curvature plot	
b. Curvature plot after smoothing	
Figure 5.3 Blade point cloud after pre-processing.....	50
Figure 5.4 Meshing based on 0.5 by 0.5mm grid point cloud.....	51
a. Initial mesh	
b. 112566 poly-daces	
Figure 5.5 Meshing based on 1 by 1mm grid point cloud.....	52
a. Initial mesh	
b. 66060 poly-faces	
Figure 5.6 Meshing based on 2 by 2mm grid point cloud.....	52
a. Initial mesh	
b. Poor representation of edges	
Figure 5.7 Mesh optimization based on 0.5mm grid mesh.....	53
a. Dense mesh	
b. Adaptive mesh	
Figure 5.8 Sharp edges problem.....	54
Figure 5.9 Plane define in spatial analyzer.....	55
a. Points selection	
b. Sampling	
c. Plane definition	

Figure 5.10 Repair points on the edges.....	56
Figure 5.11 Metal plate mesh following edge repair.....	56
Figure 5.12 Meshes of Circular Bar.....	57
a. Bad mesh representation of the surface (Sparse point cloud)	
b. Good mesh representation of the cylindrical surface (Dense point cloud)	
Figure 5.13 Repaired geometry of the circular bar.....	58
Figure 5.14 Mesh based on 2 by 2mm grid point cloud.....	59
a. Initial mesh	
b. Repair defects	
c. Final blade mesh model	
Figure 5.15 Different densities of mesh.....	61
a. Rectangular metal plate	
b. Circular bar	
Figure 5.16 Final mesh models of turbine blade.....	62
Figure 5.17 Graded mesh for turbine blade.....	63
Figure 6.1 NURBS surface .....	66
a. NURBS curve representation of the blade surface	
b. NURBS surface fitting result.	
Figure 6.2 Rapid prototyped model of blade.....	66
Figure 6.3 Surface patch number effect.....	70
a. 0.5mm grid point could, 800 surface patches, 8 control points	
b. 0.5mm grid point could, 400 surface patches, 8 control points	
c. 0.5mm grid point could, 100 surface patches, 8 control points	
Figure 6.4 Control point effect.....	71
a. 0.5mm grid point cloud, 400 surface patches, 12 control points	
b. 0.5mm grid point cloud, 400 surface patches, 8 control points	
c. 0.5mm grid point cloud, 400 surface patches, 4 control points	
Figure 6.5 Dense mesh against adaptive mesh.....	72
a. Dense mesh surface fitting	
b. Adaptive mesh surface fitting	

Figure 6.6 Uniform surface patch distribution against adaptive surface patch distribution.....	72
a. Uniform surface patch	
b. Adaptive surface patch	
Figure 6.7 Deviation map between point cloud and the CAD model (5 samples).....	74
Figure 7.1 Boundary conditions for the rectangular metal plate.....	80
Figure 7.2 Boundary conditions for the bar of circular cross section.....	80
Figure 7.3 Mesh of an aerofoil.....	81
Figure 7.4 Pressure distribution.....	82
Figure 7.5 Identification for pressure and suction surfaces.....	84
Figure 7.6 Boundary conditions for the steam turbine blade.....	85
Figure 8.1 Maximum principal stress of rectangular metal plate.....	88
Figure 8.2 Maximum displacement of rectangular metal plate.....	89
Figure 8.3 Maximum principal stress of bar of a circular cross section .....	92
Figure 8.4 Maximum displacement of bar of a circular cross section .....	93
Figure 8.5 Stress distribution contours – steam turbine blade.....	96
a. 3 by 3mm grid model	
b. 2 by 2mm grid model	
c. 1 by 1mm grid model	
d. Graded 3-2-1 model	
Figure 8.6 Displacement Contours of steam turbine blade.....	97
a. 3 by 3 mm grid	
b. b. 2 by 2mm grid	
c. 1 by 1mm grid	
d. d. Graded 3-2-1 model	
Figure 8.7 Element distortion caused by very slim element geometry.....	99
Figure 8.8 Typical stress error norm plot.....	100
Figure 9.1 Process of integration of RE and BE stress analysis.....	104

## List of Tables

Table 4.1 System specification .....	28
Table 4.2 Errors during each alignment.....	42
Table 6.1 Duration of each process in the reverse engineering of turbine blade.....	67
Table 6.2 Error distribution of five scanned samples.....	74
Table 8.1 Metal plate stress analysis (288 elements).....	90
Table 8.2 Metal plate stress analysis (578 elements).....	90
Table 8.3 Metal plate stress analysis (864 elements).....	90
Table 8.4 Circular bar stress analysis (473 elements).....	93
Table 8.5 Circular bar stress analysis (657 elements).....	94
Table 8.6 Circular bar stress analysis (1505 elements).....	94
Table 8.7 Correlation check.....	97
Table 8.8 Statistics of the major factors.....	98
Table 8.9 Force balance check.....	102

## Nomenclature

$A$	Load case Area
$A$	Coefficient matrix of knowns
$a$	Angular coordinate
$B$	Load case
$B$	Coefficient matrix of knowns
$b$	Width of the plate Body forces
$c$	Distance from the neutral axis to the point
$c(p)$	Boundary dependant multiplier at a point $p$
$D_1$	Length of optical fibre
$D_2$	twice of the distance from the device to the target
$E$	Young's Modulus
$G$	Shear modulus
$g$	Known value from G matrix
$H$	Coefficient matrix of knowns
$h$	Height Known value from H matrix
$I$	Second moment area of the cross section
$i$	Direction index
$j$	Direction index
$k$	Timoshenko shear coefficient
$l$	Length

$M_{max}$	Maximum bending moment
$N_{i,p}$	Nonrational B-spline basis functions
$n$	Number of nodes
$P$	Uniformly distributed load
$p$	Source point
	Degrees of basic function
$P_j$	Corresponding pressure of a node
$P_{i,j}$	Control points form a bidirectional control grid
$q$	Degrees of basic function
$r$	Distance
	Radius of cylinder
$S$	Surface
$S(u, v)$	NURBS surface
$t$	Traction
$u$	Displacement
	Mean
	NURBS surface direction
$u(p)$	Displacement as a point $p$
$V$	Volume
$\nu$	Poisson's ratio
	NURBS surface direction
$w_{i,j}$	Weights
$\sigma$	Standard deviation
$V$	Variance
$\gamma$	Continuous variables

$\Delta(p, x)$	Dirac delta function at point $p$ in the $x$ direction
$\omega_{max}$	Maximum deflection
$\Delta f$	Frequency
$\sigma_{max}$	Maximum principal stress
$\Delta D$	Range
$\Delta t$	Time
$\theta$	Rotational angle
$\delta_{ij}$	Kronecker delta
$\vec{n}$	Normal to the surface
$\eta$	Local coordinate

# Chapter 1

## Introduction and Structure of the Thesis

### 1.1 Introduction

Engineering is the process of designing, manufacturing, assembling, and maintaining products and systems. A good engineering design plays an important role in producing a successful product. A design engineer does not only move from an initial geometric model to the physical implementation of a product, but may also want to recover the original design details from an existing product for which there is no documentation available. This process of restoring the design information of a product, and producing a computer model is known as reverse engineering (RE) [61] [1]. Recently, with the rapid development of measurement technique and digital computing, RE has become an effective tool (in terms of accuracy and speed) to meet measurement demands for parts with a complex geometry. It also plays a crucial role in reconstructing the geometry and improving the product performance during design and analysis, in areas such as automotive engineering [47], aerospace engineering [15], medical engineering [38] and bionic engineering [60].

As computational engineering analysis techniques, the finite element method (FEM) and the boundary method (BEM) have become essential tools. They have been used to solve various engineering problems in engineering fields such as aeronautical, mechanical, civil, electronics. Both techniques subdivide object into 'elements'; these are collectively known as a 'mesh'. The concept of node points is used to define the displacement in each

element. A set of simultaneous equations is constructed by collocating a Boundary Integral Equation at each node. The entire set of equations can be solved using matrix algebra. The difference between the two approaches (FEM and BEM) is that only the surface area of the object needs to be defined in BEM, but the entire volume must be defined in FEM. The boundary element method is used in this research, since the 3D meshes generated in this research are confined to the boundary surface.

The quality of the mesh of an object has a significant effect on the analysis accuracy and efficiency. Many engineering analyses require some part of a component to be modelled in detail. Nevertheless, it would be highly inefficient to model the entire component using small elements. It is desirable to mesh the model using small elements on those parts need to be detailed modelled, and use relatively large elements on those areas of less interest.

However, despite rapid development of reverse engineering and boundary element method over the last two decades, there has not been a link between these two techniques. It is argued here that linking the RE and the BEM can accelerate the engineering design and analysis process; thus a fast analysis and re-analysis of an existing product can be achieved, particular for those parts without the CAD information.

Therefore, we propose a novel study toward integration of reverse engineering based innovative design and boundary element analysis in this thesis. The information on geometry of the object and the boundary element mesh model are reconstructed using a reverse engineering technique. This mesh model is directly used in a boundary element analysis, where the CAD-to-meshing stage is omitted for saving design and analysis time. More importantly, a graded mesh model can be directly generated from the laser scanner. The computational analysis can be more efficient as a consequence of this.

## **1.2 Structure of the Thesis**

This thesis presents a study into the coupling of reverse engineering techniques with boundary element analysis using graded mesh generation in order to give an efficient

stress analysis. A turbine blade is used as a case study to demonstrate the method. An application to freeform surface reconstruction of a blade surface is also given.

The framework of this research is illustrated in Figure 1.1. First of all, objects are digitized by the laser scanning technique in order to obtain point clouds. These point clouds are imported into reverse engineering software Rapidform to produce a graded mesh generation and surface reconstruction. The mesh is exported as a polygon data file. A set of aerodynamic loads are applied as static tractions for a particular turbine blade. The loads are obtained from computational fluid dynamic (CFD) analysis using the software Fluent. Then a BEASY input file is generated and a boundary element stress analysis is performed.

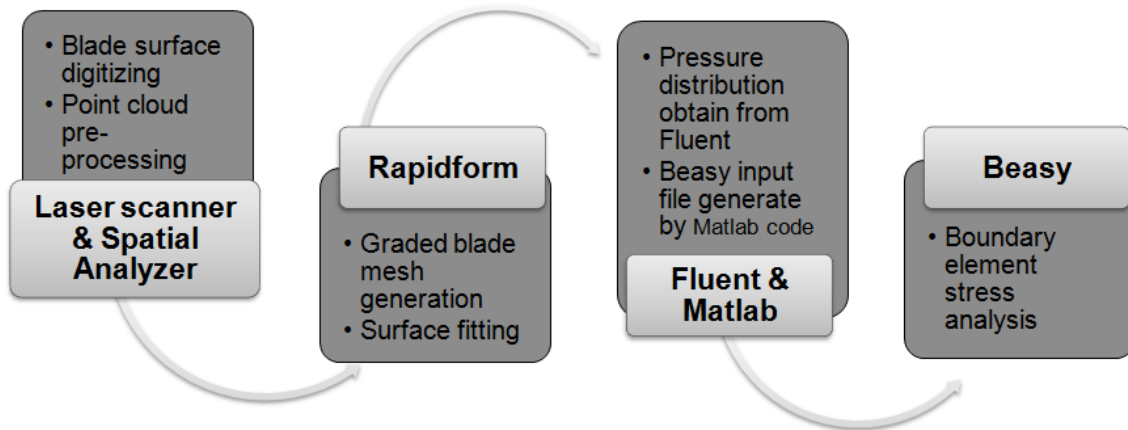


Figure 1.1 Project framework

In this thesis, literature reviews (chapter 2) are firstly given of the reverse engineering technique, including data capture methods, mesh generation and surface fitting techniques. Secondly, the computational stress analysis techniques are reviewed, including comparison between the finite element method and the boundary element method. Finally, reviews are given of earlier studies on integration of RE, CAD and FEM/BEM. Chapter 3 introduces the theories employed in this research, including an overview of the boundary element method. The laser scanner experiential measurement strategy is described, measurement setting and strategy is described in chapter 4, where the measurement results from a rectangular metal plate, a bar of a circular cross section

and two turbine blades are shown. The point cloud data are exported in an IGES file format. Chapter 5 demonstrates the mesh generation procedure for the four objects. A graded mesh model of a turbine blade is obtained. In addition, several problems are examined such as sharp edge repair. The repair algorithms are given in chapter 7 and BEASY input files are also generated using Matlab code. Chapter 6 gives a study on NURBS surface fitting for freeform application. Fitting accuracy evaluation is also included. Furthermore, repeatability of the measurement process is also discussed. Chapter 8 gives the boundary element stress analysis results for a metal plate, a bar and a steam turbine blade based on models with different grid densities. An efficient blade analysis is performed using graded mesh model. Conclusions and recommendations are finally given in chapter 9.

## Chapter 2

### Literature Review

#### 2.1 Review of Reverse Engineering Technique

Reverse engineering is an important branch of the mechanical design and manufacturing application field, and this technique has been widely recognized as a crucial step in the product design cycle. Such a cycle is illustrated in figure 2.1. The product design period and cost can be largely reduced using reverse engineering technique. Sokovic and Kopac [52] gave an explanation of the importance of reverse engineering on product development.

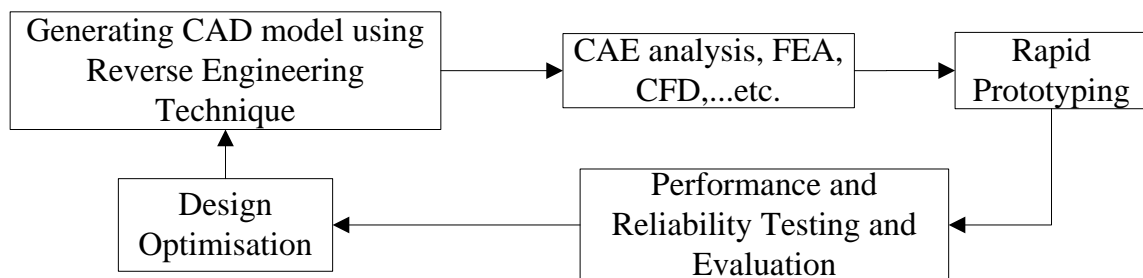


Figure 2.1 Reverse engineering in product design cycle

There are many applications of reverse engineering in the industry, such as automotive engineering [48], aerospace engineering [15], medical engineering [38] and bionic engineering [60]. It is necessary to restore the design information of a product when original documentation is not available. Recreation of a CAD model of an existing part is useful since it generates a model which can be analyzed and modified in order to construct a new improved part. In cases where a part was damaged or broken, reverse engineering can be used to recover the worn areas and reconstruct parts [24] [3].

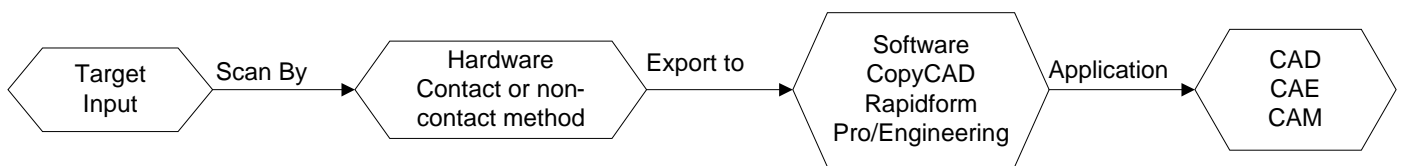


Figure 2.2 Main processes of RE

While conventional engineering transforms engineering models into real parts, in reverse engineering real parts are transformed into engineering models, and the ultimate goal is to build a complete and consistent CAD model of an object. The whole reverse engineering process is shown in figure 2.2. However, the quality of the reconstruction CAD model is strongly dependent on the data capture method and surface modelling process.

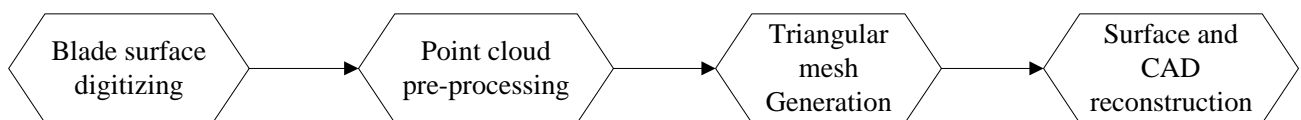


Figure 2.3 Overview RE process of turbine blade

Reverse engineering typically starts with measuring an existing part so that the surface information can be captured. These point clouds will be processing either by a bespoke

algorithm or a reverse engineering software package in order to obtain the reconstructed CAD model of the existing part, the procedure is shown in figure 2.3.

There are many reverse engineering software systems available in the market, for engineering measurement, such as Spatial Analyzer, Verisurf, Build IT, Focus Scan. For mesh generation and surface modelling, packages such as Rapidform, Imageware, Geomagic Studio, Copy CAD are available.

### 2.1.1 Measurement Technique

The first step in creating the CAD model of an existing part is surface digitizing. Data capturing is the critical part of the reverse engineering process, it directly affect the accuracy of the part model. There are many different methods for capturing the data from the part surface (as shown in figure 2.4). These methods can be divided into two types: contact type and non-contact type. In one non-contact method, light and sound are used, while the surfaces are touched by using a mechanical probe in the contact method. Jarvis [32] gave a good introduction on different methods of data acquisition. A detailed survey of optical methods for dimensional metrology was presented by Heinrich [31].

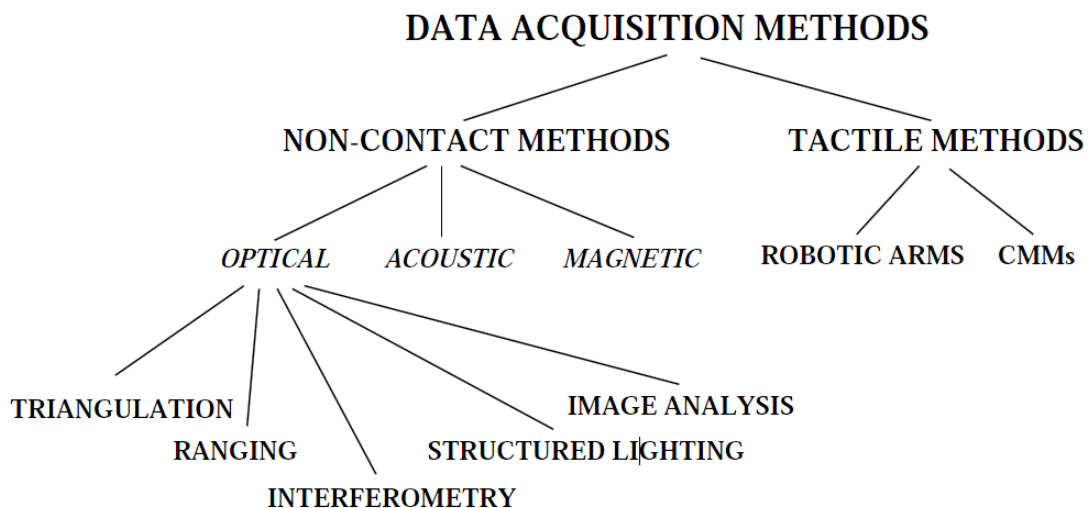


Figure 2.4 Data capturing method [56]

The tactile method, as a contact approach, uses a mechanical probe to touch a surface; the relevant location is determined by sensing devices. A Coordinate Measuring Machine (CMM) is the most widely used device for capturing the surface information of the part using this method. These machines can be programmed and follow paths along a surface to capture high accuracy results, but the low measurement speed is the main limitation of these machine. Many research works have been presented using the contact method. Lin, Wang and Dai [38] used a contact measurement method and reverse engineering technique to reconstruct the CAD model of an artificial joint in order to meet their customized demands. Structured lighting uses light source to illuminate the surface of the part in conjunction with a detector to capture the image of the light pattern on the part surface. The image must be analyzed to determine the coordinates of points on the surface. Sang's paper [47] gave a good example on structured lighting systems, the measurement procedure was optimized and a scanning case study was presented, the missing parts in the scanning were also analyzed in their work. The interferometer [11] [41] [44] method measures distances in terms of wavelengths using interference patterns. This method provides highly accurate results. Stereo scanning uses a triangulation method to find the image information. Triangulation uses high energy light sources to focus and project on the surface of interest, a video camera captures the reflection off the surface, and the position of surface point can be calculated. The triangulation method was introduced and developed in Wolf's paper [57], who investigated this method as an inspection approach for computer aided manufacturing. The laser scanning method uses a laser beam to travel along the scan path, the energy reflects back along the line of sight can be detected by the camera in order to determine the distance. The 3D coordinate value is assigned for each measured point. The laser beam is focused to the smallest possible spot by a high-speed optical device. A laser-scanning device can acquire a large amount of point data in a short time compared to a contact device. However, for measuring a point on the surface using a laser scanner, several constraints must be satisfied, these constraints were presented in Lee's paper [37]: 1. View angle constraint; 2. Field of view (FOV); 3. Depth of focus (DOF); 4. The incident beam as well as the reflected beam should not interfere with the part itself; 5. The laser probe should travel along a path that is collision free.

In addition, Xie et al [59] built a multi-probe measurement system integrated with a coordinate measuring machine (CMM), a structured-light sensor, a trigger probe and a rotary table in order to capture full data of high complex part surface.

The above mentioned measuring examples may be compared to the requirements which can be derived from the categories of part dimension, shape complexity, surface conditions and material properties such as hardness and transparency. Savio et al [49] made an evaluation of some measurement techniques, see figure 2.5.

	Laser tracker	Direct Comparison	Tactile CMM	Optical CMM	X-ray tomography	Fringe projection	Fringe reflection / Deflectometry	Photogrammetry	Interferometry	Tactile Surface topography & Profilometry	Optical Surface topography & Profilometry	Confocal Microscopy	Scanning Force Microscopy
<i>Part dimensions</i>													
large	●	◐	●	●		◐		●	◐				
medium	●	◐	●	●		◐		●	◐				
small		●	●	●	●	●	●	●	●	◐	◐	◐	
micro			◐	◐	●	◐	◐		●	●	●	●	◐
<i>Shape complexity</i>													
low	●	●	●	●	●	●	●	●	●	●	●	●	●
medium	◐	◐	●	●	●	◐		◐		◐	◐	◐	◐
high	◐		◐	◐	●								
<i>Material and surface</i>													
hard, not sensitive	●	●	●	●	●	●	●	●	●	●	●	●	●
deformable	●	◐	◐	●	●	●	●	●	◐	◐	●	●	●
specular	●	●	●				●		●	●		◐	●
transparent	●	◐	●		●			●		●		◐	●
opaque	●	●	●	●	●	◐	◐	●	●	●	●	●	●
<i>Traceability</i>													
	◐	◐	●	◐	◐	◐	◐	◐	●	●	◐	◐	●

Legend:	full match:	●
	little match:	◐

Figure 2.5 Evaluation of some measuring techniques [49]

### 2.1.2 Polygon Mesh Generation

Once a point cloud of an object has been collected, the next step is to create a mesh to represent the surface. For a polygon mesh, the points from the pre-processing stage are joined together to form a triangular mesh. Hoppe et al.[28] first addressed this topic for the general case of an unorganized point cloud. Since then, many researchers have presented their solutions. A survey was presented by Campbell and Flynn [12]. The Delaunay triangulation [7] [16] [42] [61] is best known among them. The Delaunay triangulation can be applied by using the Voronoi and the circumcircle approaches. The first approach begins with generating the Voronoi diagram which is also known as Dirichlet tessellation or Thiessen tessellations of the points acquired. The Voronoi diagram will have only one point in the middle of each polygon. The Delaunay triangulation is then created by connecting all points. In the circumcircles approach, circumcircles that do not contain any other points in their interior are created through three points. The Delaunay triangulation is then created by joining the three points from the circumcircles. Other approaches for 3D triangulation of a given point cloud have also been developed, such as volume based approach [10] and surface-based approach [42].

However, when scanning a complex shaped object for the data acquisition, it may sometime miss out some part of the object. These missing data lead to holes and overlaps. One of the available solutions to solve this problem was presented by Jun [34]. He proposed a methodology that can be used to fill the holes automatically in a piecewise manner. Other researchers also have developed surface based [8] and volumetric based [22] mesh reconstruction algorithms to deal with the factors of topology, overlap, and missing data in 3D application. Related work on mesh optimization can be found in Schroeder [50] and Hoppe [29]. An approximating polyhedral approach using 3D  $\alpha$ -shapes to capture the topological structure before surface fitting has been proposed by Guo [27].

Since the polygon mesh is shown in the form of facets in software used in this research, a stereolithography (STL) file format is used as a standard file for rapid prototyping. Typically, the STL format contains only the coordinates of triangle vertices and the normals of triangle facets. Liu et al [39] employed the STL format in their work

for integrating a system of cross sectional imaging based reverse engineering and rapid prototyping for reproducing complex objects.

### **2.1.3 Segmentation and Surface Fitting**

Segmentation partitions the original point set into patches, one for each natural surface, so that each patch contains just those points sampled from a particular natural surface. A summary of segmentation techniques can be found in [43]. There are two different methods that can be used for segmentation: face-based [9] and edge-based methods [51]. A face-based method connects regions of points with similar properties as belonging to the same surface patch. For example, a group of points having the same normal (using the normal to the triangles) belong to the same plane. Then, the edges (boundary) of the patch can be derived by intersection from the surface patches. In edge – based methods, boundaries are determined in the point data representing edges (either sharp or smooth) between surface patches. For instance, if sharp edges are being sought, places where the normal of surface patch estimated from the point data suddenly change direction are identified. If smooth edges (tangent-continuous) are being considered, places where surface curvatures or other higher derivatives have discontinuity are identified.

To fit standard engineering surfaces (analytical surfaces) such as cylinder, conical and others, implicit polynomial functions are used. In order to model freeform surfaces, parametric representations such as NURBS, B-spline and Bezier surfaces are used[43]. However, Tai [54] explained that the local control of surface shape is not possible for Bezier surface. The availability of the surface fitting optimization is limited, since a control point cannot be added without increasing the degree of the surface. Therefore B-spline and NURBS have been the standard for representing free-form surfaces in current commercial CAD systems. Lin et al[39] employed an existence B-Splines surface fitting as comparison to their method, i.e. surface lofting method. Their method begins with fitting each row of data points to obtained B-spline curves and then the section curves are fitted into a lofted surface. More recently, Chivateet al [18] employed NURBS surface

fitting using a least squares data approximation method. The NURBS surface fitting technique has been widely used in current commercial reverse engineering software.

## **2.2 Review on Computational Stress Analysis Technique**

As computational engineering analysis techniques, the finite element method (FEM) and the boundary method (BEM) have become essential tools in engineering analysis. They have been used to solve various engineering problems in wide areas, such as aeronautical, mechanical, civil, electronics.

The finite element method (FEM) was first used in aerospace engineering [55]. In 2D engineering analysis, FEM can be applied to analyze structures with 2D plane symmetry [20]. It eliminates the use of complicated experimental methods. In 3D analysis, FEM allows researchers to perform stress analysis on complicated geometries and provides a more detailed evaluation of the complete state of stress in the structures [2]. With the rapid development of this technique, many commercial softwarepackages have becomes available. The application of FEA has been extended to heat transfer, vibrations, acoustics, electromagnetics and many others.

As the alternative method, the boundary element method was firstly used to solve the elasticity problem by discretization procedures by Fredholm [25]. However, his work was limited by lack of computing speed. Since the development of the computing technology, a number of technical papers appeared in the 1960's. Jaswon [33] and Symm [53] solved the Fredholm equations using a collocation procedure for simple 2D potential flow problems. Hess and Smith looked at boundary integral methods for solving potential flow problem for general geometries. Their works also extended to elasticity problems in the 1960's. The first paper to use the direct approach of using displacements and tractions in an integral equation applicable over the boundary was published by Rizzo [46] in 1967. Then Cruse [21] extended the direct integral equation approach to 3D problem. The concept of higher-order elements using quadratic shape functions was first used by Lachat in 1976. The first text book describing the newly named *Boundary Element*

*Method* by Brebbia [6] was published in 1978. Commercial software based on the BEM appeared in the 1980's. Danson et al [23] first described the BEASY system.

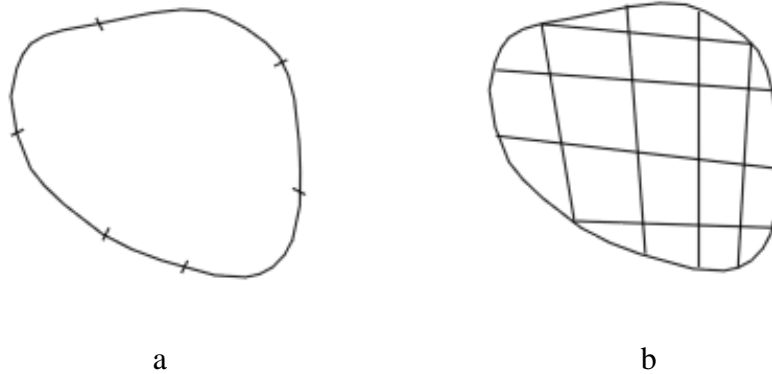


Figure 2.6 Schematic illustrations of (a) a boundary element mesh and (b) a finite element mesh

There are also many works on comparison between the FEM and BEM. Cha et al [14] presented a study on comparison of convergence and modelling time for tube stress analysis with the FEM and BEM. There are some advantages using boundary elements. 1. Since the BEM only requires mesh on the boundary (meshes for FEM and BEM are shown in figure 2.6), it requires less data preparation time than FEM. The re-mesh is also easier and faster. 2. Stresses are accurate because no further approximation is imposed on the solution at the interior points. 3. For the same level of accuracy, the BEM uses a smaller number of nodes and elements, which leads to less computer time and storage. 4. The BEM is easy applicable to incompressible materials. However, the difficulty of handling non-linear problems is the biggest disadvantage of the BEM.

### **2.3 Integration of Reverse engineering, CAD and FEM/BEM**

The approach of integrating CAD and FEM/BEM can accurately capture the object geometry of object and simplify mesh refinement by eliminating the need for communication with the CAD geometry once the initial mesh is constructed. The

integration approach of RE and FEA/BEM can reconstruct the CAD model of existing parts for fast engineering analysis purpose.

Recently, several researchers have presented works on the integration of CAD and FEM or BEM. Hughes et al [30] proposed the concept of NURBS – based isogeometric analysis which integrates CAD and finite element analysis. Cervera and Trevelyan [13] have implemented evolutionary structural optimization based on NURBS representation using the boundary element method.

More recently, a few initial studies of applications on combining reverse engineering and finite element method have become available. Goh et al [26] developed an integrated CAD–FEA process for below-knee prosthetic sockets. Kubiak et al [35] employed reverse engineering and FEA to analyze failure of the steam turbine root. In this work, the geometry of the blade was measured and reconstructed using CMM and a finite-element analysis (FEA) of the blade group model was carried out to calculate the natural frequencies. Cheng et al [17] studied the effect of high-performance polyethylene (HPPE) fibres on stress distributions in a maxillary denture and the influence of fibre position on improving denture performance. A denture was scanned by a 3D Advanced Topometric Sensor digitizing system, the model was reconstructed using Rapidform. Then a finite element stress concentration analysis was performed using ABAQUS. However, there are no RE and BEM integration studies presented at the moment.

## **Chapter 3**

### **Theory**

This chapter provides an introduction to the theory of the Boundary Element Method, surface fitting techniques and of measurement techniques.

### **3.1 Boundary Element Method**

The Boundary Element Method is a widely used technique for the solution of partial differential equations. While its use is common in a variety of engineering problems, including heat transfer, electrostatics, electromagnetics and acoustics, the focus in this work is on its use in elastostatics.

#### **3.1.1 Boundary Integral Equation**

The reciprocal theorem developed by Betti is here used to derive the boundary element method for stress analysis. The reciprocal theorem states that, for any two possible loading conditions which are applied independently to a structure such that it remains in equilibrium, the work done by taking the forces from the first load case and the displacements from the second load case is equal to the work done by the forces from the

second load case on the displacement from the first load case. If the two loading conditions are called condition A and B:

$$Forces(A) \times Displacements(B) = Forces(B) \times Displacements(A) \quad (3.1)$$

The reciprocal theorem can be applied to a general structure under the load cases  $(t, u, b)$  and  $(t^*, u^*, b^*)$ , where  $t$  is the traction,  $u$  is the displacement and  $b$  is the body force. The work done by the surface tractions  $t$  will be integral of the traction multiplied by the displacement term  $u^*$  from the complementary load case  $(t^*, u^*, b^*)$ . The integral of traction is the value of the force applied by the tractions, and the force times the displacement gives a work term. However, this integral only needs to be calculated over the surface  $S$  since this is the only the place that the traction can be applied.

To calculate the work done by the body forces, it is necessary to integrate the body forces  $b$  multiplied by the complementary displacement  $u^*$  across the whole volume.

Thus, the work done by the forces on the first load case on the displacements of the complementary load case can be written as (the same for the forces on the second load case on the displacements):

$$work = \int_S t^* u dS + \int_V b^* u dV = \int_S u^* t dS + \int_V u^* b dV \quad (3.2)$$

where we denote with  $S$  and  $V$  the surface and volume, respectively, of the subject under analysis.

In order to simplify the equation, it will be assumed that there are no body forces in the first load case ( $b = 0$ ):

$$\int_S t^* u dS + \int_V b^* u dV = \int_S u^* t dS \quad (3.3)$$

The load case  $(t^*, u^*, b^*)$  has not been defined so far. By choosing a suitable load case we can make the equation simpler. The complementary load case is chosen hereto to be a type of point force. The form the point force takes is a Dirac delta function (figure 3.1).

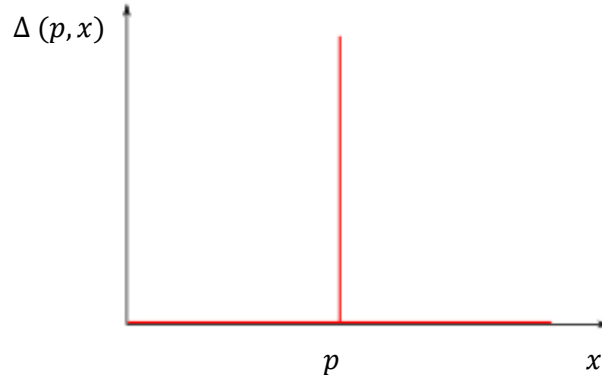


Figure 3.1 Dirac delta function

The Dirac delta function can be considered to be an infinite point load acting over an infinitesimally small area. Mathematically the Dirac delta function is given by

$$\Delta(p, x) = \begin{cases} 0 & x \neq p \\ \infty & x = p \end{cases} \quad (3.4)$$

$$\int_{-\infty}^{\infty} \Delta(p, x) dx = 1 \quad (3.5)$$

Since the complementary load case includes no body forces other than the fictitious point force inside the material, (3.3) can be rewritten as:

$$\int_s t^* u dS + \int_v \Delta(p, x) u dV(x) = \int_s u^* t dS \quad (3.6)$$

Also, since the integral of the delta function is 1, and calling that the value of the displacement  $u$  at  $p$  can be written  $u(p)$ , (3.6) can be reduced to

$$\int_S t^* u dS + u(p) = \int_S u^* t dS \quad (3.7)$$

Now, the only term left in the equation which contains a term not confined to the boundary  $S$  is the second term – the displacement in the real load case at the point at which we choose to apply the point force in the complementary load case. However, we can make (3.7) relate to the boundary by stipulating that the point  $p$  lies somewhere on the boundary. While this is helpful in giving us a boundary – only integral equation it introduces complications in that the integrals become singular. In particular the first term in (3.7) has a strong singularity requiring careful treatment. As part of this treatment we include a scalar multiplier  $c(p)$ , rewriting our integral equation as:

$$\int_S t^* u dS + c(p)u(p) = \int_S u^* t dS \quad (3.8)$$

The value that  $c(p)$  takes lies between 1 and 0. When  $c(p) = 1$ , the point force is inside the material. When  $c(p) = 0$ , the point force is outside the material and there is no force effect. On a smooth surface,  $c(p) = 0.5$ .

### 3.1.2 The Fundamental Solution

The fundamental solution due to Kelvin describes the displacement and traction fields  $(t^*, u^*)$  in infinite material as a result of the applied load in the form of a Dirac delta function. For 2D problems,

$$u_{ij}^* = \frac{1}{8\pi\mu(1-\nu)} \left[ (3-4\nu) \ln \frac{1}{r} \delta_{ij} + \frac{\partial r}{\partial x_i} \frac{\partial r}{\partial x_j} \right] \quad (3.9)$$

and for a 3D problem:

$$u_{ij}^* = \frac{1}{16\pi\mu(1-\nu)r} \left[ (3-4\nu)\delta_{ij} + \frac{\partial r}{\partial x_i} \frac{\partial r}{\partial x_j} \right] \quad (3.10)$$

where  $\mu$  is the material shear modulus,  $\nu$  is the Poisson's ratio, indices defining  $i$  and  $j$  are the directions of the applied force at the  $p$  and the required displacement at  $y$ , and  $r$  is the distance between the source point  $p$  and the field point  $y$ .  $\delta_{ij}$  is called the Kronecker delta which takes the values zero if  $i \neq j$ , and 1 if  $i = j$ .

The fundamental solutions for traction components are more complicated; for a 2D problem, they are given by:

$$t_{ij}^* = \frac{-1}{4\pi(1-\nu)r} \frac{\partial r}{\partial \vec{n}} \left[ (1-2\nu)\delta_{ij} + 2 \frac{\partial r}{\partial x_i} \frac{\partial r}{\partial x_j} \right] + \frac{1-2\nu}{4\pi(1-\nu)r} \left[ \frac{\partial r}{\partial x_j} n_i - \frac{\partial r}{\partial x_i} n_j \right] \quad (3.11)$$

and for a 3D problem:

$$t_{ij}^* = \frac{-1}{8\pi(1-\nu)r^2} \frac{\partial r}{\partial \vec{n}} \left[ (1-2\nu)\delta_{ij} + 2 \frac{\partial r}{\partial x_i} \frac{\partial r}{\partial x_j} \right] + \frac{1-2\nu}{4\pi(1-\nu)r} \left[ \frac{\partial r}{\partial x_j} n_i - \frac{\partial r}{\partial x_i} n_j \right] \quad (3.12)$$

where  $\vec{n}$  is the outward pointing normal to the surface.

### 3.1.3 Shape Functions

The nodes play a crucial role in the analysis as these nodes define the geometry of the element, and they also define the traction, displacement and demonstrate the stress variation over the element. The displacement and stress at any other point on the element can be found by interpolating from the nodes using shape function.

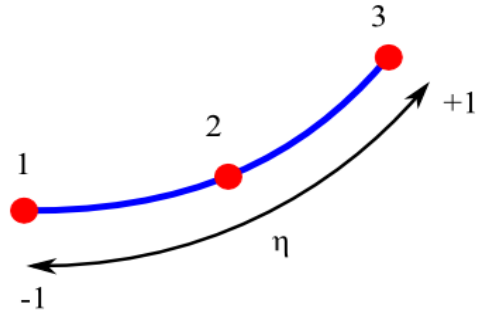


Figure 3.2 Local coordinate system for interpolation over the element

For a quadratic line element (figure 3.2), a set of Lagrangian interpolation functions in the local coordinate  $\eta$  are as follows:

$$N_1(\eta) = \frac{\eta}{2}(\eta - 1)$$

$$N_2(\eta) = (1 - \eta)(1 + \eta) \quad (3.13)$$

$$N_3(\eta) = \frac{\eta}{2}(\eta + 1)$$

For displacement,  $u$  at any point in the element can be found:

$$u(\eta) = \sum_{i=1}^3 N_i u_i \quad (3.14)$$

Expressing the above equation as a vector multiplication,

$$u(\eta) = N^T u \quad (3.15)$$

where  $N$  is a vector containing the shape functions and  $u$  is a vector containing the values of the displacement at three nodes.

For traction  $t$ :

$$t(\eta) = N_1 t_1 + N_2 t_2 + N_3 t_3 \quad (3.16)$$

$$t(\eta) = N^T t \quad (3.17)$$

### 3.1.4 Matrix method

We now proceed by writing the displacement and traction terms inside the integrals in (3.8) in their interpolated form using shape functions. The nodal displacements and tractions, being constants, may be removed from the integrals. For any position ' $p$ ', and for every element on the boundary, then, everything inside the integrals is known and can be evaluated at any point on the element. This is commonly performed using Gauss-Legendre quadrature, which approximates an integral as the weighted sum of values of the integrand sampled at specific integration points on the element.

Having converted the BIE into its discrete form, we can place the point  $p$  at node 1, and apply the Dirac delta function in the  $x$  – direction. Evaluation of (3.8) yields

$$c_1 u_1 + h_{11} u_1 + h_{12} u_2 + h_{13} u_3 + \dots = g_{11} t_1 + g_{12} t_2 + g_{13} t_3 + \dots \quad (3.18)$$

Integrating with the point  $p$  at 1, 2, 3 ...n:

$$\begin{aligned}
c_1 u_1 + h_{11} u_1 + h_{12} u_2 + h_{13} u_3 + \dots &= g_{11} t_1 + g_{12} t_2 + g_{13} t_3 + \dots \\
c_2 u_2 + h_{21} u_1 + h_{22} u_2 + h_{23} u_3 + \dots &= g_{21} t_1 + g_{22} t_2 + g_{23} t_3 + \dots \\
c_3 u_3 + h_{31} u_1 + h_{32} u_2 + h_{33} u_3 + \dots &= g_{31} t_1 + g_{32} t_2 + g_{33} t_3 + \dots \\
&\vdots \\
&\vdots \\
&\vdots \\
c_n u_n + h_{n1} u_1 + h_{n2} u_2 + h_{n3} u_3 + \dots &= g_{n1} t_1 + g_{n2} t_2 + g_{n3} t_3 + \dots
\end{aligned} \tag{3.19}$$

Now write the simultaneous equations in matrix form:

$$Hu = Gt \tag{3.20}$$

(3.20) is a statement of a set of  $n$  simultaneous equations with  $2n$  unknowns, where  $n$  is the total number of degrees of freedom. It is obvious that the equation cannot be solved without reducing the number of unknowns. This can most simply be achieved by applying the boundary conditions in such a way that at each node in each direction we prescribe either the displacement or the traction. Swapping all the unknowns variables to the left hand side of the equations:

$$Ax = By \tag{3.21}$$

Since the whole of the right hand side is now known, the matrix can be multiplied out and the following equation is generated:

$$Ax = b \tag{3.22}$$

This equation can be solved using a standard equation solver, such as Gauss Elimination.

## 3.2 NURBS Surface

Nonuniform Rational B-splines (NURBS) are mathematical models usually used in computer graphics, especially in product design and CAD (Computer-aided Design) models. NURBS can describe the surface of a model in a compact form. These surfaces are basically functions of two independent parameters  $u$  and  $v$  (figure 3.3) for a surface in 3D. For these surfaces there are control points which affect the resulting NURBS surface. In addition to this each control point has a weight to define how much it affects the NURBS surface.

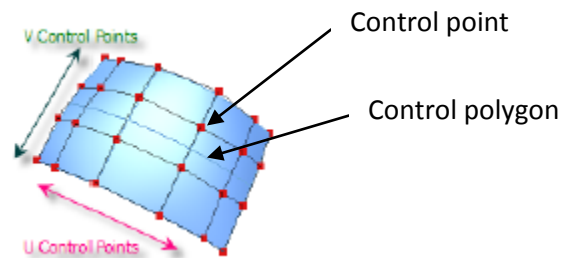


Figure 3.3 Control point and control polygon of a NURBS surface

In NURBS surface generation knots and spline order for both  $u$  and  $v$  must be defined. The knot vectors determine where and how the control points affect the NURBS surface [45]. The number of the knots is equal to the number of the control points plus order plus two. The knot vector divides the NURBS surface construction into many intervals. These intervals are referred as knot spans. Every time the value in the knot vector enters a new knot span, the new control points become active and the old ones are discarded. This means that each control point exist an influence only locally on the spline geometry. The values in a knot vector need to be in non-decreasing order because otherwise the algorithm selects a wrong knot.

The order parameter defines the degree of the polynomial used to represent the surface. The order is one less than the degree of the polynomial. Hence, second-order curves are linear, third-order quadratic, fourth-order cubic and so on. The number of control points must be greater than or equal to the order of the curve.

The mathematical definition of NURBS surface is given in (3.23),

$$S(u, v) = \frac{\sum_{i=0}^n \sum_{j=0}^m N_{i,p}(u) N_{j,q}(v) w_{i,j} P_{i,j}}{\sum_{i=0}^n \sum_{j=0}^m N_{i,p}(u) N_{j,q}(v) w_{i,j}} \quad 0 \leq u, v \leq 1 \quad (3.23)$$

where  $q$  and  $p$  are the degrees of basic function in  $u$  and  $v$  direction.  $P_{i,j}$  are the control points form a bidirectional control grid.  $w_{i,j}$  are the weights and  $N_{i,p}$  are the nonrational B-spline basis functions defined on the knot vectors  $u$  and  $v$ .

The surface approximation method uses the least-squares minimization to fit the control point. The least-squares procedure minimizes the error between the resulting surface and the original data points.

If we know the data points on the surface, we can define control points by using the least-squares surface approximation method. NURBS surfaces can only be approximated when the data point values are in regular grid order. This means that the points can be anywhere as long as they are topologically in order. The detail of the least-squares surface approximation method of NURBS can be found in the book by Piegl *et al* [45].

### 3.3 Statistics Theory for Measurement

#### 3.3.1 Normal Distribution

In probability theory, the normal (or Gaussian) distribution is a continuous probability distribution that is often used as a first approximation to describe real-valued random variables that tend to cluster around a single mean value. The graph of the associated probability density ' $f(x)$ ' function is "bell"-shaped, and is known as the Gaussian function or *bell curve*:

$$f(x) = \frac{1}{\sqrt{2\pi\sigma^2}} e^{-\frac{(x-\mu)^2}{2\sigma^2}} \quad (3.24)$$

where the parameter  $\mu$  is the mean (location of the peak) and  $\sigma^2$  is the variance. The distribution with  $\mu = 0$  and  $\sigma^2 = 1$  is called the standard normal. Note that a normally-distributed variable has a symmetric distribution about its mean.

### 3.3.2 Root Mean Square

The root mean square (RMS) statistic is most often associated with continuous variables, such as time. There are occasions where RMS is associated with discrete variables as well, such as specific measurements of a variable, for example weight. It is especially useful when variates are positive and negative, such as sinusoids. The unit of the calculation is the same as that of the data.

RMS is given by the following equation:

$$RMS = \sqrt{\frac{\sum_{i=1}^n Y^2}{n}} \quad (3.25)$$

### 3.3.3 Standard Deviation and Variance

Standard deviation is a widely used measurement of variability or diversity used in statistics and probability theory. It shows how much variation or 'dispersion' there is from the 'average' (mean). Standard deviation is also used to measure confidence level of the statistics. A low standard deviation indicates that the data points tend to be very close to the mean, whereas high standard deviation indicates that the data are spread out over a large range of values.

Standard deviation is given by the following equation:

$$\sigma = \sqrt{\frac{\sum_{i=1}^n (X_i - u)^2}{n}} \quad (3.26)$$

where  $u$  is the mean.

The variance is another measure of how far the value lies from the mean, and is in fact the square of the standard deviation. However, unlike the standard deviation, variances may be combined by addition. The population variance  $V$  is given by:

$$V = \sigma^2 = \frac{\sum_{i=1}^n (X_i - u)^2}{n} \quad (3.27)$$

## **Chapter 4**

### **Experimental Technique**

Experiment methods used to obtain the three-dimensional (3D) point clouds of different objects are described in this chapter. Two regular shaped components have been chosen in this research, a rectangular metal plate and a bar with a circular cross section. Furthermore, as examples of freeform shaped components measurement, a gas turbine blade and a steam turbine blade are also selected. These components were measured using a non-contact laser scanner. Different grid point clouds have been obtained using a different scanning resolution. The measurement procedure is given and the results are shown at the end of this chapter. The point clouds describing the surface geometry of a gas turbine blade are imported into a NURBS surface fitting application, and the geometry discretised into elements for use in BEM stress analysis in this research.

#### **4.1 Leica Laser Scanner**

The measurement process was carried out using the Leica LR-200 laser scanner. The LR-200 laser scanner is a large volume, non-contact, precision coordinate measurement machine. The LR-200 uses frequency modulated coherent laser radar (CLR) technology to measure the distance precisely from the mirror of the instrument to the surface point on which the laser is focused. The laser scanner beam is directed using a mirror mounted on

two axes, which moves the beam in the horizontal and vertical directions. The beam is focused to the smallest possible spot by a high-speed optical device.

This measurement device can be used in engineering measurement, inspection and reverse engineering, especially in large scale applications. The measurement range of this system is 1-25 metres. The maximum scan speed is 1000 pts/s in Pseudo Vision Mode. The scan errors based on absolute range are:  $\pm 0.025\text{mm}$  between 0.3 to 10m, and  $\pm 2.5\text{ppm}$  when the range exceeds 10m (key specification shown in table 4.1).

<b>FIELD OF VIEW:</b>		
Azimuth	$\pm 200^\circ$	
Elevation	$\pm 45^\circ$	
Range	1 to 25 meters	
<b>SYSTEM ACCURACY:</b>		
Scanner Angle Uncertainty	$\pm 1$ arc sec ( $\pm 0.28$ mdeg)	
2 to 10 m range	$\pm 100 \mu\text{m}$ ( $\pm 0.004''$ )	
>10 m range	$\pm 10$ ppm	
<b>MEASUREMENT SPEED AND PERFORMANCE</b>		
Laser Scanner Ranging Frequency	1,000 Hz	
Beam angular speed	90 deg/s, 20 m/s at 10m	
Surface Scans:		
“Pseudo Vision” mode	Rate (pts/s):	Accuracy (typical):
Maximum	1,000	$\pm 300\mu\text{m}$ ( $\pm 0.0122''$ )
Fast Medium	500	$\pm 150\mu\text{m}$ ( $\pm 0.006''$ )
“Metrology” mode	125	$\pm 100\mu\text{m}$ ( $\pm 0.004''$ )
Metrology	20	$\pm 80\mu\text{m}$ ( $\pm 0.003''$ )
Enhanced Metrology	2	$\pm 50\mu\text{m}$ ( $\pm 0.002''$ )

Table 4.1 System specification

The system integration is shown in Figure 4.1. The system contains four main components, the CLR scanner, instrument stand, power supply unit and mobile workstation. The CLR

Scanner is the essential component of the laser scanner system. It houses the laser scanner and beam-pointing electronics, motors, and other optical components.

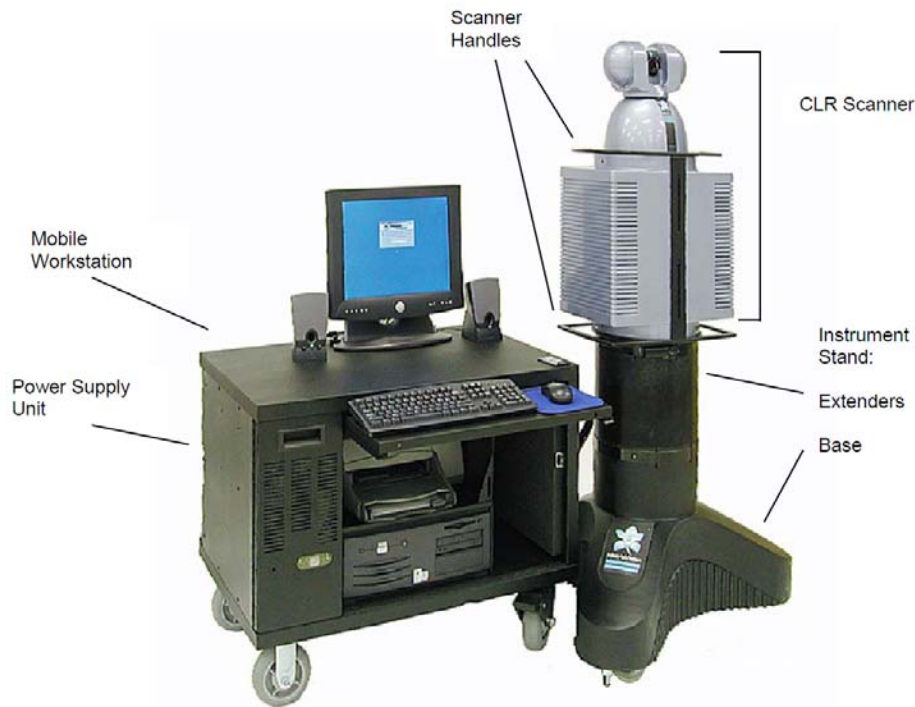


Figure 4.1 Laser scanner system integration

The basic principle of operation of the CLR device is illustrated in Figure 4.2. The laser uses frequency modulation to measure range since frequency measurement is more accurate than time. The frequency is modulated into a saw tooth wave, the wave cycle is two milliseconds with a base frequency of 200THz and the modulation adds up to 86THz at the peak. A laser beam, the frequency  $\Delta f$  which is linearly modulated in time  $\Delta t$ , is focused towards the target and the reflected signals are received using the same optical system. The travel distance of the beam  $D_2$  is equal to twice of the distance from the device to the target. The range  $\Delta D$  is determined by comparing the received signal  $\Delta f$  with the local signal (the local signal transmits in an optical fiber equivalent to 17.4m air), since the frequency shift is directly proportional to the round trip transit time  $\Delta t$  of the beam.

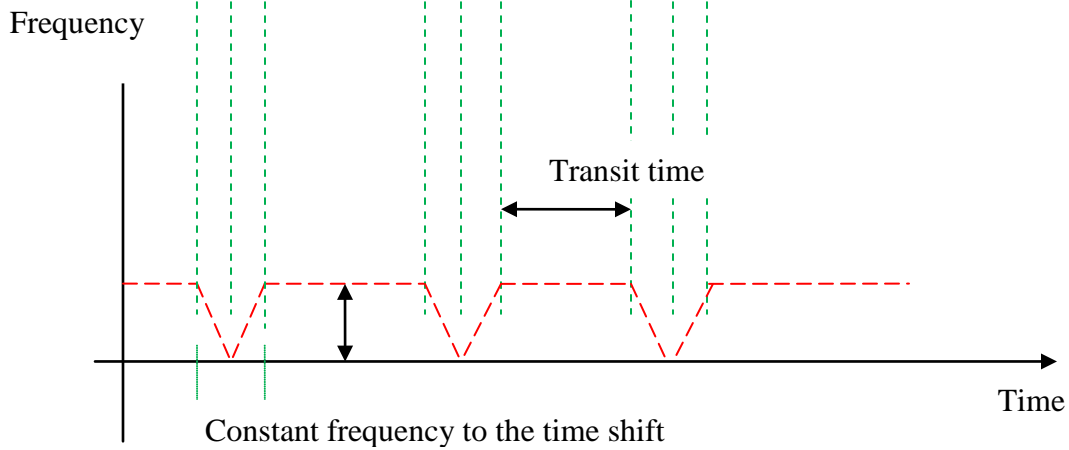
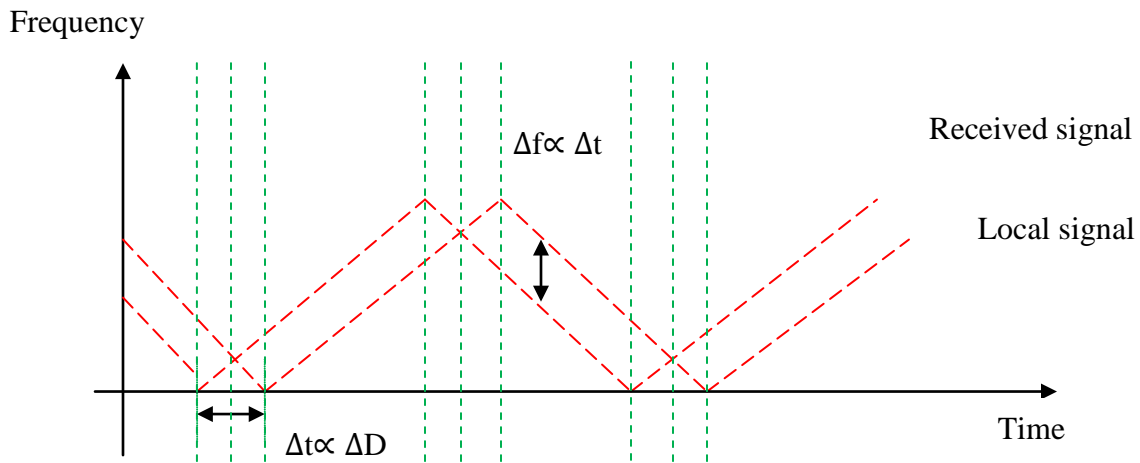
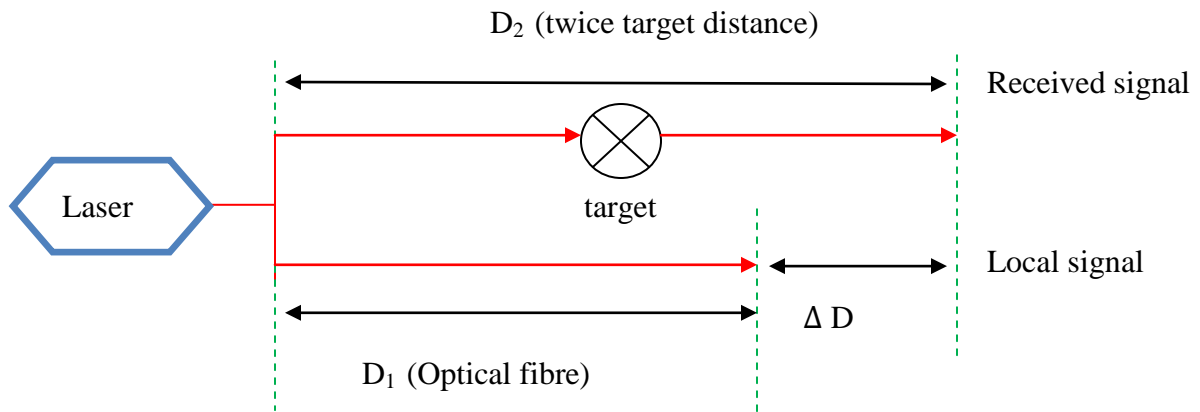


Figure 4.2 A combination of local and reflected energy, measure  $\Delta f$  instead of  $\Delta t$

The laser scanner system transmits an infra-red (IR) (class I) energy signal to measure the range, only  $10^{-8}\%$  of the original energy needs to be transmitted back in order to take the measurement. Also, a focused red laser (class II) is co-aligned with the infra-red laser. The focused red laser allows the user to identify and point to the measurement position, which can be seen on the target and the software interface window (figure 4.3).



Figure 4.3 Visible red laser pointing to the surface of a tooling ball

In the laser scanner measurement system, the points' position information is measured by a spherical technique (Figure4.4). The coordinates are initially recorded as the orientation of the scanner in azimuth and elevation, measuring the distance from the mirror of the instrument to the surface point on which the laser is focused. This can be converted to Cartesian coordinate system.

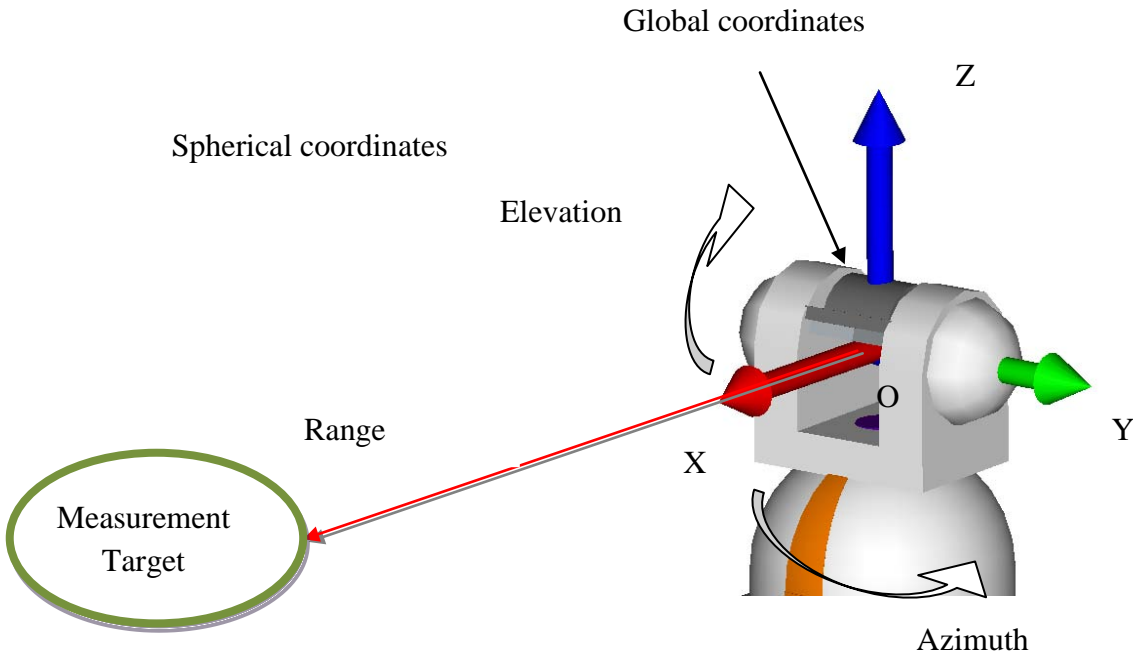


Figure 4.4 Measurement coordinates of laser scanner system

## 4.2 Spatial Analyzer

A piece of engineering measurement software known as Spatial Analyzer (SA) was used in this research. This software allows the user to control the operation of the laser scanner, carrying out the measurement tasks. It also allows the user to acquire and access the measurement data, and check the data's quality, performing point cloud processing and geometric analysis. This point cloud file can be converted to IGES file format and then imported into RE and CAD software for further application.

The software interface is shown in figure 4.5. The entire interface includes three parts; main window, measurement setting window and video window. The main window shows the position relationship between the laser scanner and the measurement target; the measurement target tree which allows users to see the different tasks; the functional tool bar allows users to perform parameter creation, geometry fitting and analysis etc. Scanning quality setting, grid setting, and target type selection can be adjusted in

measurement setting window. Users can see the target object and where the laser beam is pointing to via the video window.

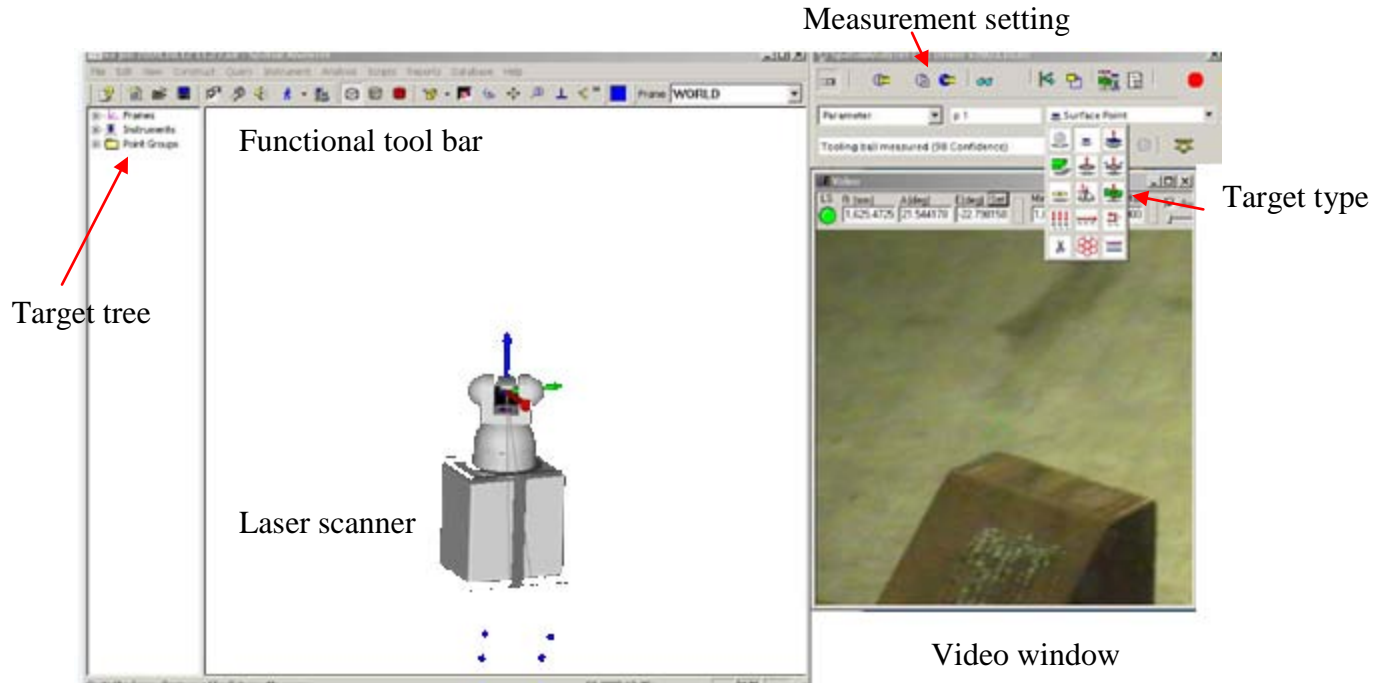


Figure 4.5 Software interface

### 4.3 System Calibration

In order to make sure the laser scanner is in good condition to carry out accurate measurement, the system needs to be well calibrated before any measurement activities. A few functions need to be checked:

- Linearization test: To linearize the laser scanner system before each measurement and after re-applying power to the system.
- Self test: This indicates whether the system is operating properly. It verifies there is sufficient light energy reaching the scanner head.

- Flip test: The Flip Test provides quick feedback on system calibration parameters through range and angle readings. The test takes range, azimuth and elevation readings with the mirror in normal initial (front sight) position, and then with the mirror position moved 180 degrees and flipped over (back sight).

If the system does not pass the above test or the system is transported, a quick or full compensation [40] also needs to be performed. The system also needs 4 hours warm up time from cold.

## **4.4 Scanning Method**

The laser scanner is a focused system with depth of focus (DOF) requirements, just like a camera. The laser scanner uses an (invisible class I) infra-red (IR) energy signal to measure the range. Laser scanner focuses the IR energy at the commanded focal point range. The amount of IR energy reflected back to the Laser scanner is dependent on the focus of the IR energy at the target range. Therefore, by taking a measurement of a point, the Laser scanner system needs to be focused on the target surface to ensure an accurate measurement.

However, it is impossible to measure each point manually, as a large number of points are always needed in RE application. Three main measurement methods used in laser scanner system are introduced here.

In addition, when scanning an object and taking a large amount of points, it is necessary to give the measurement resolution depend on needs. In the Laser scanner system, the resolution can be changed on both point spacing and line spacing.

### **4.4.1 Metrology Scan**

The metrology scan measures surface points on an object. However, the metrology scan has to be carried out inside a known perimeter (Figure 4.6). This method measures the

target surface line by line. The user can define the line spacing and point spacing. The scanner stops and refocuses before measuring each surface point. By doing this, the accuracy of the scanning data can significantly increase. Metrology scans are relatively slow, but this can produce more accurate point data and also bring the benefits for reducing the noise data. This method is typically used for inspection. Maximum data rates are approximately five to ten points per second.

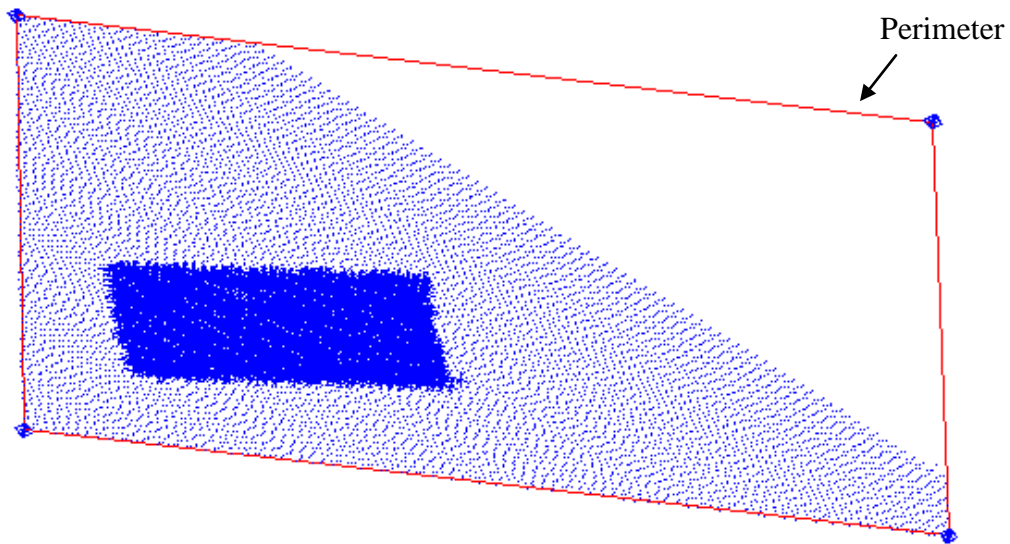


Figure 4.6 Metrology scan within perimeter

#### 4.4.2 Pseudo Vision Scan

The pseudo vision scan also measures surface points on an object. However, unlike the metrology scan needs to measure inside a known perimeter, the pseudo vision scan can focus the laser beam at the centre of the interesting area of target surface. The measurement will be performed within this area by giving the width and height. In comparison with metrology scans, pseudo vision scans are much more rapid as this method does not refocus on each point. Pseudo vision scans collect data rates of up to 1,000 points per second. Pseudo vision scans are more likely to be used for reverse engineering and deformation checks, rather than inspections.

### **4.4.3 Automatic Scan**

There are two function of this scanning method. The first one allows the user to carry out a fast, automatic measurement of the same positions of one or more objects. This is suitable for large and repetitive inspection tasks.

The other function is that of combining the metrology scan and pseudo vision scan together to perform a fast and accurate automatic scan. Unlike both methods, usually, the automatic scanning technique requires a metrology scan of the target first with coarse grid. This creates basic points which describe the feature of the target. Then a quick, automatic and sparse pseudo vision scan can be performed around this point, the grid can then be set manually to cover the space.

## **4.5 Measurement Strategy**

In RE, the quality of the data acquisition process is crucial to the accuracy of the resulting mesh and CAD models. Therefore, before carrying out a measurement, it is important to define a suitable measurement plan as this can bring benefits to an accurate measurement and save process time.

When a part is located on the table, always the first thing that needs to be considered is how to scan it. An object cannot be scanned in just one setup to obtain the full surface information, since it has a complex geometry with hidden surfaces when viewing in one direction. Thus, it is very important to decide suitable scan times from different angles to capture the full surface information, since more scans can take much more time. A turbine blade uses here as a measurement example.

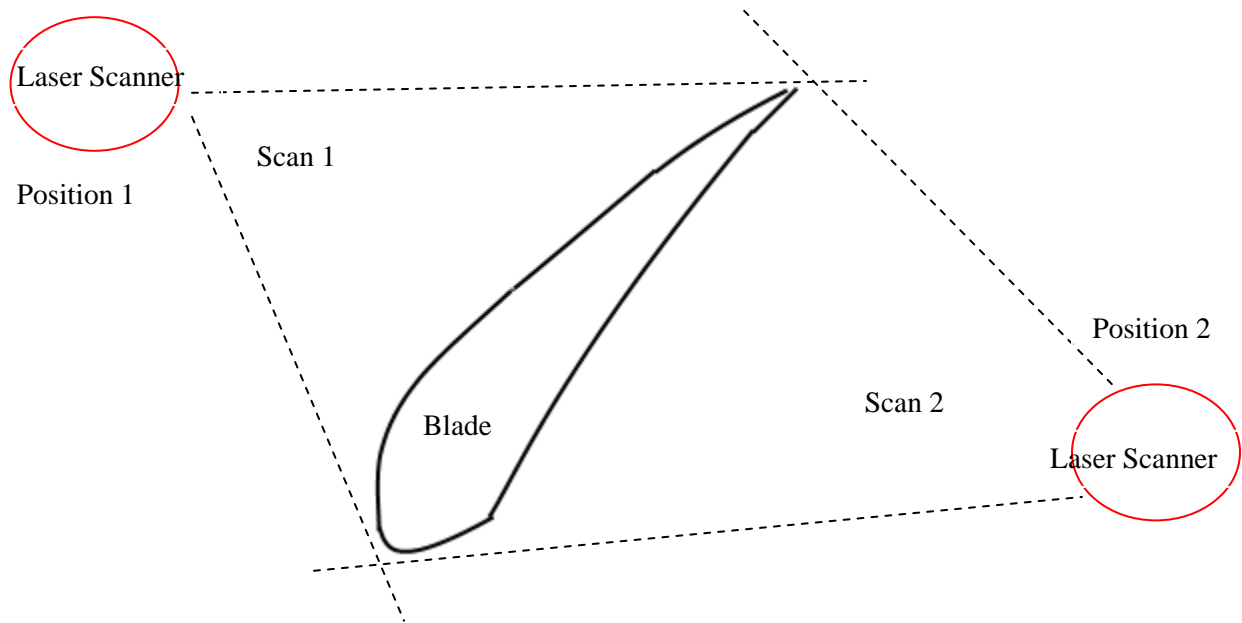


Figure 4.7 Angle of Azimuth direction and scanning times

From Figure 4.7, it seems that the blade surface information can be fully captured by just scanning twice from two directions. However, when performing a real scan, the angle between the laser beam and the target surface has a significant effect on the measurement quality. When the laser is pointing normally at the surface, the highest energy reflection obtained. When the angle is getting smaller, the reflected energy decreases. And the more reflected energy is obtained, the better measurement quality can be achieved. Also, a small angle between the laser beam and the surface can cause an increase of noise data in the measurement results. In the above scanning plan, the angle between the laser and the leading edge of the blade is relatively small. This can cause a poor measurement result. During the measurement, we also found that, if the target has a glossy surface, the angle cannot be smaller than 30 degrees, as the small angle leads to very low reflected energy from this kind of surface, which leads to a poor measurement result. Considering the energy reflection issue, a new scanning plan for the blade is shown in Figure 4.8. The new plan avoids the poor results occurring in the leading edge.

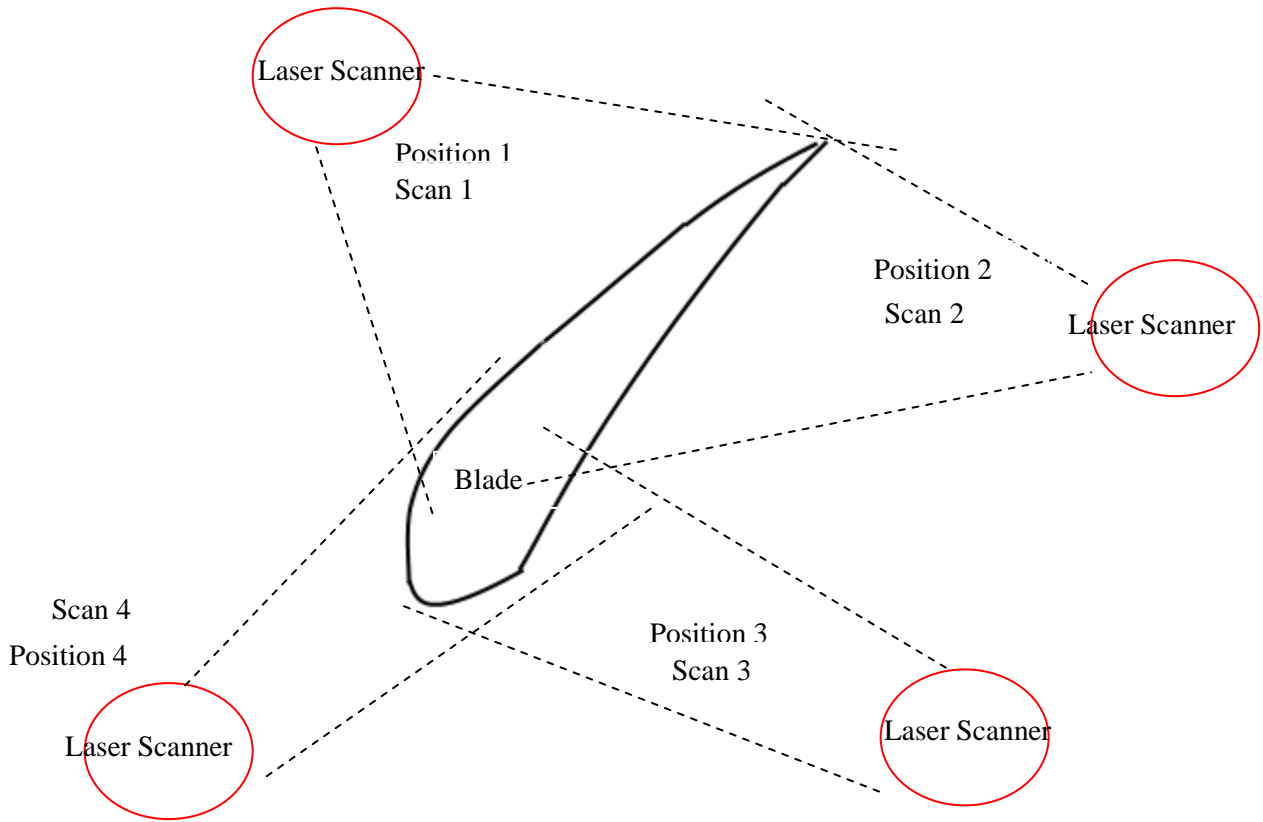


Figure 4.8 Modified scanning plan after considering the angle issue

The azimuth direction has been considered above. However, the elevation direction also needs to be considered, which is directly controlled by how high the object is placed, since the height of the laser scanner is fixed. It suggests that the object is placed at least above half height of the laser scanner (as shown in figure 4.9), to make sure the angle is larger than 30 degrees. Also, the measurement range of the system is 1m to 25m, so the object needs to be placed at least 1m further away from the laser scanner, since if the range is within 1m, the system cannot focus.

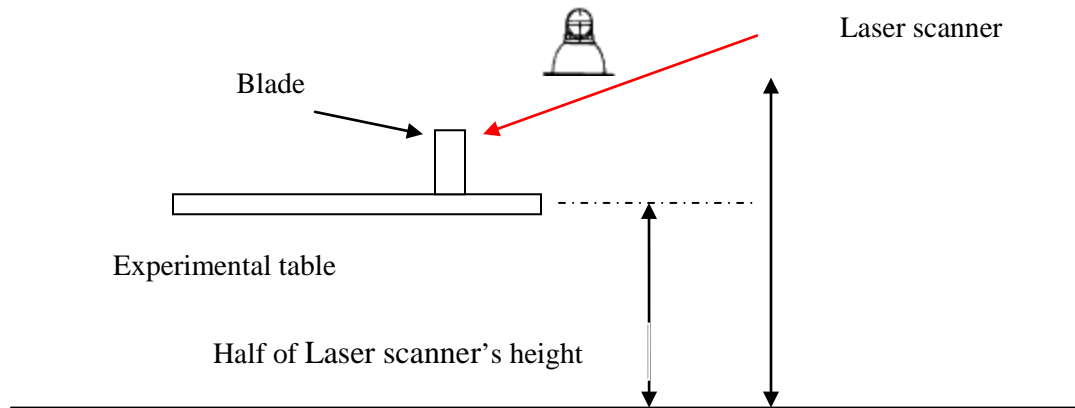


Figure 4.9 Angle of Elevation direction

Also, it is important to fix the object in a suitable way for scanning. Some objects contain complex features, so if just laying this kind of component on the table, a lot of features will be hidden and cannot be scanned, such as a turbine blade. To avoid this problem, a vice is used to fix the blade (Figure 4.10).



Figure 4.10 Fix a gas turbine using vice

Furthermore, as a smooth metal ball was used (known as tooling ball) as the reference for aligning different view point clouds of an object. It needs to be careful when fixing these balls, since when the scanner scans the object from a different direction, some of the balls may be hidden. Thus, using a sufficient number of balls or choosing a suitable location is necessary.

The last issue is choosing different scan methods for different features. For instance, the leading edge, trailing edge and fillet are important features of the turbine blade. These features contain sharp edge and high curvature, and this needs to be detailed modelled in RE. Thus, choosing a dense grid and metrology scan when measuring these features is necessary. Also, for the area of less interest, a vision scan can be chosen to perform a fast scan. Figure 4.11 shows a fine scan around the leading edge, trailing edge and fillet of a steam turbine blade.

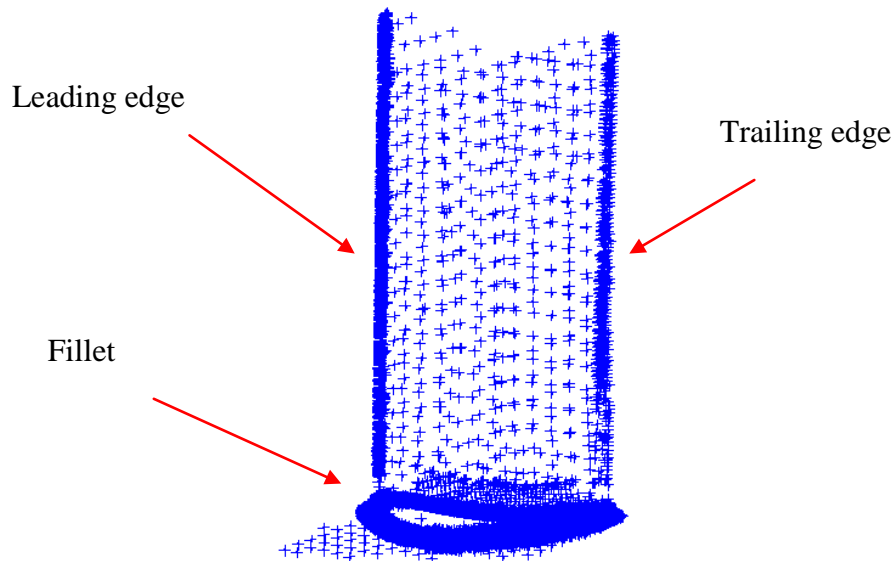


Figure 4.11 Fine scan of important features

## 4.6 Point Clouds Alignment

In order to digitize the entire surface of an object, the model needs to be rotated and scanned several times from different angles. Aligning these point clouds together to present the whole geometry of an object is essential.

The point clouds captured from different locations were aligned with the method of three-point alignment. A reference tooling ball was used here (Figure 4.12). The position of the centre of the tooling ball was determined, knowing the ball's radius. The object needs to

be surrounded by at least three tooling balls. These balls' coordinates reflect the information of relative position in different locations. The tooling balls were measured on the first position and these tooling balls were as a set reference group. Once the scan had been completed on the first position, the laser scanner was moved to the second position (or the object was rotated). The tooling balls need to be scanned again on each new position of the laser scanner. It is important to measure these tooling balls in the same order each time to allow the coordinate information to match.

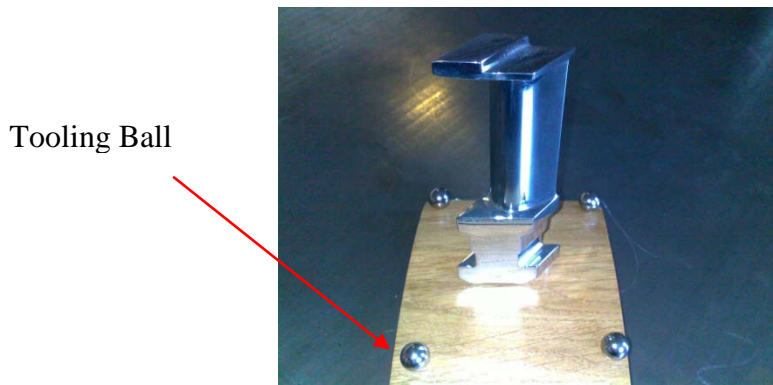


Figure 4.12 Using tooling balls as coordinate reference

The spatial transformations in SA are described below here. Consider a situation in which there are frames A and B, and we want to transform a geometric description from frame B to A. For position, we describe the  $X_A$ ,  $Y_A$ , and  $Z_A$  components of the origin of B. Note these terms are the distances along the  $x$ ,  $y$ , and  $z$ -axes of A. For rotation, we use unit rotation matrices, which are given below:

$$Rx(\theta_1) = \begin{cases} 1 & 0 & 0 \\ 0 & \cos \theta & -\sin \theta \\ 0 & \sin \theta & \cos \theta \end{cases} \quad (4.1)$$

$$Ry(\theta_2) = \begin{cases} \cos \theta & 0 & \sin \theta \\ 0 & 1 & 0 \\ -\sin \theta & 0 & \cos \theta \end{cases} \quad (4.2)$$

$$Rz(\theta_3) = \begin{cases} \cos \theta & -\sin \theta & 0 \\ \sin \theta & \cos \theta & 0 \\ 0 & 0 & 1 \end{cases} \quad (4.3)$$

$$R_{xyz}(\theta_1, \theta_2, \theta_3) = Rx(\theta_1)Ry(\theta_2)Rz(\theta_3) \quad (4.4)$$

where  $\theta_1, \theta_2, \theta_3$  is rotational angle of  $x, y,$  and  $z$ -axes of A. In double precision arithmetic this application of multiple coordinate transformations causes only a very small error to accumulate.

After finishing all the scans, the several views of the point cloud were aligned by translating these tooling balls to the reference group by the relative position. The combined point clouds of a turbine blade example are shown in Figure 4.13 ( five point clouds 1 – green, point cloud 2 – orange, point cloud 3 – red, point cloud 4 – blue, point cloud 5 – purple).

In order to understand the accuracy of point cloud alignment, the errors during each alignment are also recorded (shown in table 4.2)

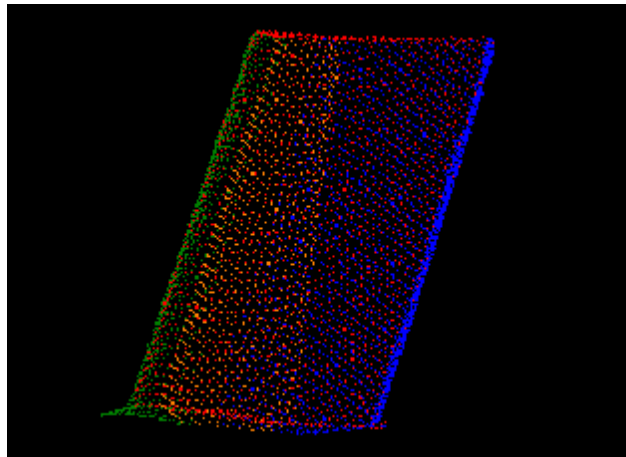


Figure 4.13 Point clouds alignment for a sample turbine blade (point cloud 1 – green, point cloud 2 – orange, point cloud 3 – red, point cloud 4 – blue, point cloud 5 – purple)

Best-fit transformation	Align 1	Align 2	Align 3	Align 4
Max error (mm)	0.0090	0.0043	0.0089	0.0119
RMS error (mm)	0.0066	0.0034	0.0064	0.0091
StdDev error (mm)	0.0080	0.0041	0.0079	0.0111

RMS error: Root mean square error; StdDev error: Standard deviation error.

Table 4.2 Errors during each alignment

From the above table, the errors during each alignment process are very small. This can be negligible for the accuracy of the scanning process.

## 4.7 Scan Results

The point clouds of a rectangular metal plate, a bar of circular section, a gas turbine blade and a steam turbine are shown here (as shown in figure 4.14 – 4.17). Three different grid point clouds are obtained for both plate and bar, which are  $2 \times 2$ mm grid,  $3 \times 3$ mm grid and  $4 \times 4$ mm grid. For the gas turbine blade, which is for freeform surface modelling, we collected denser point clouds (tip and base of blade are ignored), which are  $0.5 \times 0.5$ mm grid,  $1 \times 1$ mm grid and  $3 \times 3$ mm grid. For the steam turbine blade, we also collected three different grid point clouds:  $1 \times 1$ mm grid,  $2 \times 2$ mm grid and  $3 \times 3$ mm grid. In addition, as our objective of this research is to investigate the efficiency of using a graded boundary element mesh model in stress analysis, we also generated a graded grid point cloud of the steam turbine blade.

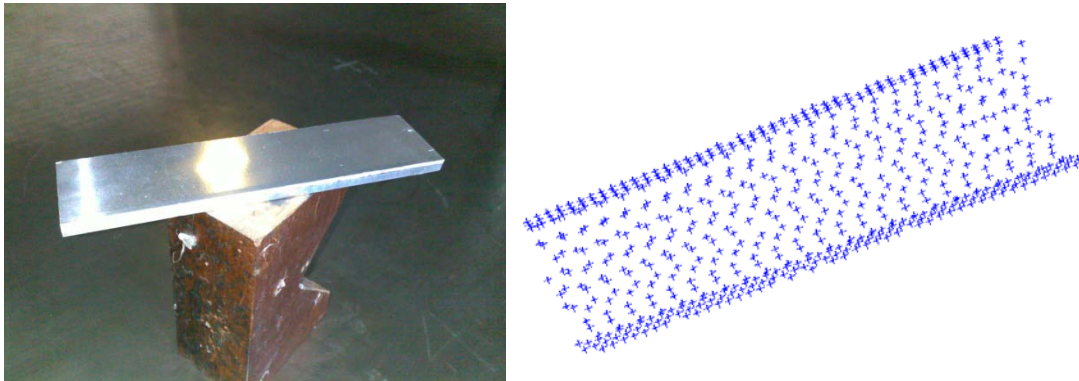


Figure 4.14 Point cloud of the rectangular metal plate ( $2 \times 2$ mm grid on top and bottom surface,  $1 \times 1$ mm grid on sides)

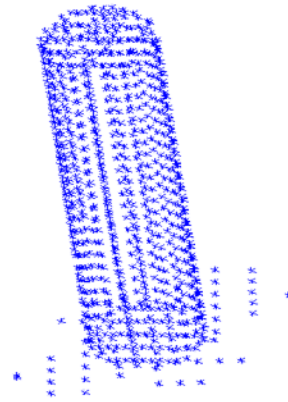


Figure 4.15 Point cloud of the bar of circular cross section ( $2 \times 2\text{mm}$  grid)

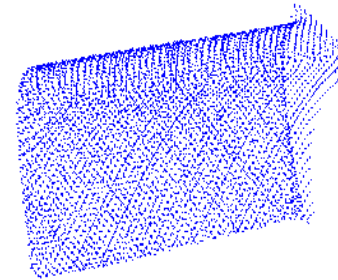


Figure 4.16 Point cloud of the gas turbine blade ( $1 \times 1\text{mm}$  grid)

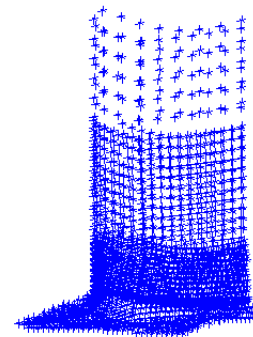


Figure 4.17 Point cloud of the steam turbine blade (Graded point cloud,  $1 \times 1\text{mm}$  on the fillet,  $2 \times 2\text{mm}$  around the middle of the blade,  $3 \times 3\text{mm}$  on tip)

At last, the point clouds are exported in Initial Graphic Exchange Specification (IGES) file format. This format can be imported into Rapidform for further processing.

## **Chapter 5**

### **Boundary Element Mesh Generation**

One of the major advantages of the Boundary Element Method compared to the Finite Element Method is that it uses a smaller number of nodes and elements for the same level of accuracy, also that no internal points and elements are needed for 3D analysis in BEM. As the CAD model is a boundary representation of the geometry, these CAD surface can be directly used into boundary element applications. The 3D meshes generated in this research are of the boundary element type; this means there are no internal points and elements. Therefore, according to the character of BEM, these meshes can be directly used into computational boundary element analysis.

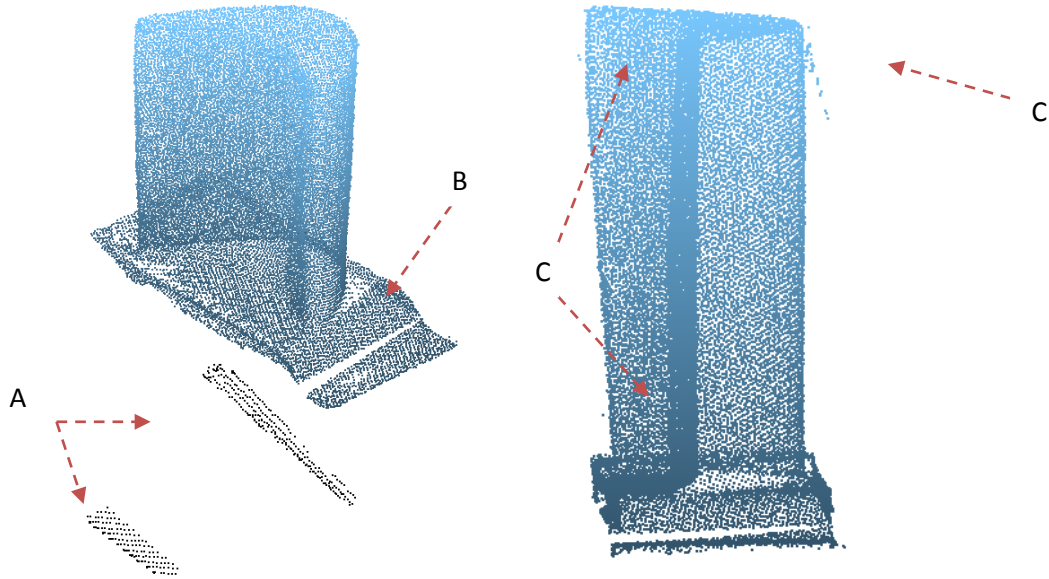
This chapter contains a description of mesh generation for a rectangular metal plate, a circular bar and a turbine blade using commercial reverse engineering software known asRapidform. For one metal plate and circular bar, inaccurate meshes occurred during the initial mesh generation and the solutions used to repair the meshes are given. For turbine blade, a  $3 \times 3$ mm grid point cloud, a  $2 \times 2$  mm grid point cloud and a  $1 \times 1$ mm grid point cloud were used respectively, and a graded mesh model combining the three different grid densities point clouds are also produced.

## 5.1 Point Cloud Pre-processing

Point cloud pre-processing is the key stage before generating a good quality mesh and surface model, as the initial scanned data usually contain spikes, outliers and poor quality regions. These noisy data directly affect the surface quality and they are also the major contributor to large errors. Thus the poor quality points need to be removed at the earliest opportunity. In addition, point clouds registration, smoothing and decimating are also needed depending on case. As the point clouds registration has already described in chapter 4, we focus now on the removal of parts that can be considered to be ‘noise’.

### 5.1.1 Noise Reduction

Figure 5.1 shows the initial point cloud ( $0.5 \times 0.5\text{mm}$  grid) obtained from the blade measurement. It can be seen that it is easy to detect and remove unwanted data if points are obviously a long way off the target surface. For a small region of noise points, careful manual removal is needed as these points may cause one rough mesh and surface. The major noise data encountered in current research are unwanted background information (Figure 5.1(A)), the base of turbine blade (Figure 5.1(B)) and noise points (Figure 5.1(C)) which are very closed to the surface.



A. Unwanted background information captured during scanning

B. The base of turbine blade

C. Noisy points close to the surface

Figure 5.1 Examples of noisy points

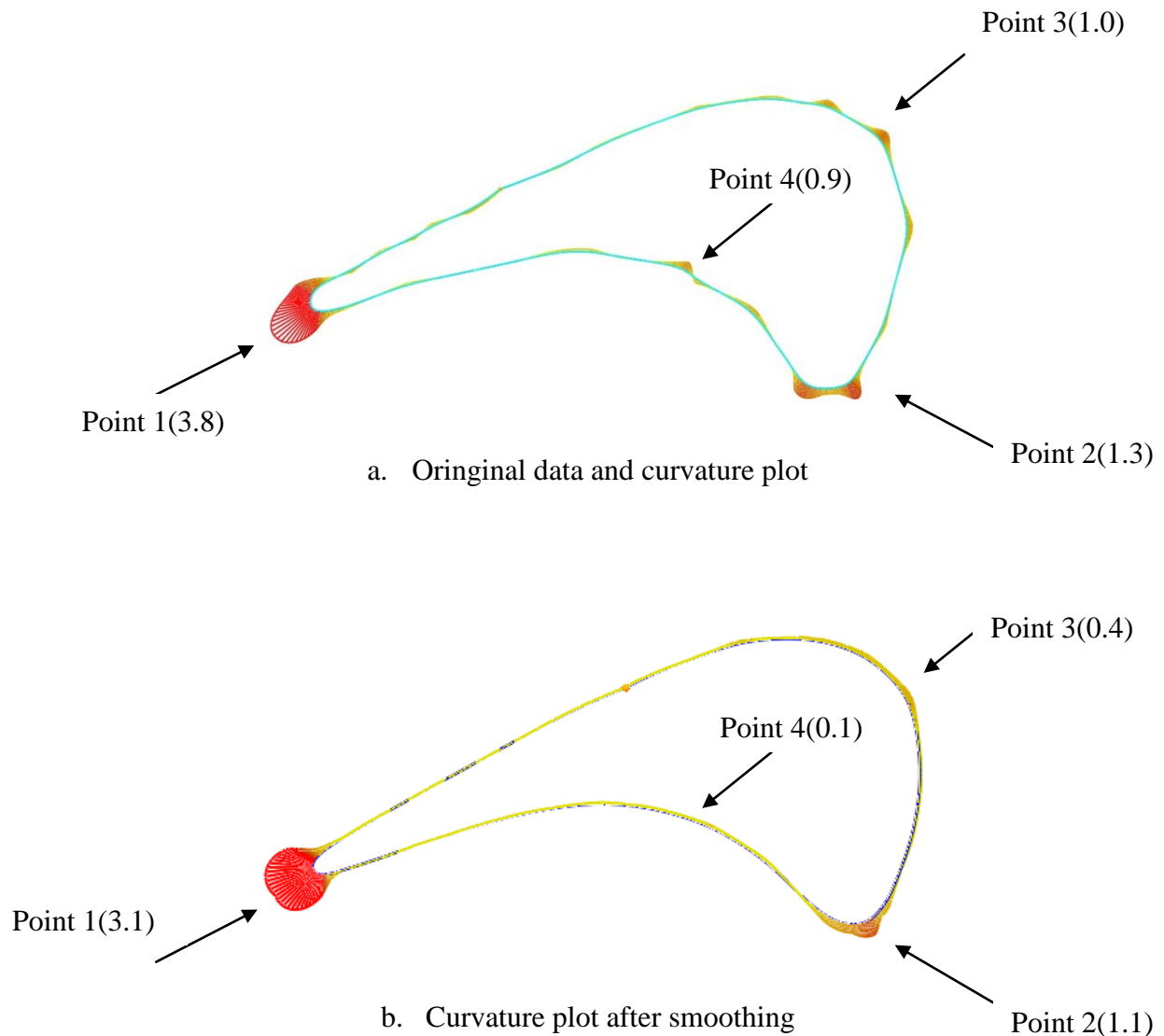
### 5.1.2 Smoothing

Usually the data obtained from measurement are subject to errors. In mesh generation and surface reconstruction, we not only want the data to provide a good approximation to the actual geometry, but we also want the curves to be visually pleasing in a functional or an aesthetic way. Therefore, in order to generate a smooth mesh and surface for a freeform object, smoothing is also a common step for point cloud pre-processing as the point clouds texture obtained directly from scanning are undesirable.

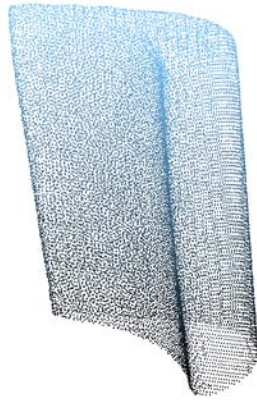
Smoothing reduces the point cloud or mesh roughness by moving a selected region. Nevertheless, the smoothing level needs to be chosen carefully as extreme smoothing has to potential to cause deformation. Figure 5.2 (a) illustrates an example of a curvature plot of a turbine blade section. The largest curvature 3.8 occurred around the trailing edge (point 1), which is not surprising as it is where the curve undergoes a tight turn. The second largest curvature 1.3 is found around the leading edge (point 2). Point 3 and 4 are

also shown unsmooth curve representation of the geometry of the aerofoil. Figure 5.3(b) shows the curvature plot of the aerofoil section after smoothing. It can be clearly seen that the curvature on point 3 and 4 are significantly reduced to 0.1 and 0.4 from 0.9 and 1.0 respectively. The curvature is also slightly reduced on point 1 and 2.

Figure 5.3 shows the blade point cloud after pre-processing. The major noise data were removed and an appropriate smoothing is performed.



## 5.2 Smoothing of blade airfoil section



5.3 Blade point cloud after pre-processing

## **5.2 Meshing Strategies for Surface Representation and Boundary Element Analysis**

In the meshing process, generally, an initial mesh is generated first for visual inspection of the structural integrity. The quality of the initial mesh is based on the point cloud (the mesh cannot create geometric features which are missing from the original point cloud). If any major features are hard to detect or even missing, this means the original point cloud does not provide sufficient information for good quality mesh generation, thus an enhanced scan needs to be taken.

When the initial mesh does present the major features of the object, additional meshing processes can be carried out to enhance the shape. These generally include four major steps: missing features repair, boundary edit, decimate and smoothing. In addition, an optimised model also can be achieved by using graded meshing on different features of the model depending on application.

In this section, two types of mesh are generated. The first type is for blade freeform surface reconstruction, and the second type of meshes is for efficient boundary element stress analysis.

### 5.2.1 Meshing for Freeform Surface Reconstruction

Meshing is an important step before surface fitting. The quality of the mesh directly affects the quality of the surfacing result. In general, a dense mesh produces better surface fitting, since the model contains more detailed geometric information. However, using an extremely dense mesh requires more computing time and storage. The gas turbine blade was selected as a case study for surface fitting application.

Three mesh models were generated in Rapidform based on a  $0.5 \times 0.5$ mm grid, a  $1 \times 1$ mm grid and a  $2 \times 2$ mm grid point cloud (as shown in figures 5.4 – 5.6). The initial meshes of each model are shown in (a), and the meshes after processing (such as smoothing) are shown in (b). The 0.5mm grid shows the finest geometry representation of the blade surface. For the 1mm grid mesh, the result still remains at an acceptable level. However, the 2mm grid mesh does not show a good representation of the surface, since the original point cloud of 2mm grid mesh does not supply enough information of some parts, and in particular points are missed around the edges.

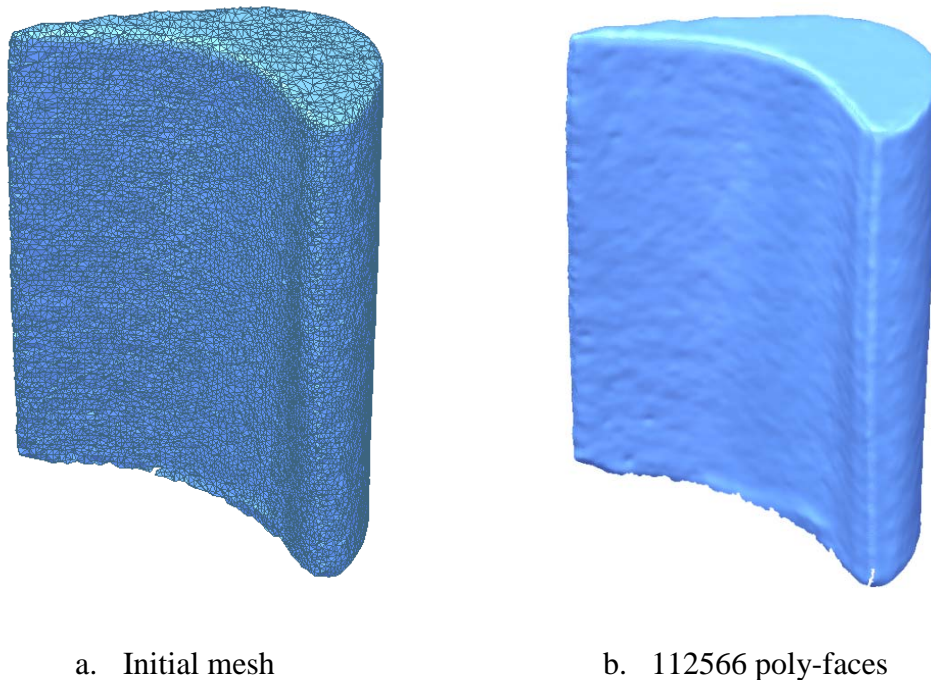
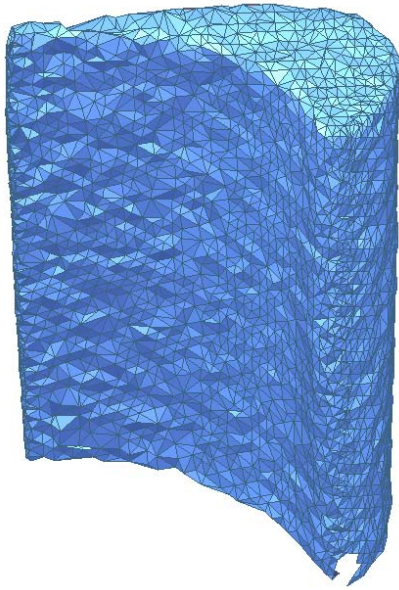


Figure 5.4 Meshing based on 0.5 by 0.5mm grid point cloud

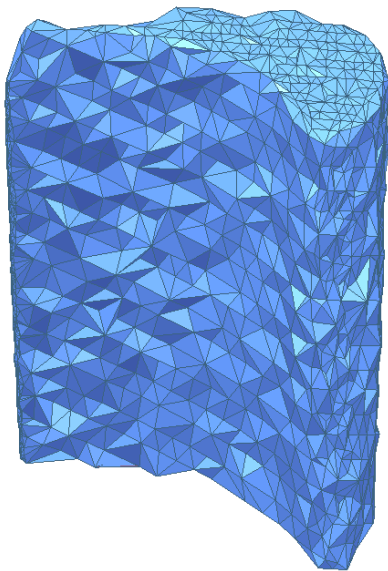


a. Initial mesh



b. 66060 poly-faces

Figure 5.5 Meshing based on 1 by 1mm grid point cloud



a. Initial mesh



b. Poor representation of edges

Figure 5.6 Meshing based on 2 by 2mm grid point cloud

In addition, an optimised mesh is also produced using an adaptive mesh method based on a  $0.5 \times 0.5$  mm grid mesh model. The elements (Figure 5.7(b)) around the edge remain sufficient density, but the elements reduce over the body for saving computing time.

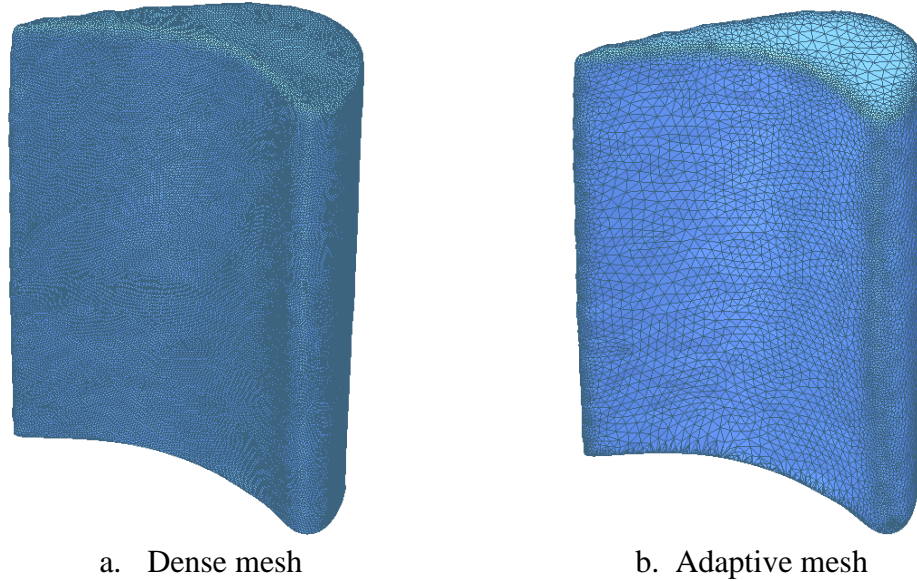


Figure 5.7 Mesh optimization based on 0.5mm grid mesh

### 5.2.2 Meshing for Boundary Element Stress Analysis

In FEM/BEM stress analysis, the accuracy of the simulation results is highly dependent on the quality of the mesh. Since the cost of performing such an analysis is directly related to the number of degrees of freedom, we can view the objective of the current work as the production of a mesh that will efficiently give results of suitable accuracy.

Although the surface fitting can be finished within ten minutes for a mesh containing more than a hundred thousand elements, the boundary element programme may need more than one day to finish a stress analysis of mesh model which contains ten thousand elements. Therefore, to generate a high quality mesh but containing fewer elements to produce a good simulation results is always a crucial task in computational analysis.

As the mesh describes the geometry of the analysis target, the generation of a geometrically accurate mesh based on the scanning data is major task in our research as the point clouds always contain different kinds of error. Also, the regularity of the

element is important in order to achieve an accurate stress distribution, especially the elements generated around fillets and sharp edges, where stress concentrations also arise. This is an important point since the areas that present most challenges to the accurate meshing are also those in which a quality mesh is most important.

Element distortion was also found during the meshing of turbine blade. These elements (always with very small, long and narrow geometry) always cause inaccurate simulation results.

In this section, the boundary element meshing algorithms are developed by considering three example objects: a rectangular metal plate, a bar of circular cross section and a steam turbine blade. Each presents its own difficulties and it is shown how these inform the fine algorithms.

### 5.2.2.1 Rectangular Metal Plate

The challenge of the mesh generation of metal plate is to accurately represent the sharp edges. As be seen in figure 5.8, the mesh cannot represent sharp edges as there are no points on the edges in the original point cloud.

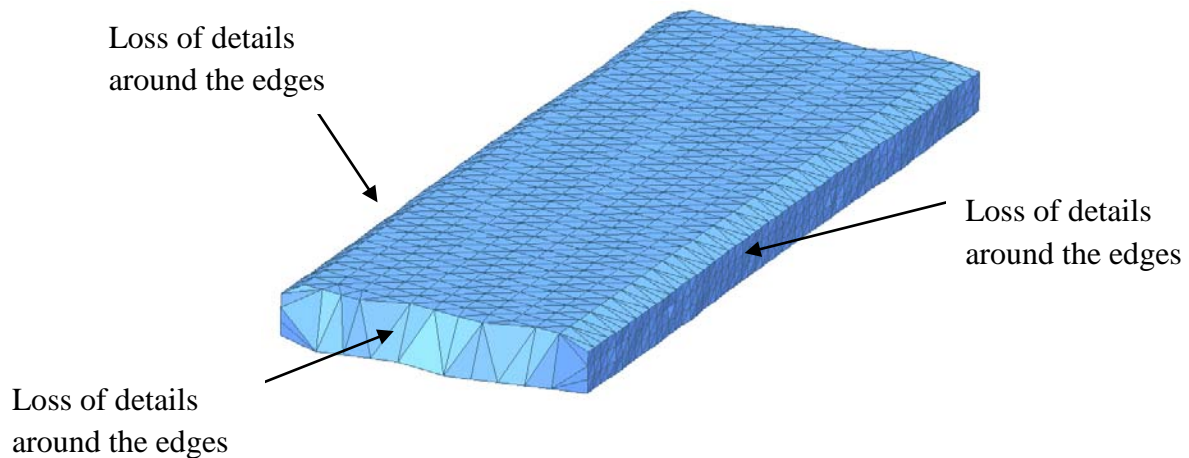


Figure 5.8 Sharp edges problem

It is well-known that during measurement, sharp edges are always features which are hard to detect and define. The main restriction comes from the measurement technique, and even using a very fine scan resolution, the points on the edges are still difficult to capture accurately.

A manual repair solution was performed in the current work in order to recreate the missing feature on the sharp edge. During the measurement, many points were obtained on each surface of the metal plate. These points can accurately describe the flatness of these surfaces.

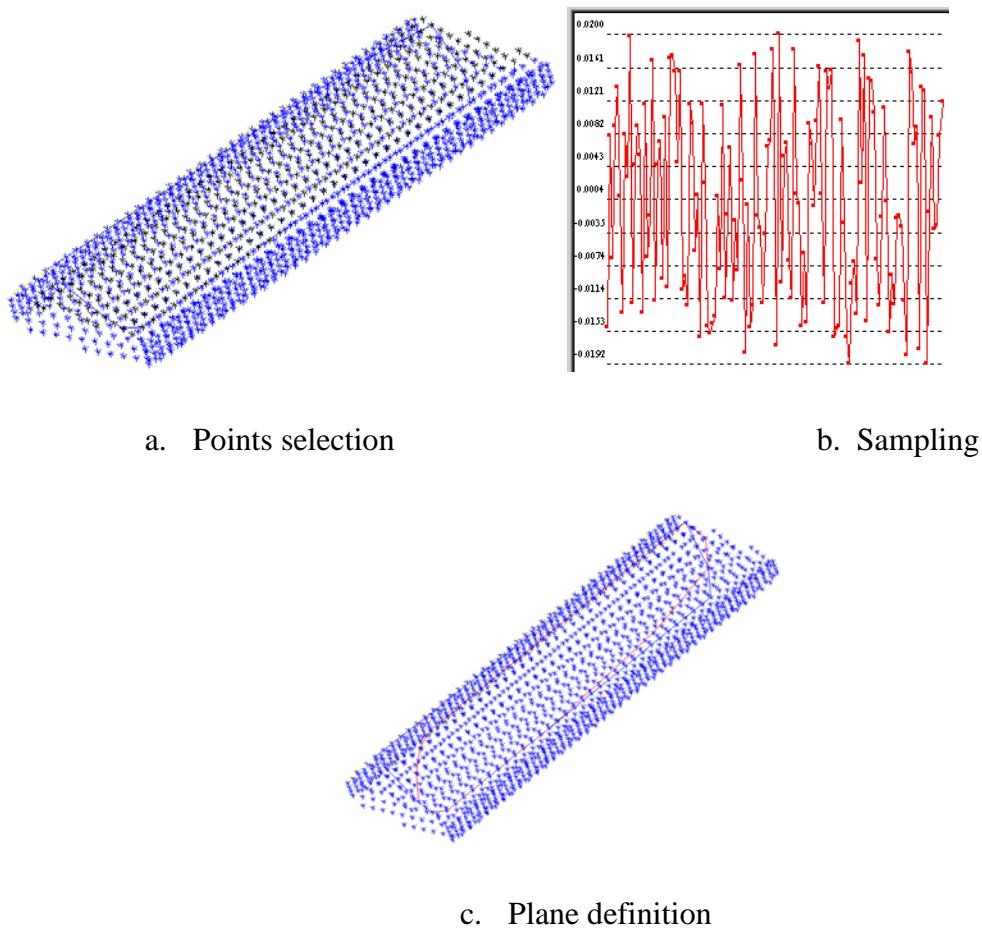


Figure 5.9 Plane define in spatial analyzer

The solution is to determine the planes for two adjacent surfaces of the plate based on these points. As can be seen in figure 5.9 (a), the points (black) which on the top plate surface are selected. These points were sampled (figure 5.9 (b)) to determine the fine

tolerance of the plane which represent the surface (0.02mm tolerance using here). Once the points which are outside the tolerance have been deleted, the plane (red geometry in figure 5.9 (c)) can be defined and recreated. The intersection between these two adjacent planes is obtained (the red line in figure 5.9) which represents the sharp edge, and then points (green points in figure 5.10) can be created on this line with the required geometry. Therefore, the features can be repaired and an accurate mesh containing edges can be achieved (figure 5.11).

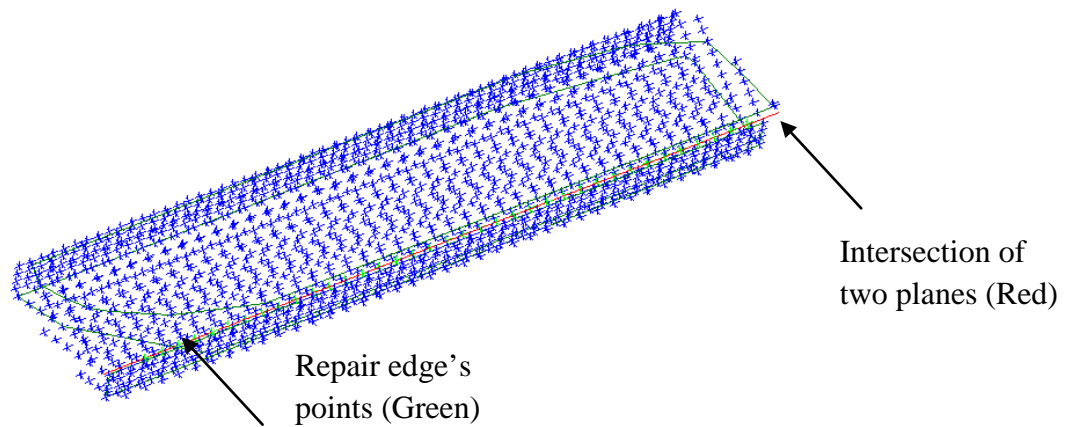


Figure 5.10 Repair points on the edges

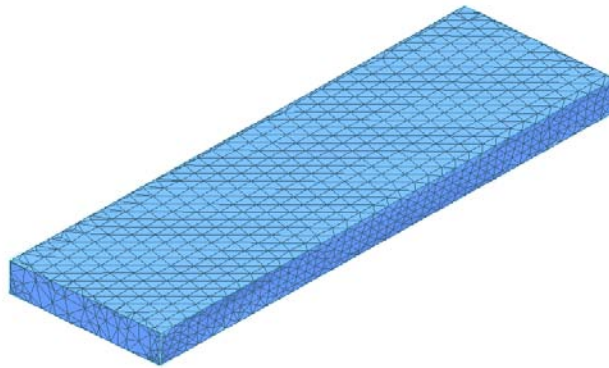
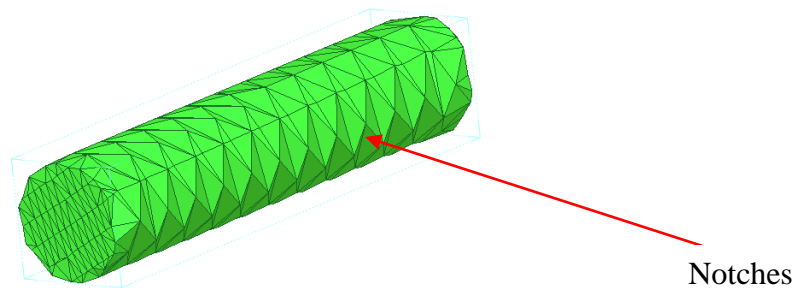


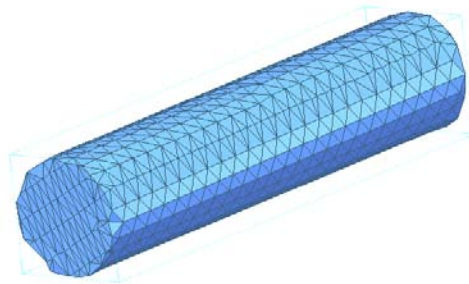
Figure 5.11 Metal plate mesh following edge repair

### 5.2.2.2 Bar of Circular Cross Section

The second problem of interest is the mesh generated for a regular curved surface. Thus we consider a straight bar of circular cross section. The same edge definition problem is also encountered on the intersection between the cylindrical surfaces and the two flat ends of the circular bar during the meshing process. The same solution as described in the metal plate meshing process was used to avoid this. However, some notches were found during the meshing process when a sparse grid point cloud was used (as shown in figure 5.12(a)).



a. Bad mesh representation of the surface (Sparse point cloud)



b. Good mesh representation of the cylindrical surface (Dense point cloud)

Figure 5.12 Meshes of Circular Bar

Unlike the fine mesh of the bar (figure 5.12(b)), the triangular elements of the sparse mesh are not connected as we expected. A manual repair process can be taken by removing the bad elements and reconnecting those nodes. But this option is time

consuming and is not suitable for a model which contains many bad features. To solve this problem, we develop an automatic repair code in Matlab (details to be given in chapter 7) to recreate the elements which represent more accurately the cylindrical surface of this circular bar.

When we generate the BEASY input file for stress analysis (a detailed description is given in Chapter 7), the mesh generated in Rapidform (comprised of 3-noded triangular elements) needs to be converted to 6-noded elements, by the addition of a mid-node on each edge of the triangular elements. Our approach is to snap these 6 nodes to the surface of the bar, which is known analytically, and then the mesh could be able to accurately represent the surface curve of the bar.

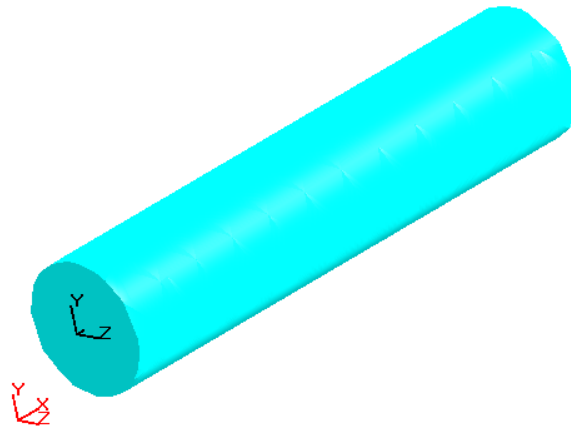


Figure 5.13 Repaired geometry of the circular bar

### 5.2.2.3 Steam Turbine Blade

The last problem of our interest is the mesh generation for a freeform shaped part with a  $90^\circ$  fillet. A steam turbine blade was used as this test case. The major challenges presented here are how to deal with meshing around the fillet and the trailing edge. As can be seen from the measurement procedure, the fillet is sharp and is difficult to capture. The angle of the trailing edge is even smaller than  $15^\circ$ , and as has been described, it is very difficult to capture and define points on such a sharp edge. Figure 5.14(a) shows an initial mesh of the blade based on a  $3 \times 3$ mm grid point cloud. This mesh has been

manually repaired by hole filling and smoothing as the initial mesh contains defects. As can be seen in the figure 5.14(b), the representation of the trailing edge remains poor after this process. In order to correct these errors, we snapped the nodes which close to the trailing edge to the correct X and Y coordinate where the trailing edge is located using an automatic Matlab programme (details to be given in chapter 7). A repaired blade mesh example is shown in figure 5.14 (c).

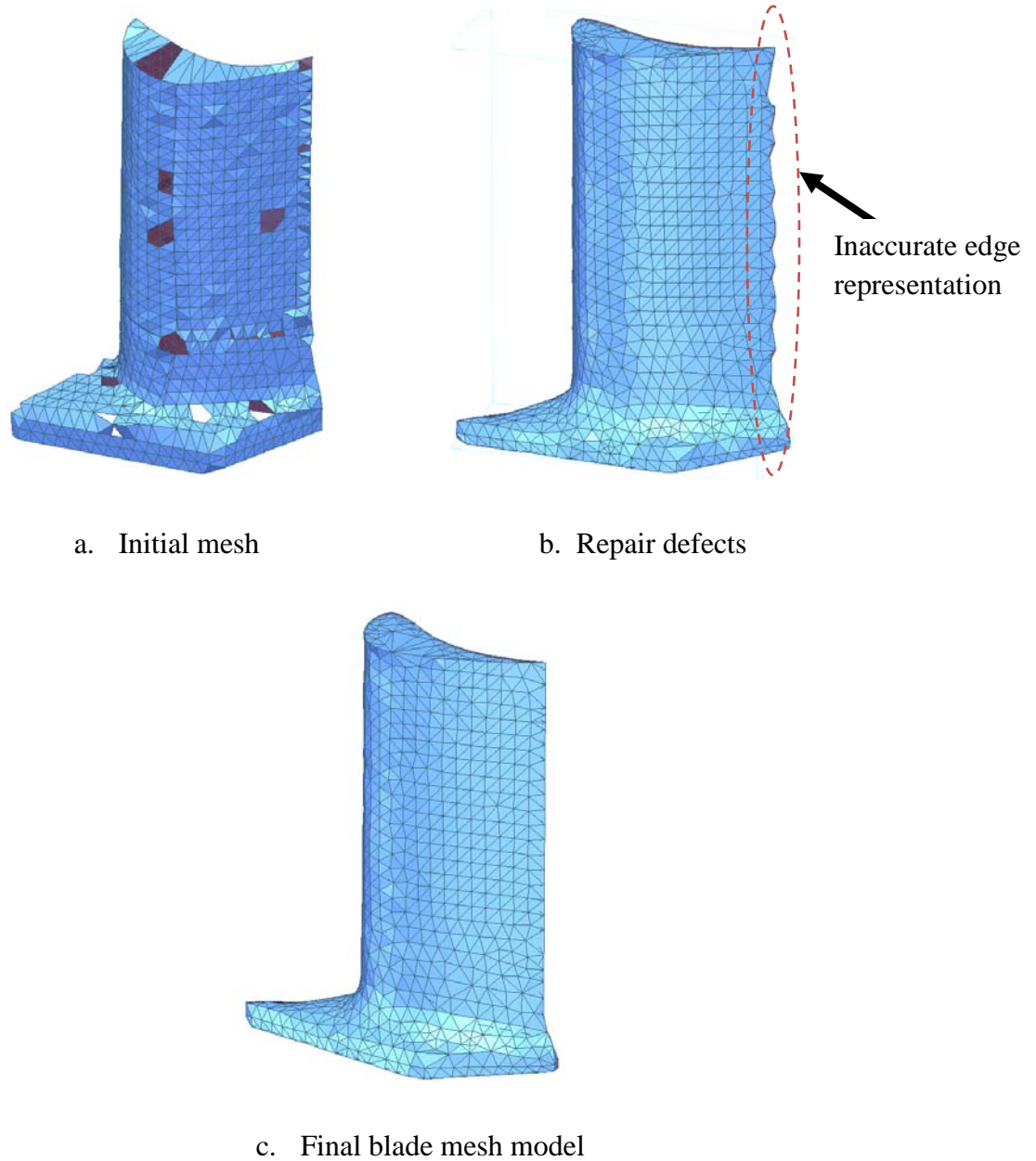
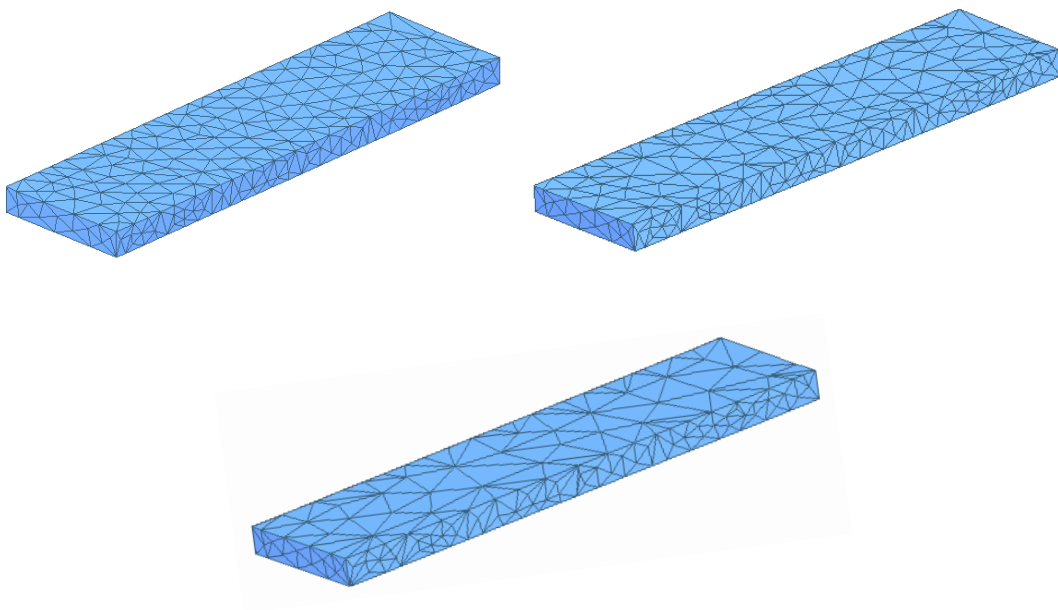


Figure 5.14 Mesh based on 2 by 2mm grid point cloud

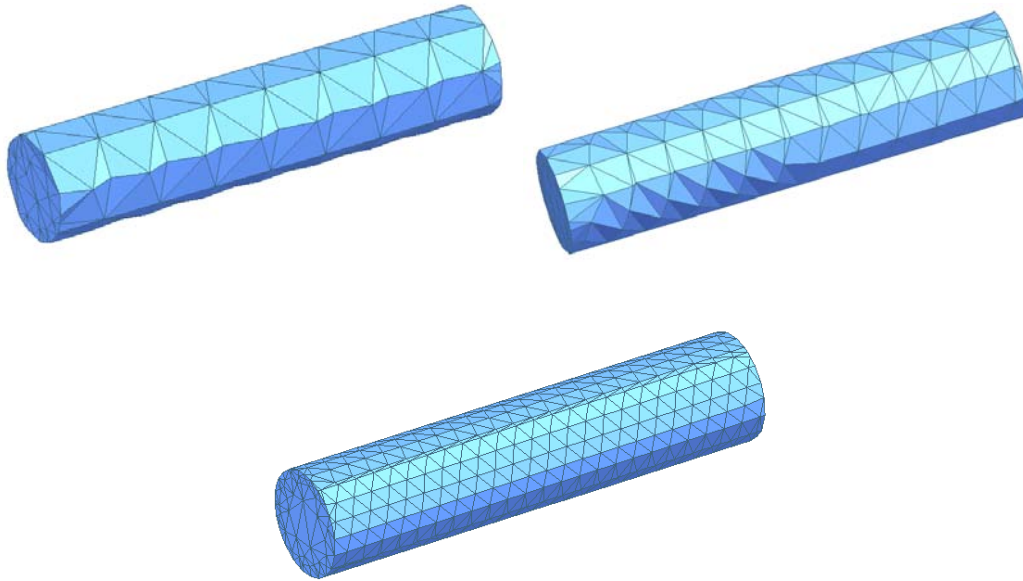
### 5.3 Mesh Results

In engineering application, it is not always easy to choose a suitable mesh for analysis which can achieve good solution for both accuracy and computing efficiency. As we collected different resolutions of point cloud of different components, here, we generated different resolution meshes of these components. Furthermore, a graded mesh of the steam turbine blade was generated. This section describes the meshes produced; the stress analysis results and computing time are compared for coarse and fine meshes in chapter 8.

For both rectangular metal plate and circular bar, three different densities of mesh were generated. A rather coarse mesh ( $4 \times 4$  mm grid), a medium mesh ( $6 \times 6$  mm grid) and a rather dense mesh ( $8 \times 8$  mm grid) of the rectangular metal plate are illustrated in figure 5.15 (a). An  $8 \times 8$ mm grid mesh, a  $5 \times 5$ mm grid mesh and a  $3 \times 3$ mm grid mesh of the bar of circular cross section are shown in figure 5.15(b).



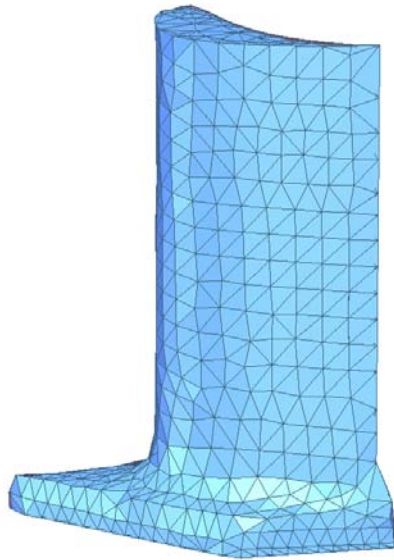
a. Rectangular metal plate



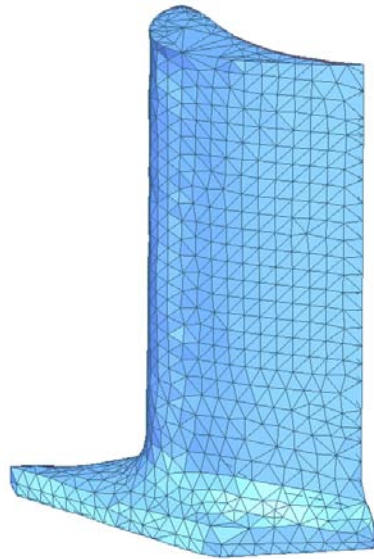
b. Circular bar

Figure 5.15 Different densities of mesh

In the mesh of turbine blade, we understand that unsmooth representation of the fillet can cause inaccurate analysis solution. In addition, a bad mesh around the fillet can also cause inaccurate results in the stress concentration. In order to better understand the fillet problem, we produced 3 meshes (figure 5.16) for the stress analysis, where approximately 2 elements are used around the fillet in the  $3 \times 3$ mm grid mesh, 3 elements are used around in the 2 by 2mm grid mesh and 4 elements are used around the fillet in the rather fine mesh ( $1 \times 1$ mm grid).



3 by 3mm grid



2 by 2mm grid



1 by 1mm grid

Figure 5.16 Final mesh models of turbine blade

Furthermore, in some cases of analysis, such as components containing cracks, holes and sharp angles, certain features are always needed to be meshed in detail to achieve sufficient accuracy. However, in an analysis, there always contain some main features which engineers are concerned about, but also contain features of less interest. Thus,

using a fine mesh around the features of most concern and a coarse mesh around the areas of less interest can make the analysis much more efficient. We produced a graded mesh model (figure 5.17) with a high mesh density around the fillet as the area we are concerned about the accuracy, and reduced the density over the blade surface along the length to the tip. We expect this can achieve the same level of accuracy in the interesting area as the fine mesh but reduce the computational time to make the process more efficient.

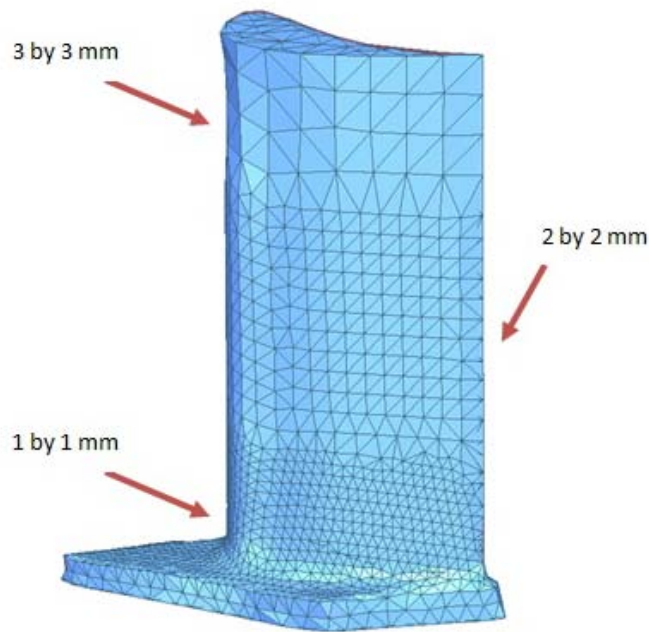


Figure 5.17 Graded mesh for turbine blade

All of the meshes in this chapter were produced in the Rapidform software.

## **Chapter 6**

### **Freeform Surface Reconstruction**

The freeform surface model of a gas turbine blade was reconstructed in this chapter. There is also a discussion on the factors which affect the surfacing fitting quality. In addition, a rapid prototyped blade model was generated to determine the surface fitting accuracy against the blade. The model was also used to test the repeatability of the scanning process, and the result is shown at the end of the chapter.

#### **6.1 Freeform Surface Fitting**

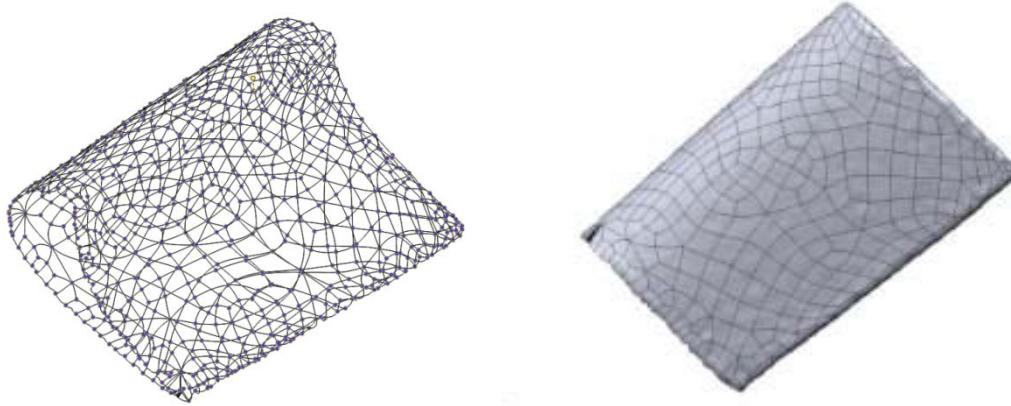
Freeform shaped parts are of great interest in many applications, either for functional or aesthetical reasons. Their relevance for industry is well-known in the design and manufacturing of products having complex functional surfaces. These parts are important components in industries such as automotive, aerospace, household and consumer products. However, with highly complex and freeform shaped parts being used in industry more and more, the conventional measurement machine is insufficient to meet the measurement demand of both accuracy and time-saving. Also, this freeform surface is relatively hard to model and reconstruct, since the shape and feature are always irregular.

As the measurement method has been described in chapter 4, here, the reverse engineering software Rapidform was employed to reconstruct the NURBS surface model of the turbine blade in this research. The procedure was as follows:

1. An initial mesh was constructed that roughly represents the blade geometry.
2. From the initial mesh, optimized triangular meshes were generated with an adaptive algorithm based on curvature and multiple density settings.
3. Based on the mesh, a NURBS surface was constructed with variable surface patch number setting and control point setting.

The first two points have been described in chapter 5. The subdivision modeling technique is used here in freeform surface fitting. This method creates a curve network based on the shape information from the mesh, which divides up the surface by means of a series of ‘characteristic curves’, which might be sharp edges, lines of large curvature and so on. This NURBS curve network is controlled by means of ‘control point’. The network can be adjusted by moving these control points to suit different features. In addition, the curve can better represent the shape information of the surface and subdivide the network into further detail level by increasing the numbers of the control point. Subdivision-based representations of complex geometry can be manipulated and rendered efficiently, and this is used as a bridge between the polygon mesh and the freeform surface.

After getting this curve network, a surface patch generation process can be performed by setting the numbers of the surface patch and its distribution. An NURBS curve representation of the blade surface based on mesh is shown in Figure 6.1(a) and NURBS surface fitting result is shown in Figure 6.2(b).



(a)

(b)

a. NURBS curve representation of the blade surface

b. NURBS surface fitting result

Figure 6.1 NURBS surface

After getting the NURBS surface model of the turbine blade, a 1:1 scaled rapid prototyped model of turbine blade obtained from  $1 \times 1$  mm resolution point cloud with 8-control points surfacing was produced (as shown in Figure 6.2). This rapid prototyped model was used for a repeatability test later in this research. The duration of each process of the experiment is shown in Table 6.1.

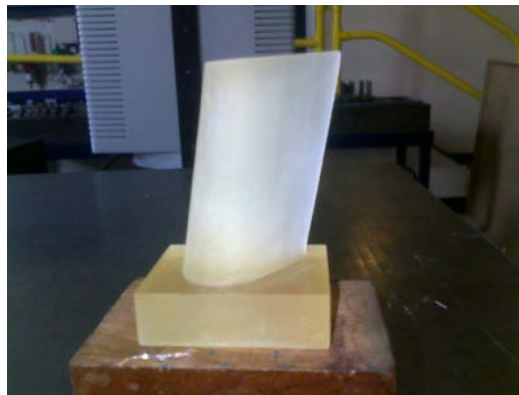


Figure 6.2 Rapid prototyped model of blade

Resolution	0.5×0.5mm	1×1mm	2×2mm
Surface scanning and point clouds alignment	21.5 min	14.85 min	9.5min
Point clouds pre-processing and mesh generation	12 min	8 min	5min
Surface reconstruction (5-control points)	5 min	4 min	N/A
Surface reconstruction (8-control points)	6 min	4.5 min	N/A
Surface reconstruction (12-control points)	8 min	7 min	N/A
Rapid prototyping	N/A	200 min	N/A
Total	N/A	238.35 min	N/A

Table 6.1 Duration of each process in the reverse engineering of turbine blade

From the above table, from measurement to obtaining a rapid prototyped model, the entire process can be finished within 4 hours.

## 6.2 Accuracy Evaluation of Surface Fitting Result

As described in section 6.1, three main factors affect the quality of the surface fitting result, which are mesh density, the number of surface patches and the number of control points in both u and v directions. In this section, the influence of these three factors upon the accuracy of the surface fitting is evaluated.

Three levels were chosen for the numbers of the surface patches (800, 400 and 100) and for numbers of the control points (12, 8 and 4) in both u and v directions. For mesh density, we compared the dense mesh model with the adaptive mesh model which was obtained in chapter 5. In addition, the uniform surface patch distribution is also compared with the adaptive surface patch distribution. The simulation results (deviation contour between the NURBS surface and the original point clouds) are shown from Figure 6.3 – 6.6.

For the effect of numbers of the surface patch affects (Figure 6.3), a  $0.5 \times 0.5$ mm grid mesh model was used, the numbers of the control point in both u and v directions are fixed to 8. The initial surface patch number started from 800. It can be seen that the surface fitting is within high accuracy, where almost the entire surface deviation are within  $\pm 0.01$ mm. We reduced the surface patch number to 400. The surface fitting quality

still remains at a high level of accuracy. However, the error around the trailing edge and the edge on the tip are slightly increased, where the maximum error is  $\pm 0.04\text{mm}$ . The last simulation investigates the effect of setting the number of surface patches to 100. Here, the simulation shows that the surface fitting quality is poor, especially the edges which are around the tip and leading edge. The maximum error is higher than  $\pm 2\text{mm}$  here.

Next, the effect of the number of control points is investigated (Figure 6.4). Again, a  $0.5 \times 0.5\text{mm}$  grid mesh model was used. The surface patch numbers are fixed to 400. The initial numbers of control point in both u and v directions are set to 12. The simulation result shows a good surface fitting quality. Almost the entire surface is within an error range of  $\pm 0.01\text{mm}$ . The number of control points was then reduced to 8, where the surface fitting quality still remains at a high level of accuracy. However, the error around the trailing edge and the edge on the tip are slightly increased the same as was found in the number of surface patch affect, where the maximum error is  $\pm 0.05\text{mm}$ . Finally, the number of control points in both u and v directions was set to 4. The simulation result shows that around 70% of the surface is within tolerance range of  $\pm 0.01\text{mm}$ . The error for the rest of the area is within  $\pm 0.04\text{mm}$ , which is acceptable.

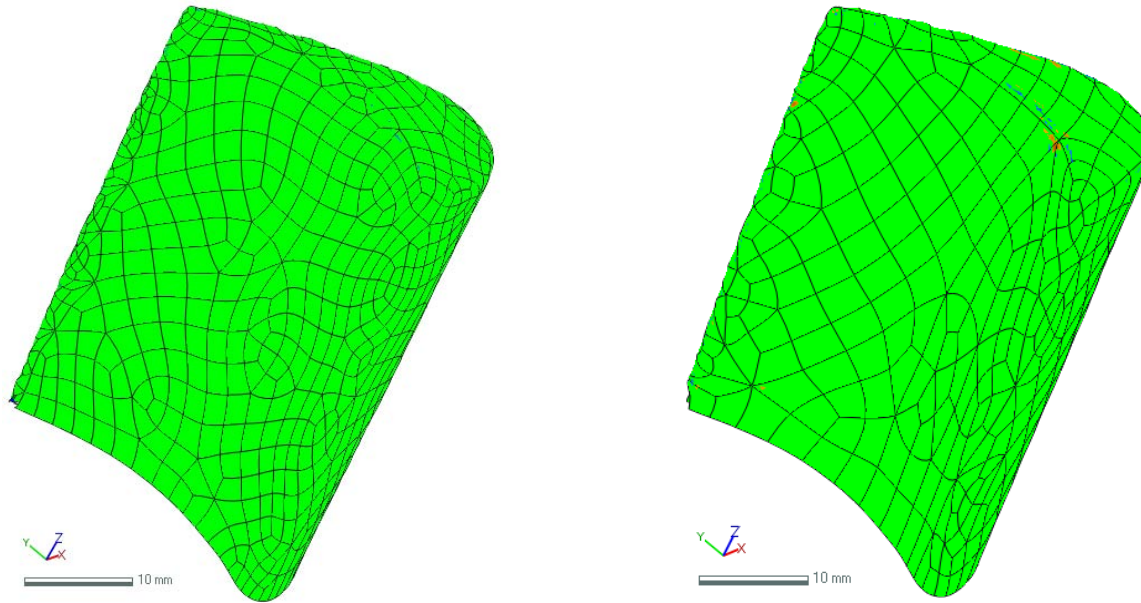
For density of mesh evaluation, we compare a dense mesh ( $0.5 \times 0.5\text{mm}$  grid) with an adaptive mesh (relative sparse mesh along the width of the sword, and fine mesh around the leading edge and tip). The result is shown in figure 6.5. The optimized mesh model gives better representation of the edge as finer meshes are used, at the same time. The surfacing result of the blade surface still shows a comparable accuracy with the dense mesh.

The effect of the surface distribution result is shown in figure 6.6. Here, an adaptive surface patch algorithm is used. Smaller and denser surface patches are generated around the sharp edges, and sparser and larger patches are generated around the area of less curvature. A better representation of the edge is found by using an adaptive surface patch distribution algorithm.

By evaluating different control parameters which have effects on the accuracy of surface fitting, it is important to choose suitable level of these parameters for saving computer

time, while obtaining sufficient level of accuracy of the surface fitting result. A greater number of surface patches and control points can give more accurate result. However, the surface fitting process is time consuming. The time taken is dependent on the specification of the computer used (processor speed and memory available). Thus, use of an adaptive mesh and surface patch distribution method can save computer time, while producing a result within sufficient accuracy.

d. 0.5mm grid point could, 800 surface patches, 8 control pointsb. 0.5mm grid point could, 400 surface patches, 8 control points



c. 0.5mm grid point could, 100 surface patches, 8 control points

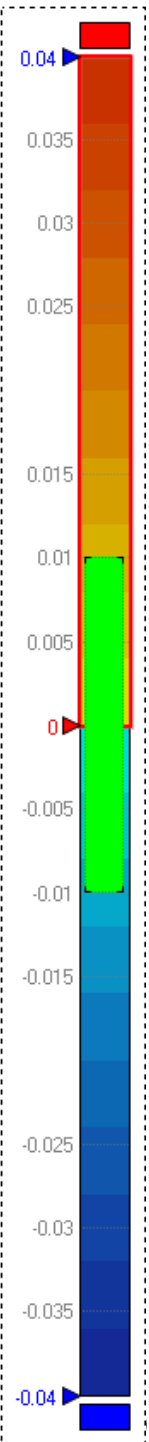
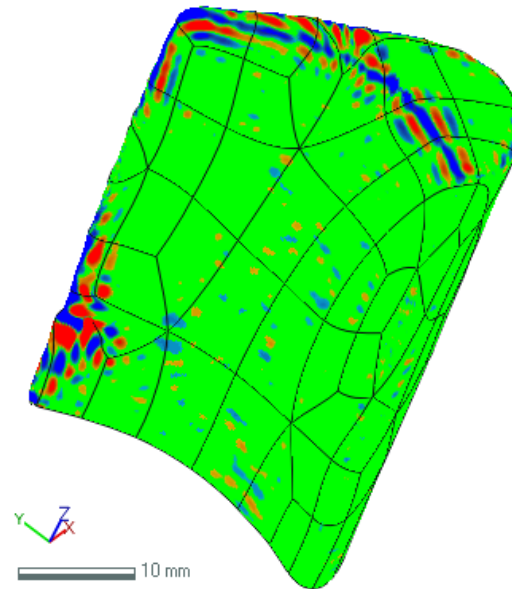
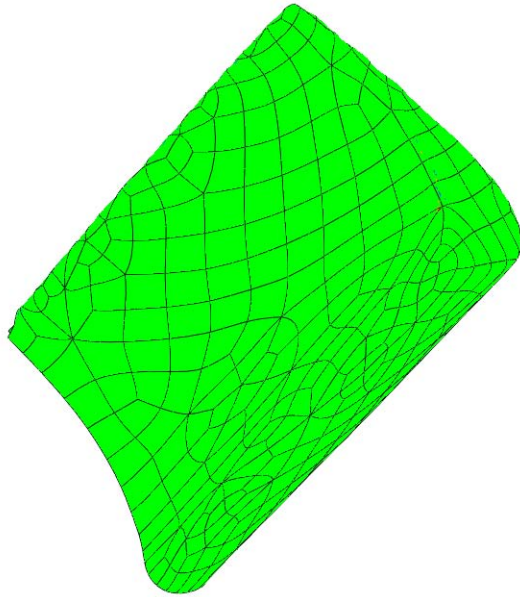
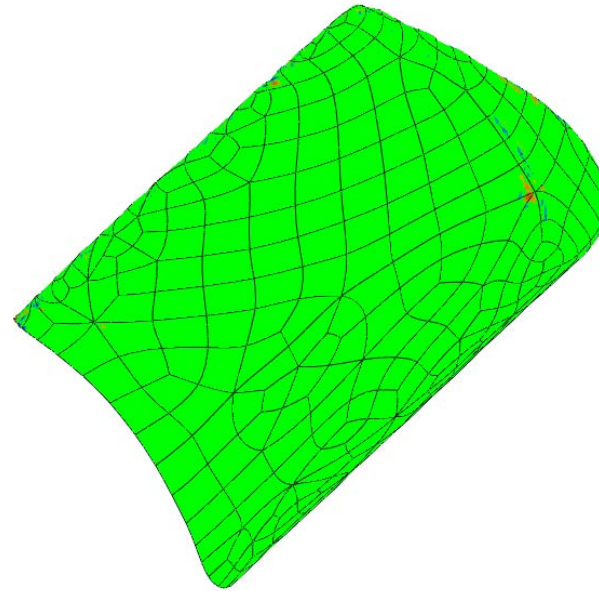


Figure 6.3 Surface patch number effect (deviation map between the point cloud and surface in mm)

c. 0.5mm grid point cloud, 400 surface patches, 12 control points



b. 0.5mm grid point cloud, 400 surface patches, 8 control points



d. 0.5mm grid point cloud, 400 surface patches, 4 control points

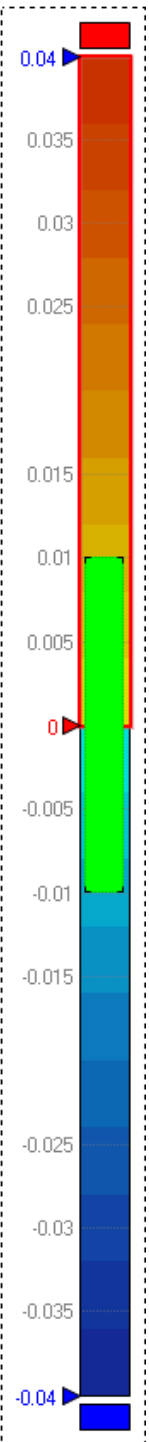
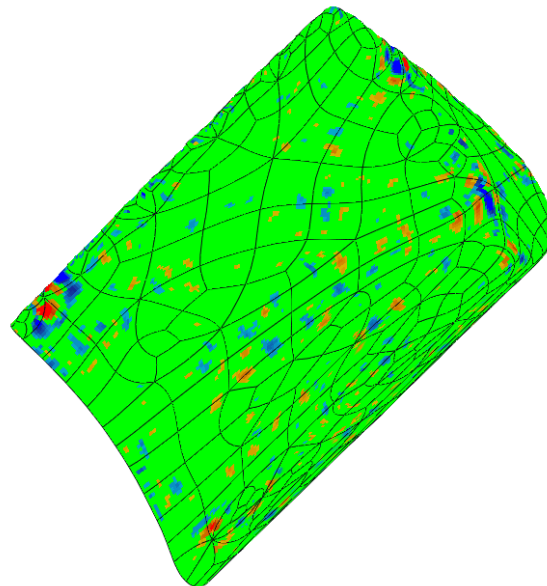
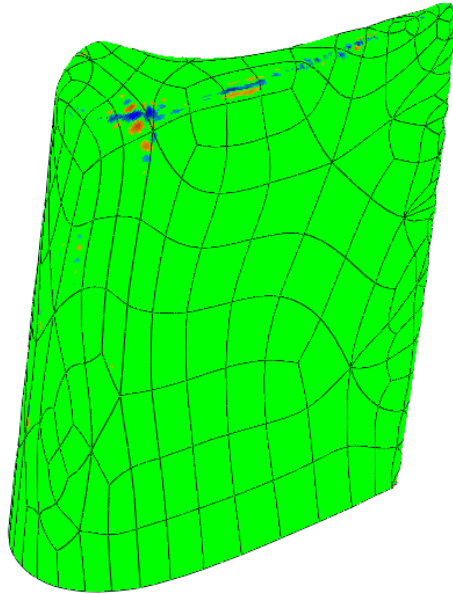


Figure 6.4 Control point effect (deviation map between the point cloud and surface in mm)

a. Dense mesh surface fitting



b. Adaptive mesh surface fitting

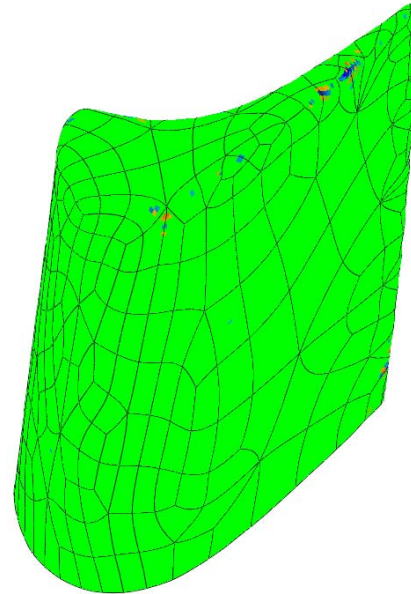
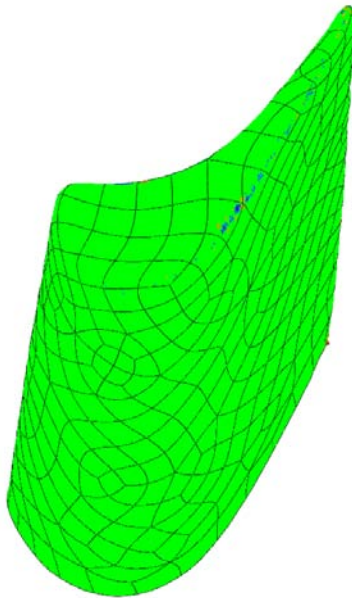


Figure 6.5 Dense mesh against adaptive mesh (deviation map between the point cloud and surface in mm)

c. Uniform surface patch



b. Adaptive surface patch

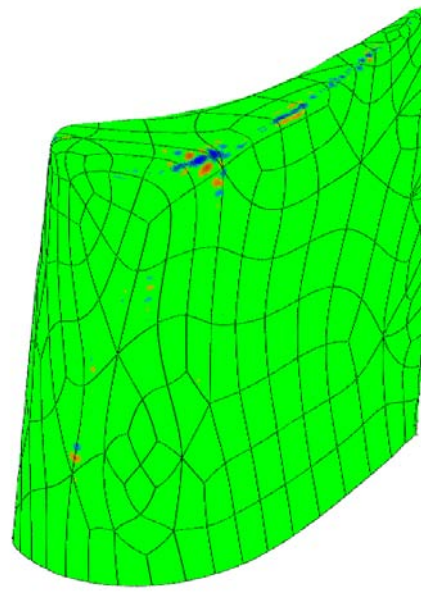
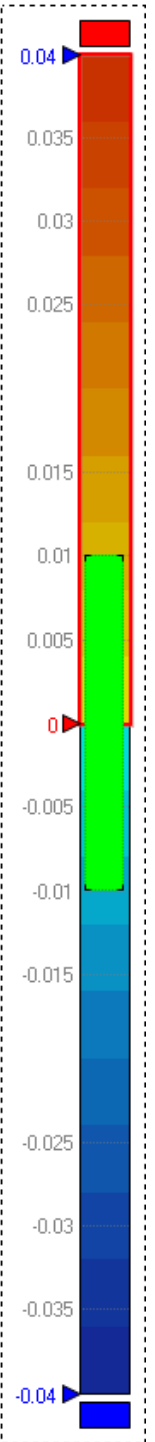


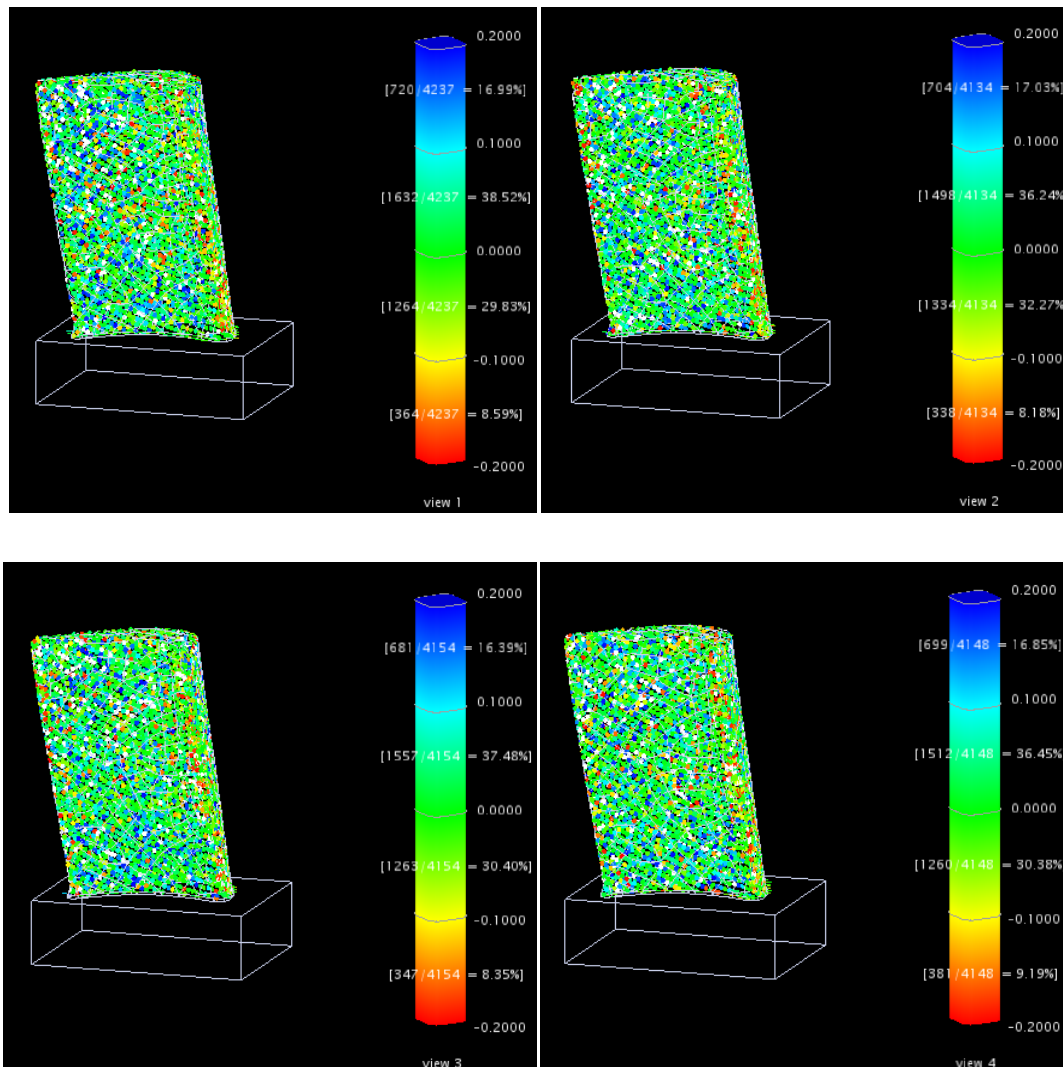
Figure 6.6 Uniform surface patch distribution against adaptive surface patch distribution



### 6.3 Repeatability Test

In order to understand better the stability of the scanning process, the rapid prototyped blade model was scanned repetitively 5 times under the same resolution setting. The scanning grid was set to 1mm on point spacing and 1mm on line spacing. The five samples of the point cloud were fitted to the same surface model, and then the errors between each sample point cloud and the CAD model were analyzed.

The surface vector intersect (SVI) contour was used to present the deviation between the point clouds and the CAD model. The SVI identifies the point at which a mathematical vector intersects an actual surface. Typically, the vector is a surface normal vector. The test results are shown in Figure 6.7.



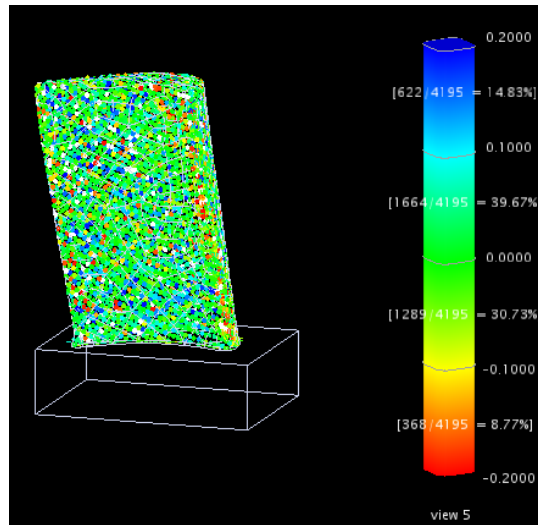


Figure 6.7 Deviation map between point cloud and the CAD model (5 samples)

Measurement results	Number of points	Points within tolerance range of $\pm 0.2\text{mm}$	Points within tolerance range of $\pm 0.1\text{mm}$	Standard deviation (mm)	Max error (mm)
Scan 1	4237	93.93%	68.35%	0.10	0.61
Scan 2	4134	95.72%	68.51%	0.11	0.44
Scan 3	4154	93.62%	67.89%	0.11	0.54
Scan 4	4148	92.87%	66.83%	0.11	0.71
Scan 5	4195	94.00%	70.39%	0.11	0.89

Table 6.2 Error distribution of five scanned samples

It can be seen from the table 6.2 that about 4150 points are collected on each measurement, the result shows that more than 92% of points are within a tolerance range of  $\pm 0.2\text{mm}$ , and more than 65% of points are within a tolerance range of  $\pm 0.1\text{mm}$ . The standard deviations of each sample are also in good agreement (0.11).

However, the result shows the maximum errors of the five scans are more than twice the 0.2mm tolerance used. There are many reasons that are likely to have caused these errors during data acquisition, such as machine calibration, measurement accuracy, noisy data and alignments of multiple views [56]. Some alignment errors cannot be avoided. Nevertheless, as the results have shown, the alignment errors in this research are negligibly small. These noisy data are always difficult to fully detect and delete completely using an automatic algorithm. So manually removing those points is essential.

## **Chapter 7**

### **BEASY Input File Generation**

In this chapter, the procedure of generating the BEASY input file is described. The repair algorithms of rectangular metal plate mesh, bar of circular cross section and steam turbine blade are also given. The boundary conditions for each case are defined. A set of pressures obtained from the commercial Computational Fluid Dynamics (CFD) software Fluent are applied as boundary conditions in a turbine blade stress analysis.

#### **7.1 Structure of BEASY input file**

The BEASY input file contains three major elements, points and elements information, boundary conditions. The points section contains x, y and z coordinates of each node which represents the geometry of the object. In the element section, each element is defined by six nodes (three corner nodes and three mid-side nodes). In the boundary condition, we use traction to define the pressure on the boundary. Traction in the normal direction is equal to the applied pressure distribution loading. For free surfaces, the traction components will be zero as there is no applied pressure.

The points and elements information are obtained from a polygon type file exported from Rapidform. This polygon file contains points and elements information in a form similar to

that required for the BEASY file, but the polygon file exported from Rapidform only contains the three corner nodes for each element. Therefore, these 3-noded elements need to be converted to 6-noded elements, by the addition of a mid-side node on each edge of the triangular elements. The procedure used is given here.

If a triangular element is defined by three corner nodes a, b and c and three mid-side nodes, d, e and f, the  $x$  coordinate of each mid-side node is given by

$$d_x^i = \frac{a_x^i + b_x^i}{2}, \quad 0 < i \leq n \quad (7.1)$$

$$e_x^i = \frac{b_x^i + c_x^i}{2}, \quad 0 < i \leq n \quad (7.2)$$

$$f_x^i = \frac{a_x^i + c_x^i}{2}, \quad 0 < i \leq n \quad (7.3)$$

where  $a_x^i, b_x^i, c_x^i, d_x^i, e_x^i, f_x^i$  is the  $x$  coordinate of each node in the number  $i$ th element, and  $n$  is total number of triangular elements.

Similar computations are used for y and z coordinates' calculation.

## 7.2 Repair Solution

As was described in chapter 5, the edge is hard to define for arectangular metal plate. Spurious notches are generated during mesh generation of a circular bar and the trailing edge need to be repaired for a steam turbine blade. The repair solution for a rectangular metal plate has been given in chapter 5. The repair solutions for a bar of circular cross section and for the blade are given here.

### 7.2.1 Bar of Circular Cross Section

The reason for the notch problem is that the nodes of the element do not lie on the cylindrical surfaces, especially the 3 mid-side nodes. In order to solve this problem, the mid-side nodes are recreated and snapped to the cylindrical surface, the algorithm is given below.

The radial coordinates of a node, measured from the axis of symmetry of the cylinder, is given by

$$r = \sqrt{b_y^i{}^2 + b_z^i{}^2} \quad (7.4)$$

The angular coordinate,  $a$ , in the circumferential direction of the cylinder, is given by

$$a = \tan^{-1} \frac{|b_z^i|}{|b_y^i|} \quad (7.5)$$

Snapping the nodes to the cylindrical surface

$$b_y^i = \begin{cases} 0.03 \cos(a), & b_y^i > 0 \text{ and } b_z^i > 0 \\ -0.03 \cos(a), & b_y^i < 0 \text{ and } b_z^i > 0 \\ -0.03 \cos(a), & b_y^i < 0 \text{ and } b_z^i < 0 \\ 0.03 \cos(a), & b_y^i > 0 \text{ and } b_z^i < 0 \end{cases} \quad (7.6)$$

$$b_z^i = \begin{cases} 0.03 \sin(a), & b_y^i > 0 \text{ and } b_z^i > 0 \\ 0.03 \sin(a), & b_y^i < 0 \text{ and } b_z^i > 0 \\ -0.03 \sin(a), & b_y^i < 0 \text{ and } b_z^i < 0 \\ -0.03 \sin(a), & b_y^i > 0 \text{ and } b_z^i < 0 \end{cases} \quad (7.7)$$

where 0.03m is the radius of the cylinder,  $b_x^i$ ,  $b_y^i$ ,  $b_z^i$ , stands for the  $x$ ,  $y$  and  $z$  coordinate of a node respectively, the range of  $i$  is set to  $0 < i \leq n$ ,  $n$  is the total number of nodes. Note that the above is the equivalent of the atan2 function in Matlab and C. The first step

is to snap the point which should be on the cylindrical surface. However, we do not want to move the points which are on the two end flat surfaces. The length of bar is 0.2675m; the range  $0.005 < b_x^i < 0.267$  selects only points between one two end surface to be moved.

The second step is to repair the cylinder edge of the two end surfaces. Here, we snap the point which is on the end surface to the edge. Nevertheless, we do not want to move the point which is ‘inside’ the end surface as moving this points will affect the mesh quality. So we only move the points which are very close to the edge. As the radius of this bar is 0.03m, we only consider snapping points radial coordinate greater than 0.025m.

If  $r > 0.025$  and  $b_x^i < 0.005$  or  $b_x^i > 0.267$

$$b_y^i = \begin{cases} 0.03 \cos(a), & b_y^i > 0 \text{ and } b_z^i > 0 \\ -0.03 \cos(a), & b_y^i < 0 \text{ and } b_z^i > 0 \\ -0.03 \cos(a), & b_y^i < 0 \text{ and } b_z^i < 0 \\ 0.03 \cos(a), & b_y^i > 0 \text{ and } b_z^i < 0 \end{cases} \quad (7.8)$$

$$b_z^i = \begin{cases} 0.03 \sin(a), & b_y^i > 0 \text{ and } b_z^i > 0 \\ 0.03 \sin(a), & b_y^i < 0 \text{ and } b_z^i > 0 \\ -0.03 \sin(a), & b_y^i < 0 \text{ and } b_z^i < 0 \\ -0.03 \sin(a), & b_y^i > 0 \text{ and } b_z^i < 0 \end{cases} \quad (7.9)$$

It is important to be aware that some small elements might be generated around the edge after repairing by this algorithm. These small elements are often poorly shaped and may affect the accuracy of the analysis. Therefore, a visual check needs to be carried out in order to make sure the mesh is of good quality. If problematic regions of the mesh are observed, they are manually repaired. In future, automation of this process would be of great value.

## 7.2.2 Steam Turbine Blade

As described in chapter 5, the representation of the trailing edge of the turbine blade remains poor after manual repair process. From the measurement, we determine that the correct  $x$  coordinate of the trailing edge is 35.328mm, and the correct  $y$  coordinate is 9.3579mm, the  $z$  coordinate does not need to be consider as the  $z$  axis is set to be parallel to the trailing edge, and the top surface of the base set to  $x$ - $y$  plane. We only consider the points which are more than 2mm above the  $x$ - $y$  plane and whose  $x$  coordinate is greater than 35mm here.

Thus to fix the trailing edge on the blade we use the following algorithm. If  $z > 2mm$ ,  $b_x^i > 35mm$  and  $0 < i \leq n$ ,  $n$  is the total number of nodes, we set

$$b_x^i = 35.328mm \quad (7.10)$$

$$b_y^i = 9.3579mm \quad (7.11)$$

where  $b_x^i$  and  $b_y^i$  stands for  $x$  and  $y$ 's coordinates of a node respectively.

Also, a visual check needs to be carried out in order to make sure the mesh is of good quality.

## 7.3 Boundary Conditions

### 7.3.1 Rectangular Metal Plate

The dimension of the rectangular metal plate is 116×32×6mm. The plate was tested as cantilever beam application. One end is fixed and normal distributed loads equal to 81081.08Pa (the total load applied to the top surface of the rectangular plate is 300N, the pressure obtained by dividing the load by the area of the top surface) are applied normal to the top surface. The Young's modulus is chosen as 210GPa and Poisson's ratio set to zero.

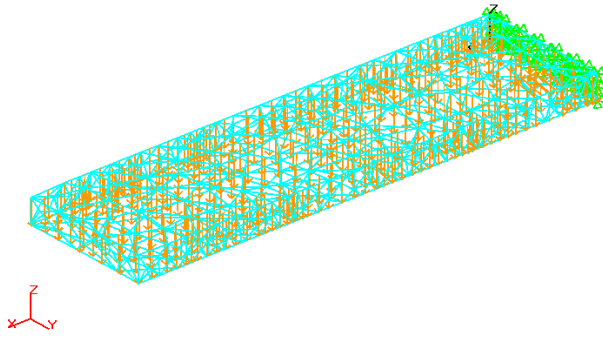


Figure 7.1 Boundary conditions for the rectangular metal plate

### 7.3.2 Bar of Circular Cross Section

The radius of the bar of circular cross section is 30mm, and the length is 267.5mm. The bar was tested as cantilever beam, where one end is fixed, and a shear force equal to 300N is applied to the other end along the  $-z$  direction. The Young's modulus is chosen as 210GPa and Poisson's ratio set to zero.

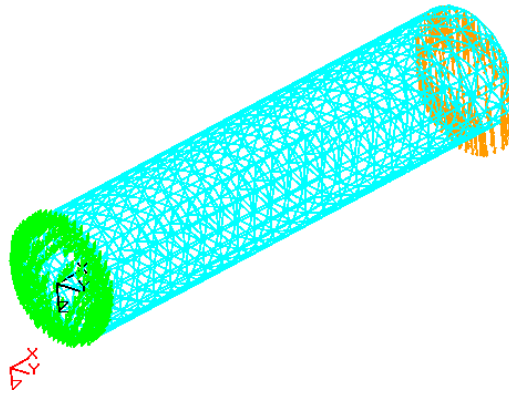


Figure 7.2 Boundary conditions for the bar of circular cross section

### 7.3.3 Steam Turbine Blade

#### 7.3.3.1 Pressure Distribution of Steam Turbine Blade Aerofoil

The pressure distribution of a steam turbine blade can be complex, and it varies according to the shape of the aerofoil and one operating condition. The pressure distribution of such a blade is important in this research for acquiring an actual stress distribution. Therefore, in order to understand and obtain the pressure distribution of the steam turbine aerofoil, the CFD technique was employed in this research.

Before performing any CFD analysis, as same as FEM/BEM analysis, creating a suitable mesh is key to achieving accurate results. A rather fine mesh needs to be generated around the area where the pressure changes rapidly in order to prescribe the pressure accurately as a boundary condition for the BEM analysis. For the area of less interest, a relatively coarse mesh can be created for computing efficiency. It can be observed that the pressure changes rapidly around the leading edge and trailing edge. Therefore, a fine mesh is generated around these two areas. Also, the boundary of the meshed computational domain was generated according to the real blade operating condition, so the upper and lower boundaries are set in locations consistent with the periodicity of the flow field.

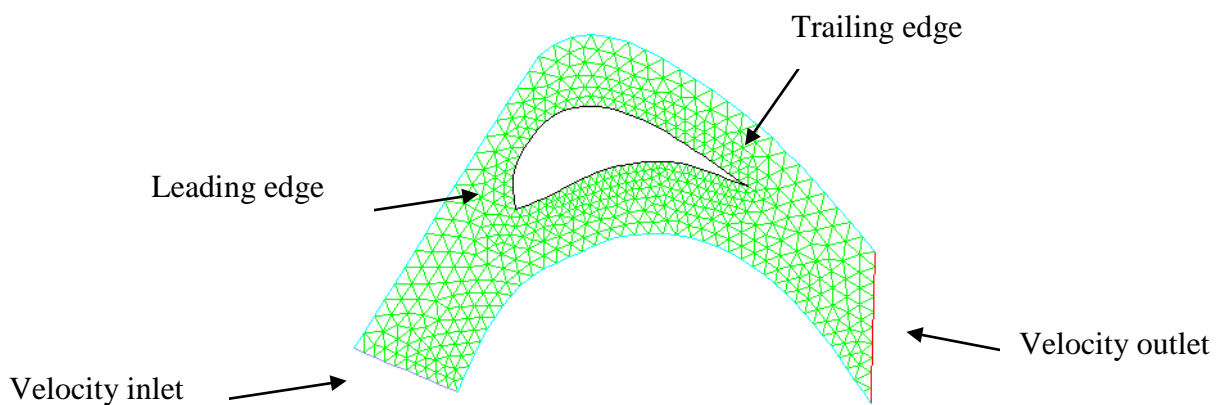


Figure 7.3 Mesh of an aerofoil

The Standard  $k-\epsilon$  model is used through the CFD simulation. This is the most broadly used model in CFD because of its low computational costs and reasonable numerical

stability. An inlet velocity of 500m/s was prescribed. The simulation result is shown in figure 7.4. The static pressure was then exported in a vector file (which contains x, y coordinate information and pressure on each point) to be used in the blade stress analysis.



Figure 7.4 Pressure distribution

### 7.3.3.2 Boundary Condition of Steam Turbine Blade

Although the main aim of this research is to explore the link between reverse engineering and BEM analysis, it is preferable to perform such studies on realistic problems of industrial relevance. Thus we focus in this section on how to prescribe realistic pressure distributions on the turbine blade, which will give realistic stress concentration effects in the fillet.

The realistic load that applies to an operating turbine blade can be very complicated. As the objective of our research is to investigate the efficiency of defining and using graded boundary element mesh, in order to simplify the loading condition, we assume that the

pressure distribution only varies along the chord direction, but remains uniform along the length of the blade.

The pressure boundary condition is applied to all elements at least 3mm above the base. The Young's modulus is chosen as 210GPa and Poisson's ratio is 0.3. As we have already obtained the pressure distribution over one section of the turbine blade, the load will be interpolated into our mesh model.

In order to apply the pressure to our mesh model, a new curve (shown in figure 7.5) was constructed between the minimum  $x$  coordinate and maximum  $x$  coordinate of the aerofoil. As the aerofoil sections are uniform (same geometry) along the blade, we only need to consider one two dimensional situation here.

The curve divides the aerofoil into two parts: the upper area is the pressure surface and the lower area is the suction surface. Also, as the export file of pressure from Fluent is a vector file, two sets of pressure distribution can be obtained. One gives the pressure with the corresponding  $x$  coordinate of pressure surface from the minimum  $x$  coordinate (point A) to maximum coordinate (point B) (shown in figure 7.5). In the similar for the other one, this gives pressures with the corresponding  $x$  coordinate of suction surface from point A to point B. Therefore, we only need to determine whether a node is on the suction surface or on the pressure surface, then the corresponding pressure can be interpolated.

The determination of the location for one node is given by

$$f(b_x^i) - b_y^i < 0, \quad 3 < b_z^i < 54mm \quad (7.12)$$

$$f(b_x^i) - b_y^i > 0 \quad 3 < b_z^i < 54mm \quad (7.13)$$

where  $b_x^i$ ,  $b_y^i$  and  $b_z^i$  represent the  $x$ ,  $y$  and  $z$  coordinates of a node respectively, the range of  $i$  is set to  $0 < i \leq n$ , and  $n$  is the total number of nodes. As the starting pressure position of the blade is 3mm above the base, the height of the blade is 54mm. The range  $3 < b_z^i < 54$  only selects the node of our consideration. If (7.12) is satisfied, it means the node is

on the pressure surface. In relative, if (7.13) is satisfied, and then the node is on the suction surface.

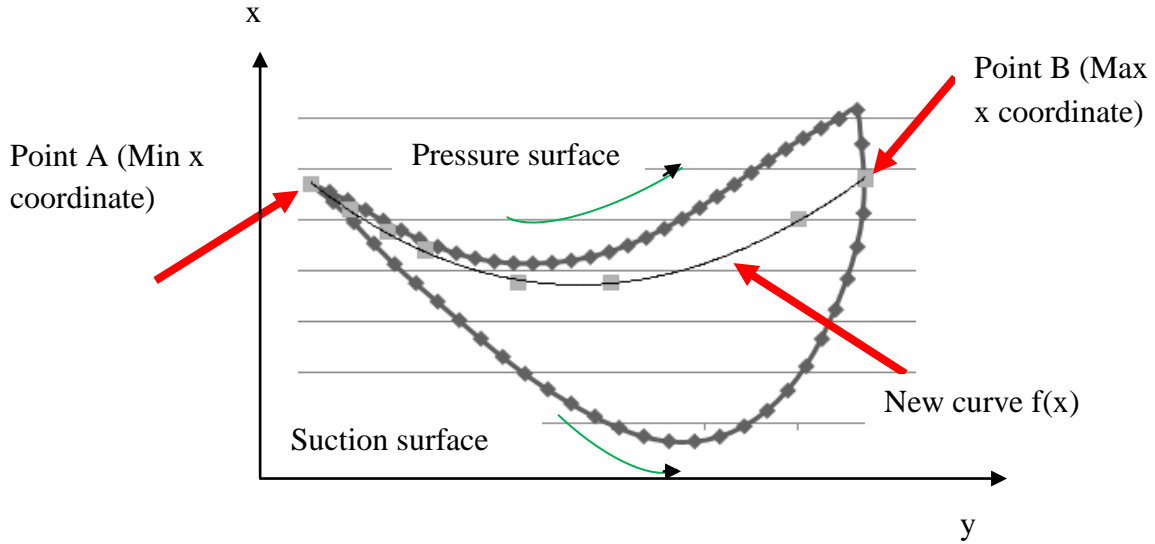


Figure 7.5 Identification for pressure and suction surfaces

If a node  $B$  is on pressure surface,

$$X_j < b_x^i < X_{j+1}, \quad 0 < i \leq n, \quad 0 < j \leq m \quad (7.14)$$

then the interpolation algorithm is given by

$$c_x^i = (P_{j+1} - P_j) \left| \frac{b_x^i - X_j}{X_{j+1} - X_j} \right| + P_j, \quad 3 < b_z^i < 54 \quad (7.15)$$

where  $X_j$  is  $x$  coordinate of a node in a set of pressure distribution of pressure surface obtained from the Fluent simulation, and  $P_j$  is the corresponding pressure of this node.  $b_x^i$  and  $b_z^i$  is  $x$  and  $z$ 's coordinates of a node respectively,  $c_x^i$  is the corresponding pressure of this node. The  $n$  in range  $0 < i \leq n$  is total number total number of nodes for mesh model and the  $j$  in range  $0 < j \leq m$  is the total number of nodes in a set of pressure distribution of pressure surface. Equation 7.13 determines the adjacent  $x$  coordinate of nodes in a set of pressure distribution of pressure surface of a node in mesh model.

Similar computations are used for the calculation of pressure on the suction surface.

The final boundary condition can be seen in figure 7.6.

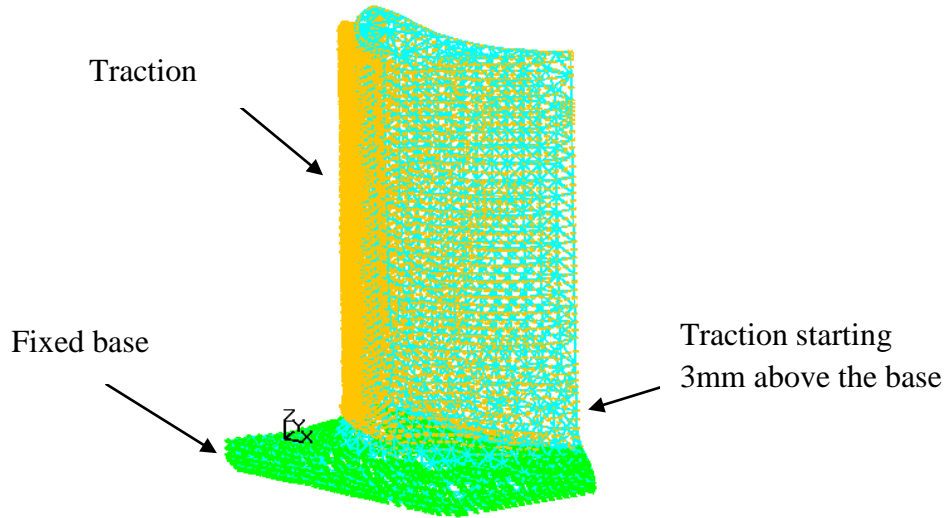


Figure 7.6 Boundary conditions for the steam turbine blade

## **Chapter 8**

### **Computational Boundary Element Stress Analysis**

In chapter 5 and 7, the mesh model and boundary conditions were introduced. In this chapter, three cases of 3D linear, static stress applications are analyzed: a rectangular metal plate, a bar of circular cross section and a steam turbine blade. The boundary element method was used to determine the principal stress distribution and displacement, and the analysis time was recorded. These results were used to demonstrate the efficiency to be gained by using graded mesh. The commercial boundary element software BEASY [5] was used to perform this study.

#### **8.1 Euler-Bernoulli Beam Theory and Timoshenko Beam Theory**

Both Euler–Bernoulli beam theory and Timoshenko beam theory allow the engineer to determine the load and deflection characteristics of a beam. However, the Euler–Bernoulli beam theory is subjected to lateral loads only. So for deep beam applications, Timoshenko beam theory is more suitable as the shear deformation is accounted for.

In our research, the principal stress and deformation of the rectangular metal plate are initially calculated by Euler–Bernoulli beam theory. For the bar of circular cross section,

as the depth of the cross section is five times less than its length, Timoshenko beam theory was used for this deep beam application.

## 8.2 Rectangular Metal Plate Stress Analysis

### 8.2.1 Euler-Bernoulli Beam Theory

The maximum principal stress of the rectangular metal plate, as calculated by Euler-Bernoulli beam theory, is given below:

$$I = \frac{bh^3}{12} \quad (8.1)$$

$$M_{max} = \frac{(l-x)^2 Pb}{2}, \quad x = 0 \quad (8.2)$$

$$\sigma_{max} = \frac{M_{max}c}{I} \quad (8.3)$$

where  $b$  is the width of the plate,  $h$  is the height of the plate,  $l$  is the length,  $P$  is the uniformly distributed load applied to the upper surface;  $c$  is the distance from the neutral axis to the point of interest and  $I$  is the second moment area of the cross section.  $x$  is the  $x$  coordinate of a point of interest,  $M_{max}$  is the maximum bending moment and  $\sigma_{max}$  is the maximum principal stress.

The maximum deflection is obtained from

$$\omega_{max} = \omega(l) = -\frac{Pbl^4}{EI} \quad (8.4)$$

where  $E$  is the Young's Modulus.

## 8.2.2 Boundary Element Simulation

As described in chapter 7, the rectangular metal plate was applied the boundary condition as a cantilever beam under a uniformly distributed load. The boundary element analysis was then performed on the meshes produced by the scanning procedure. The stress distribution contours are shown in figure 8.1 and corresponding displacements shown in figure 8.2.

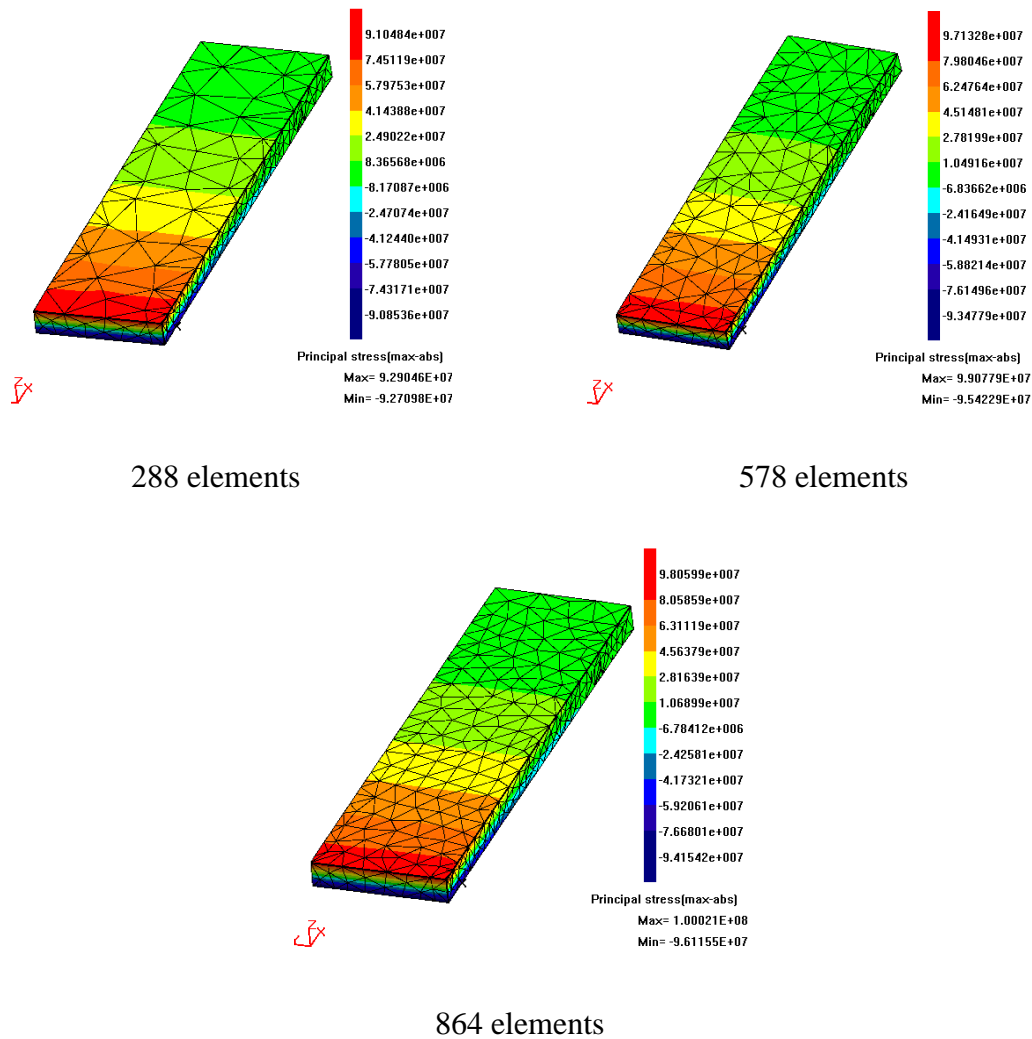
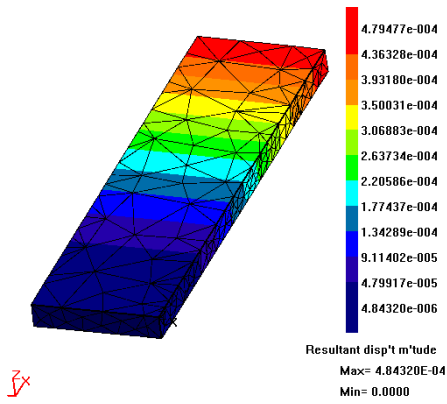
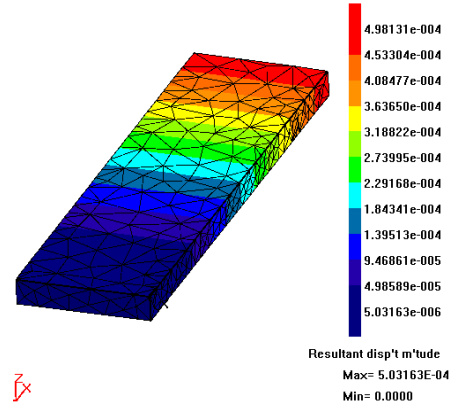


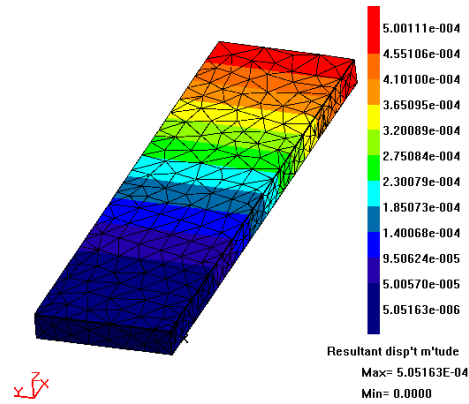
Figure 8.1 Maximum principal stress of rectangular metal plate



288 elements



578 elements



864 elements

Figure 8.2 Maximum displacement of rectangular metal plate

Reasonable stress distribution and displacement contours are obtained from the simulation. Comparison of the results of each grid model and Euler-Bernoulli Beam Theory are listed in tables 8.1, 8.2 and 8.3.

Metal Plate Stress Analysis 288 elements	BEASY Results Boundary Element Method	Euler-Bernoulli Beam Theory	Difference
Max principal stress	92.290 MPa	90.625 MPa	1.8%
Min principal stress	-92.271 MPa	-90.625 MPa	1.8%
Max displacement	0.483 mm	0.484 mm	0.2%
Simulation time	14 s	N/A	N/A

Table 8.1 Metal plate stress analysis (288 elements)

Metal Plate Stress Analysis 578 elements	BEASY Results Boundary Element Method	Euler-Bernoulli Beam Theory Results	Difference
Max principal stress	99.078 MPa	90.625 MPa	8.5%
Min principal stress	-95.423 MPa	-90.625 MPa	5.0%
Max displacement	0.503 mm	0.484 mm	3.8%
Simulation time	34 s	N/A	N/A

Table 8.2 Metal plate stress analysis (578 elements)

Metal Plate Stress Analysis 864 elements	BEASY Results Boundary Element Method	Euler-Bernoulli Beam Theory	Difference
Max principal stress	100.021 MPa	90.625 MPa	9.4%
Min principal stress	-96.116 MPa	-90.625 MPa	5.7%
Max displacement	0.505 mm	0.484 mm	3.9%
Simulation time	82 s	N/A	N/A

Table 8.3 Metal plate stress analysis (864 elements)

As shown in table 8.1, 8.2 and 8.3, the closed maximum and minimum principal stresses (4% difference maximum) of the same mesh model are obtained by using BEM. The displacement of each analysis remains stable. However, the coarsest mesh gave us the best agreement with the beam theory on both maximum principal stress and maximum displacement. For the other two simulations, the differences of displacement against beam theory are within 4%. However, the results obtained from simulation 2 and 3 seems have a high difference with the beam theory. Furthermore, the finest mesh (864 elements) required more than 5 times simulation time than the coarse mesh.

## 8.3 Circular Bar stress analysis

### 8.3.1 Timoshenko Beam Theory

The maximum principal stress of the bar of a circular cross section calculated by Timoshenko beam theory [4] is given below:

$$I = \frac{\pi r^4}{4} \quad (8.5)$$

$$M_{max} = P(l - x), x = 0 \quad (8.6)$$

$$\sigma_{max} = \frac{M_{max}c}{I} \quad (8.7)$$

The maximum deflection is obtained from

$$\omega_{max} = \omega(l) = -\frac{Pl^3}{3EI} \left[ 1 + \frac{3E}{k^2G} \frac{I}{Al^2} \right] \quad (8.8)$$

$$k = \frac{6 + 12\nu + 6\nu^2}{7 + 12\nu + 4\nu^2} \quad (8.9)$$

where  $p$  is the uniformly distributed load applied to the end surface along the  $-z$  direction,  $r$  is the radius of the cylinder,  $l$  is the length,  $x$  is the  $x$  coordinate of a point of interest,  $c$  is the distance from the neutral axis to the point of interest and  $I$  is the second moment area of the cross section.  $E$  is the Young's modulus,  $A$  is the area of the cross section,  $k$  is Timoshenko shear coefficient,  $\nu$  is Poisson's ratio,  $G$  is shear modulus.  $M_{max}$  is the maximum bending moment and  $\sigma_{max}$  is the maximum principal stress.

### 8.3.2 Boundary Element Simulation

The circular section bar was also given a set of boundary conditions modelling a cantilever beam case. The stress distribution contours are shown in figure 8.3 and corresponding displacement shown in figure 8.4.

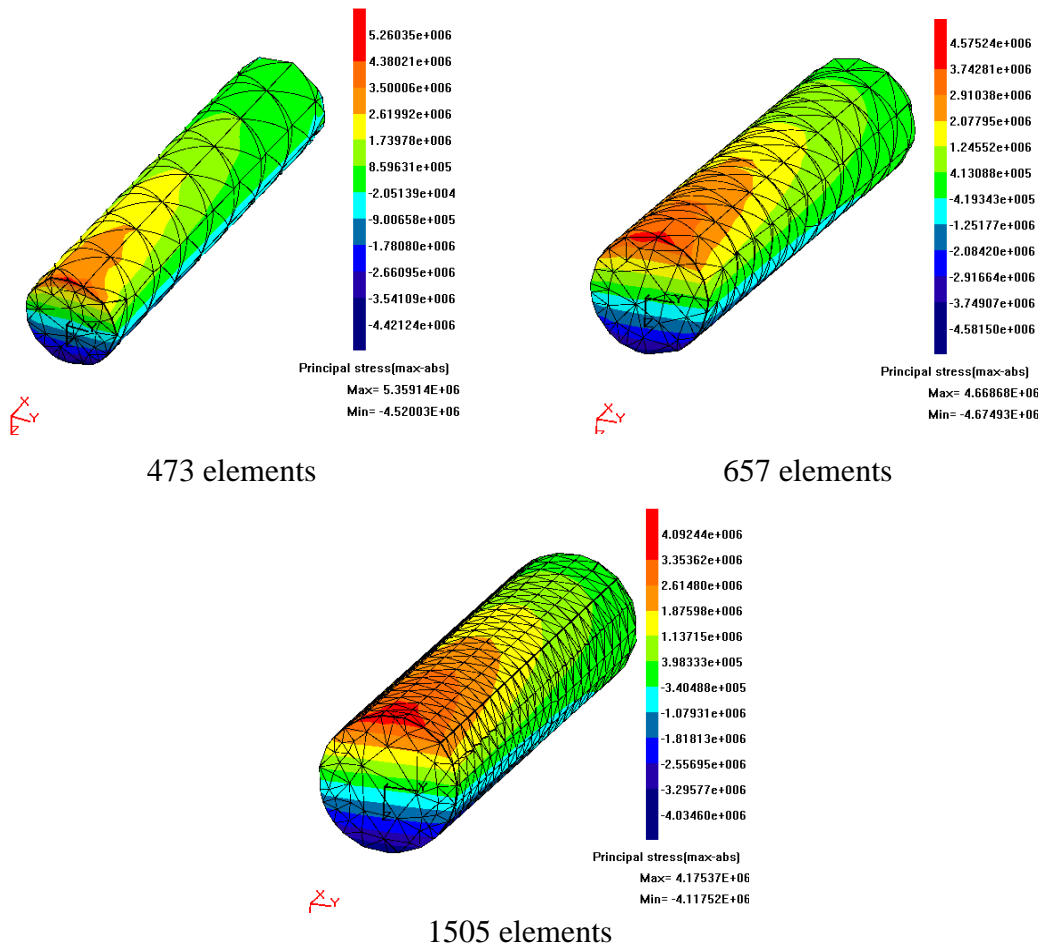
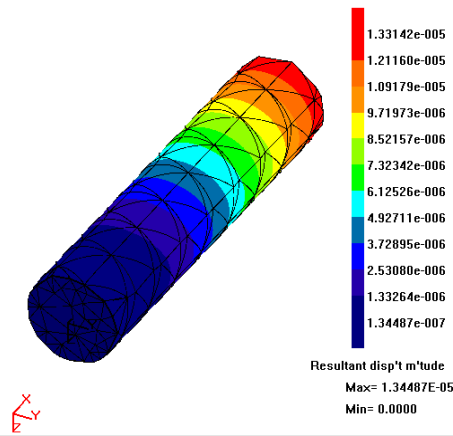
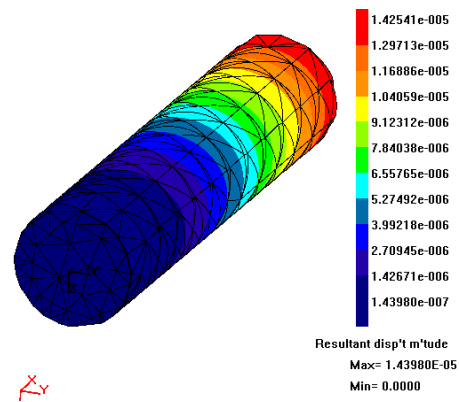


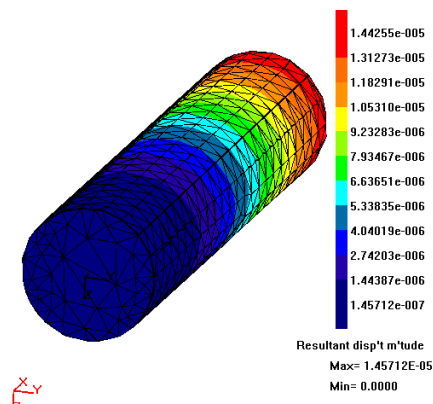
Figure 8.3 Maximum principal stress of bar of a circular cross section



473 elements



657 elements



1505 elements

Figure 8.4 Maximum displacement of bar of a circular cross section

Comparisons of the results of each grid model against Timoshenko Beam Theory are listed in tables 8.1, 8.2 and 8.3.

Circular bar Stress Analysis 473 elements	BEASY Results Boundary Element Method	Timoshenko Beam Theory	Difference
Max principal stress	5.359 MPa	3.785 MPa	29.3%
Min principal stress	-4.520 MPa	-3.785 MPa	16.3%
Max displacement	0.0134 mm	0.0143 mm	6.7%
Simulation time	19 s	N/A	N/A

Table 8.4 Circular bar stress analysis (473 elements)

Circular bar Stress Analysis 657 elements	BEASY Results Boundary Element Method	Timoshenko Beam Theory	Difference
Max principal stress	4.670 MPa	3.785 MPa	18.9%
Min principal stress	-4.675 MPa	-3.785 MPa	19.0%
Max displacement	0.0144 mm	0.0143 mm	0.7%
Simulation time	52 s	N/A	N/A

Table 8.5 Circular bar stress analysis (657 elements)

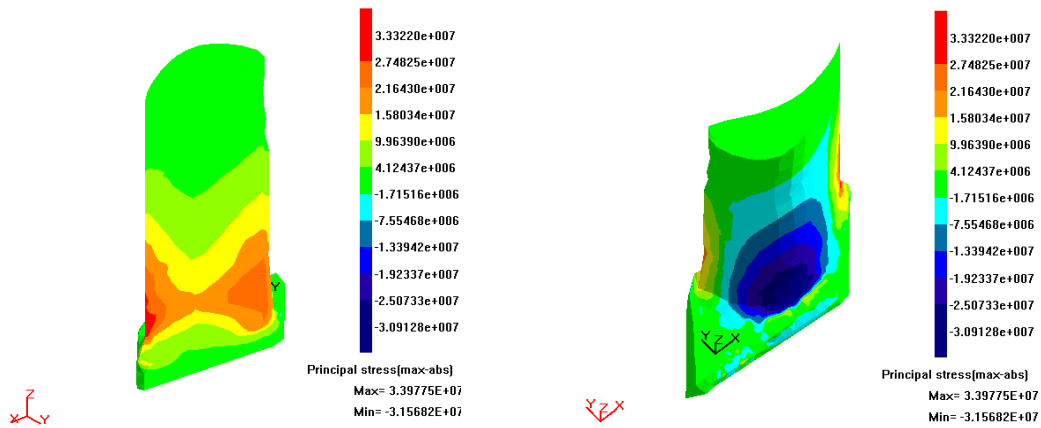
Circular bar Stress Analysis 1505 elements	BEASY Results Boundary Element Method	Timoshenko Beam Theory	Difference
Max principal stress	4.175 MPa	3.785 MPa	9.3%
Min principal stress	-4.117 MPa	-3.785 MPa	8.1%
Max displacement	0.0146 mm	0.0143 mm	2.1%
Simulation time	301 s	N/A	N/A

Table 8.6 Circular bar stress analysis (1505 elements)

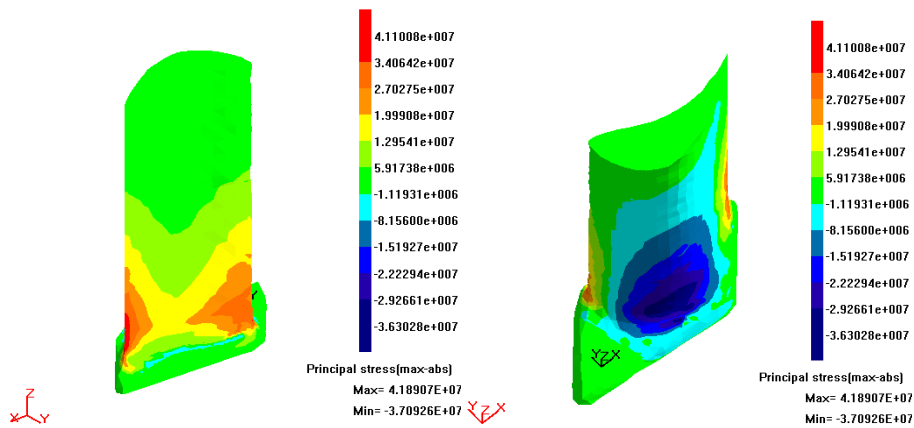
As can be seen in the above tables, the stresses of analysis 1 performed a fast simulation, but gave poor agreement with the deep beam theory (30% error). A closer analysis result was obtained from simulation 2, in which the element counts increased to 657, and which took 4 times longer than the initial mesh. The best result was shown in analysis 3, which considered the finest mesh resolution (1505 elements), but spent fifteen times more time than the coarsest mesh. However, the results still have more than 8% difference to the deep beam theory. The displacement result shows a better agreement with the deep beam theory (0.7% for 657 elements model, 2.1% for finest mesh).

## 8.4 Steam Turbine Blade Stress Analysis

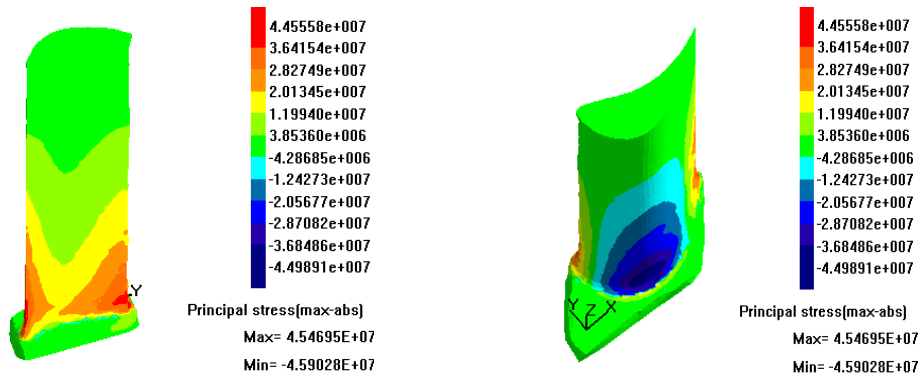
The principal stress distribution contours resulting from the four different graded meshes of the steam turbine blade are shown in Figure 8.5, and the corresponding maximum displacement contours are shown in Figure 8.6. The stress contours show that the maximum principal stress was found around the fillet close to the trailing edge on the pressure surface where the thinner geometry is located. The maximum compressive stress was found approximately in the middle of the fillet on the suction surface. All stress components decreased along the blade towards the tip. The maximum displacement occurred on the tip and decreased towards the base. All of these are consistent with expectation based on classical beam theory and the development of stress concentrations.



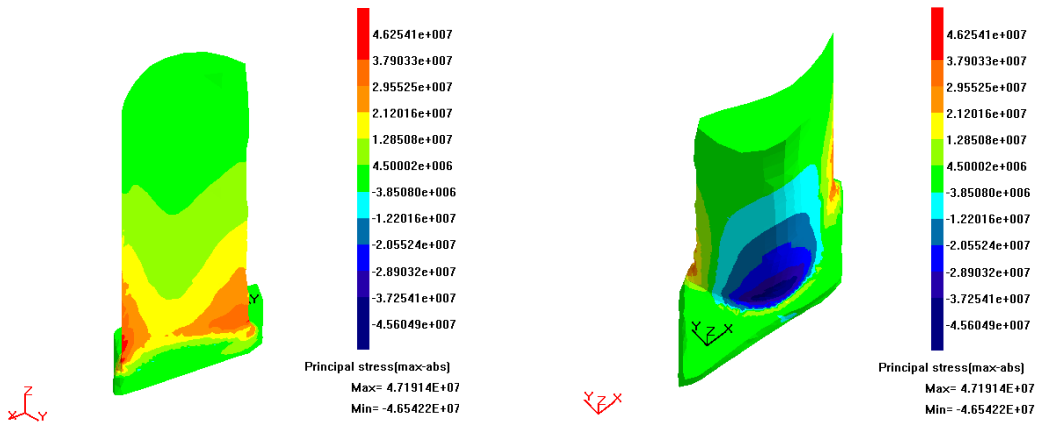
a. 3 by 3mm grid model



b. 2 by 2mm grid model

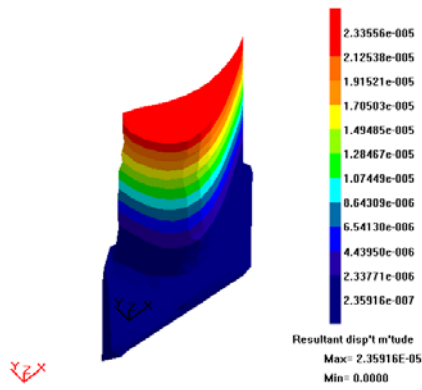


c. 1 by 1mm grid model

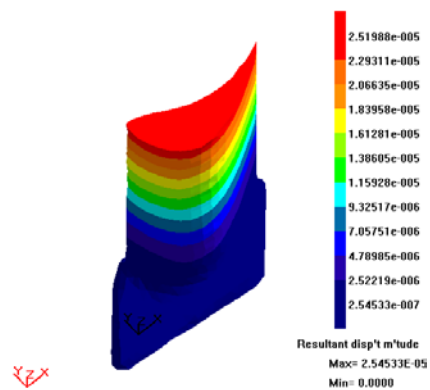


d. Graded 3-2-1model

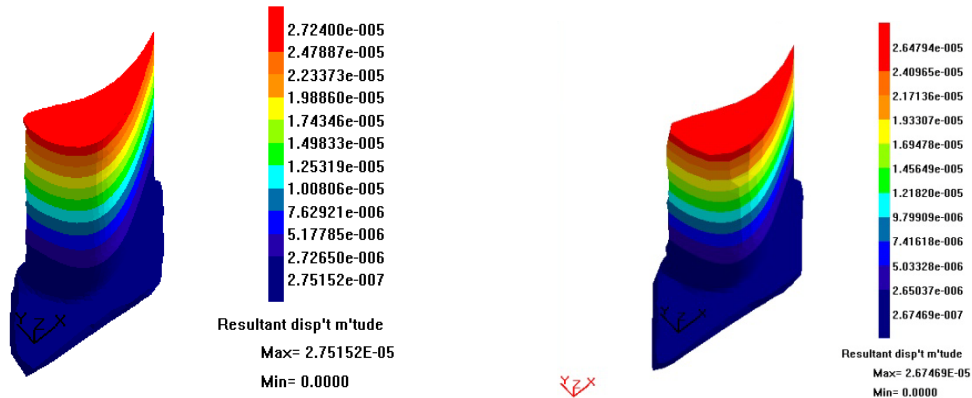
Figure 8.5 Stress distribution contours of steam turbine blade



a. 3 by 3 mm grid



b. 2 by 2mm grid



c. 1 by 1mm grid

d. Graded 3-2-1 model

Figure 8.6 Displacement Contours of steam turbine blade

	Number of elements	Normalized total force in y direction (Fy+)	Normalized Displacement	Displacement/total force in y direction (Fy+)
3×3mm grid	1368	1.0	1.0	4.27E-06
2×2mm grid	2782	1.055	1.042	4.22E-06
1×1mm grid	8044	1.078	1.169	4.62E-06
Graded grid model	3654	1.093	1.125	4.40E-06

Table 8.7 Correlation check

Several factors were analysed in order to test the convergence of the results. A particular concern was raised that the procedure for mapping pressures from the Fluent results to the BEASY analysis may have resulted in the four different models being subjected to slightly different total loads, which would explain the variation in displacements. We normalized the total force in y direction,  $F_{y+}$ , the displacement and the result per unit load, and the converged results from coarse mesh to fine mesh are shown in table 8.7. The variation in the result displacement per unit applied load is found to be within 1%. We can also see that the graded model is in good agreement with the finest mesh (1.3% difference).

	<b>Number of elements</b>	<b>Max principal stress (MPa)</b>	<b>Min principal stress (MPa)</b>	<b>Max displacement (mm)</b>	<b>Simulation time(hour)</b>
3×3mm grid	1368	33.978	-31.568	0.0024	0.33
2×2mm grid	2782	41.890	-37.093	0.0025	2.5
1×1mm grid	8044	45.470	-45.903	0.0028	21
Graded grid	3654	47.191	-46.542	0.0027	4

Table 8.8 Statistics of the major factors

The maximum and minimum principal stresses, maximum displacement and simulation time are listed in table 8.8. Unlike the result shown in Table 8.7, the maximum principal stress from the mesh 3×3 mm grid mesh and 2×2 mm grid mesh does not show a good agreement with the finest mesh (1×1mm grid) result. The displacements are remaining stable through the four analyses.

For the simulation time, the coarse mesh (3×3mm grid) took half an hour to solve the problem. It takes 5 times longer than the initial mesh to solve the problem by increasing the element counts to 2783. Also, the finest mesh (1×1mm grid) should give us the most reliable result within the four analyses. However, it took 21 hours to run this model which contains more than 8000 elements. A better solution was obtained for the graded mesh model. The principal stress variation between the graded mesh and finest mesh is 3.65%, and the maximum displacement variation is 3.7%, which shows a fair agreement. The simulation time is significantly reduced from 21 hours to 4 hours by using the graded mesh.

## 8.5 Accuracy

### 8.5.1 Element Distortion

In boundary element analysis, there are many ways in which a mesh can be inadequate for its purpose and will cause the BEM to produce inaccurate results. In addition to the mesh being simply too coarse to capture the underlying stress distribution, poor results can also be found if elements are excessively distorted. The usual causes are, firstly, the element's shape cannot produce accurate representation of the real geometry. Secondly, elements distortion presents inaccurate stress variation largely because of difficulties in performing numerical integration to derive matrix terms. And last, peak stresses on zero degree corners in 3D problem can be incorrectly reported. Figure 8.7 shows an example of element distortion causing inaccurate stress variation. Here the contour plot is shown element by element with no averaging between adjacent elements. The consequent discontinuity in stress contours at element edges is an indicator that locally the mesh is inadequate.

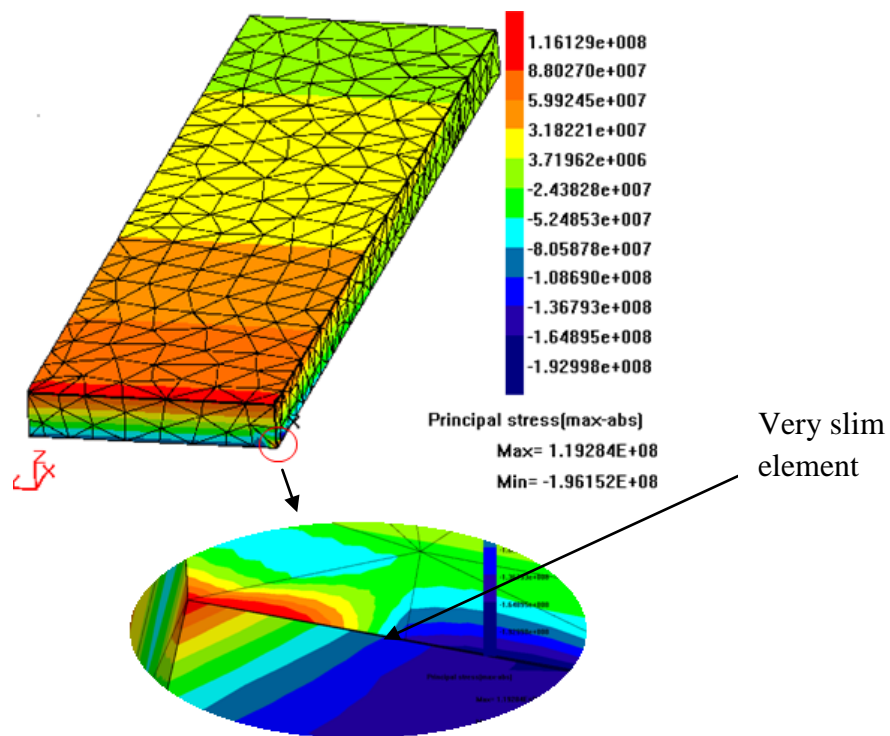


Figure 8.7 Element distortion caused by very slim element geometry

### 8.5.2 Error Estimation

It is important to assess the accuracy of the results in any analysis. In BEASY, the “stress error norm” is one of the techniques that allow us to assess the possible local error locations. The stress error norm function measures the average of the discontinuity of the stress components around the edges of an element. This is then expressed as a percentage of the maximum stress in the zone. However, it is difficult to provide general guidance on how the numerical values of this quantity vary with other measures of error. Instead, it appears that the error norm is best used to indicate which load region are likely to be most affected by errors, allowing the engineer to examine those regions more closely using other, more quantitative, error indicators.

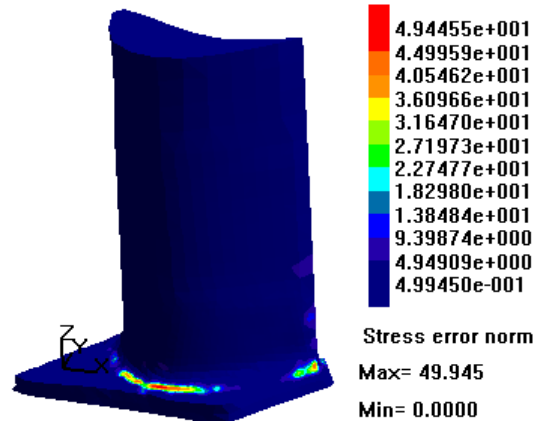


Figure 8.8 Typical stress error norm plot

## 8.6 Result Discussion and Conclusion

The analysis result of each mesh resolution of one rectangular beam shows poor agreement with Euler-Bernoulli beam theory. We deduced that the major issue causing this is that the mesh density is not high enough along the depth of the plate. It can be seen that only 2 or 3 elements are located in the depth. In addition, some areas of the geometry representation of the cross section are just represented by one large element and this can cause an inaccurate result to be encountered during simulation.

From the circular bar simulation, it can be seen that the results are getting close to the deep beam theory with the element numbers increasing in the mesh. But the finest mesh still gives an unacceptable result (8% error). We deduce that this is because the point cloud contains fewer details, especially around the edges on the two end surfaces. This will produce poor representation of the geometry during meshing.

A highly efficient solution is achieved by the graded mesh in the steam turbine blade analysis. The simulation time was significantly reduced but still remains the same level of accuracy as the finest mesh. However, the rather sparse meshes ( $3 \times 3$  mm and  $2 \times 2$  mm grids) did not show good results during the simulation. In order to better understand the problem, the force balance of the model was examined. External forces and reactions associated with element can be found by integrating the appropriate stress components over the element. Repeating these calculations over every element provides the total force in the positive y-direction and that in the negative y-direction (as well as the x and z direction). If we these forces to be equal and opposite are found, then equilibrium is satisfied. Any divergence from this equilibrium state can be viewed as a useful global error indicator. From table 8.9, it can be seen that the difference of the surface force in Y direction between the  $2 \times 2$  mm grid mesh and finest mesh is 2.25%, and the difference between the graded mesh and finest mesh is 1.17%. However, the surface force in Y direction of the  $3 \times 3$  mm grid mesh shows a large error (7.5%) against the finest mesh. This indicates that the  $3 \times 3$  mm grid mesh is generally of inadequate detail for this problem.

	<b>Element number</b>	<b>Surface force in Y+ direction (MPa)</b>	<b>Surface force in Y- direction (MPa)</b>
3*3mm grid	1368	0.56237E+03	-0.55483E+03
2*2mm grid	2782	0.59308E+03	-0.57955E+03
1*1mm grid	8044	0.60644E+03	-0.59845E+03
Graded grid model	3654	0.61351E+03	-0.61680E+03

Table 8.9 Force balance check

Furthermore, we also deduce that a few issues might cause the inaccurate results in blade analysis, or otherwise complicate comparison between different meshes.

1. The difference of the geometry of each mesh, as each mesh was generated based on a different resolution point cloud. The denser point cloud can produce a better representation of the geometry, but the coarse point cloud could not guarantee this. So it is possible to have geometry difference errors between each mesh model.
2. The coarse mesh contains fewer elements around the fillet, and especially the area close to the trailing edge and the fillet. The mesh is difficult to generate around those areas as the original point cloud contains less information.
3. As was described in chapter 7, the boundary condition is applied to all elements at least 3mm above the base. However, the sizes of the elements in each mesh model are different. Therefore, because of the geometry difference of the elements, it is possible to obtain a different applied load, thus, this might affect the accuracy of any comparison between models.

From the above simulation, it can be seen that the mesh quality has a significant effect on the accuracy of the analysis. Our approach generated different resolution boundary

element meshes based on the different grid point clouds from scanning. Inaccurate representation of the geometry is difficult to avoid for a rather coarse point cloud. However, using a graded mesh the solution can produce accurate results as well as significantly reducing the simulation time to achieve efficient analysis. We conclude with a few points that need to be concerned during mesh generation:

1. The element size should not change sharply between adjacent elements.
2. Use regular elements. Avoid elements having high aspect ratio which could cause distortion.
3. The elements need to be small enough to represent the area of interest geometrically.
4. Use a graded mesh to produce efficient analysis.

Three boundary element analyses have been performed in this exercise using meshes generated by the laser scanning technique. This includes a rectangular metal plate, a bar of circular cross section and a steam turbine blade. The major issues which contribute to the inaccurate simulation results have been found and analysed.

However, the purpose of this research is to demonstrate the effectiveness of the laser scanning technique in the generation of an efficient boundary element mesh. According to results shown in the steam turbine blade analysis, a highly efficient solution is achieved by using a graded mesh. The principal stress variation between the graded mesh and finest mesh (1×1mm grid) is 3.65%, and the maximum displacement variation is 3.7%, which shows a fair agreement. The simulation time is significantly reduced from 21 hours to 4 hours by using the graded mesh. This demonstrates that the graded mesh model of steam turbine blade using here, which was generated by laser scanning technique, is able to produce the same level of accuracy as the finest mesh, and also makes the analysis much more efficient.

## Chapter 9

### Conclusions and Recommendations

One of the main aims of this thesis was to generate efficient boundary element meshes using a graded laser scanning technique. In order to do this, a steam turbine blade was scanned by non-contact laser scanner using different scanning resolutions. From this, a graded mesh model of the blade was generated and then boundary element stress analyses were performed. A summary of the entire process is illustrated in Figure 9.1.

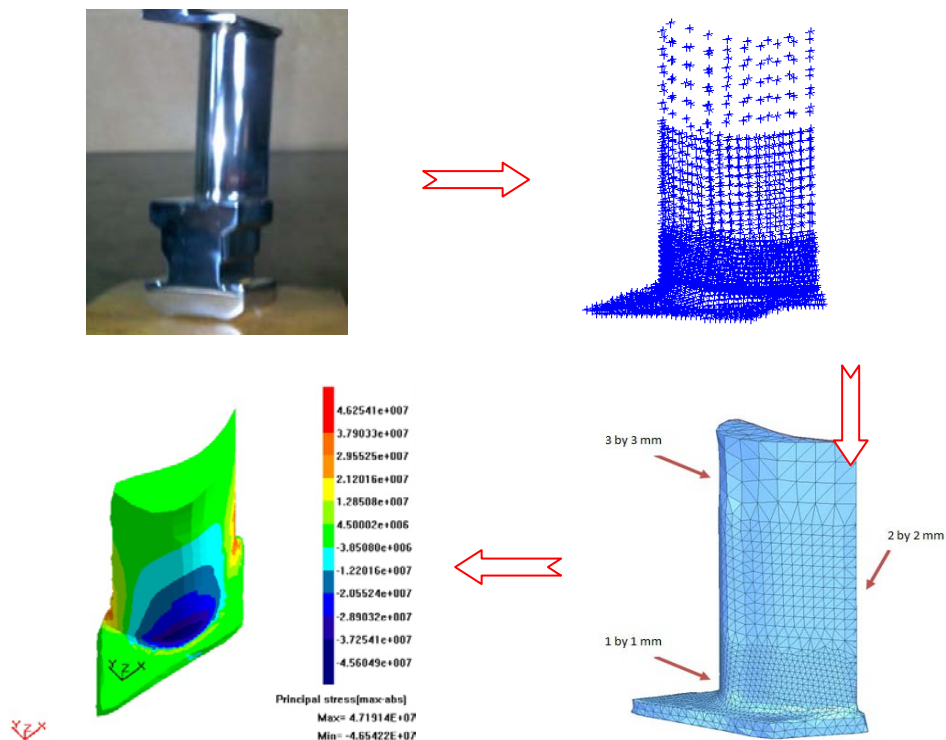


Figure 9.1 Process of integration of RE and BE stress analysis

In addition, a NURBS fitting process was applied to the gas turbine blade's freeform surface, and the consequences (in terms of accuracy) of adopting different control parameters were evaluated. A repeatability test of the measurement process was also performed.

## 9.1 Conclusions

In this work, it has been shown that laser scanning techniques can be used to provide an efficient mesh for boundary element analysis in a reverse engineering context. The integration process, linking reverse engineering procedures with the boundary element technique produces good results; particularly on graded mesh generation for stress analysis. This process avoids the necessity for a CAD-to-mesh stage, by generating the mesh model for boundary element stress analysis directly. This has obvious benefits which an object has no CAD data available. Particular features of this integrated process are:

- The following four engineering objects were selected for analysis: a rectangular metal plate, a bar of a circular cross section, a gas turbine blade and a steam turbine blade. Objects were scanned at different resolutions. From this, different grid point clouds of each object were generated. In addition, a graded point clouds of steam turbine blade was generated to enable an efficient boundary stress analysis to be performed.
- It is important to place the object at a suitable height and angle during the measurement, since the angle between the laser beam and the surface of the object has an effect on the reflected signal of the laser beam, which might affect the measurement accuracy. We suggest the object to be placed on about half height of the device, the angle should not be larger than  $30^\circ$ .
- There were difficulties in detecting the edges during measurement process, since the point cloud contains insufficient information close to the edges. The edge is

difficult to capture. We proposed several repair techniques to successfully solve this problem.

- By evaluating different control parameters which have effects on the accuracy of surface fitting, it is important to choose a suitable level of these parameters for saving computer time, while obtaining a sufficient level of accuracy of the surface fitting result. A greater number of surface patches and control points can give more accurate result. However, the surface fitting process is time consuming. It is dependent on the specification of the computer used (processor speed and memory available). Thus, use of an adaptive mesh and surface patch distribution method can save computer time, while producing a result within sufficient accuracy.
- The repeatability test shows the measurement process is stable and accurate. The results statistics show that more than 92% of points are within a tolerance range of  $\pm 0.2\text{mm}$ , and more than 65% of points are within a tolerance range of  $\pm 0.1\text{mm}$ .
- The stress analysis for the rectangular metal plate and circular bar did not show a good agreement with the engineering beam theory and deep beam theory. We deduced that the major issue causing this is the mesh density, which was not high enough over the depth of the plate. It can be seen that only 2 or 3 elements are located in the depth. In addition, some areas of the cross section are represented by one element. This can lead to an inaccurate result in the simulation.
- According to results shown in the steam turbine blade analysis, a highly efficient solution is achieved by using a graded mesh. The principal stress variation between the graded mesh and finest mesh ( $1 \times 1\text{mm}$  grid) is 3.65%, and the maximum displacement variation is 3.7%, which shows a fair agreement. The simulation time is significantly reduced from 21 hours to 4 hours by using the graded mesh.

## 9.2 Recommendations

- It is recommended that a rotatable and height-adjustable work table be used when scanning. During the measurement process, in order to capture the entire surface information, it was necessary to either move the laser scanner or rotate the measurement object. However, these two actions are rather complicated and always time consuming. These actions slowed down the scanning process. In addition, moving the measurement device also lead to errors. Placing the object onto a rotational and height adjustable working platform can make the multi view scanning easier and reduce the measurement and alignment errors.
- The stress analysis of the rectangular metal plate and the circular bar gave rise to some unacceptable results. In order to solve this problem, capturing more points around the edges can produce better mesh model. However, this requires a considerable amount of manual intervention. To avoid this, shape functions can be used to introduce additional interpolated nodes into the model, such that a detailed mesh can be generated around the required area.
- The Matlab repaired solutions have been proposed for edge and cylindrical surface repair. However, these codes are specific for the objects using in this research. Further work is required to develop a general solution for the problems.
- Further work should be undertaken to examine components containing complex surface geometries and with complex loading patterns.
- The entire process still requires a considerable amount of manual intervention. It would be better if the manual steps could be replaced by a fully automatic scheme.

## References

1. Abella, R., Daschbach, J., McNichols, R. (1994). Reverse engineering industrial applications. *ComputIndEng*; 26 (2): 381-385.
2. Argyris, J. H. (1964). Recent advances in matrix methods of structural analysis. In: Ferri, A., Küchemann, D., Smolderen, J. editors. *Progress in aeronautical science*. New York: Pergamon Press; 146-54.
3. Basilio, Ramos. Barbero. (2009). The recovery of design intent in reverse engineering problems. *Computers & Industrial Engineering*;56: 1265-1275.
4. Beam theory note, Iowa State University of Science and Technology, USA
5. BEASY software, Computational Mechanics, Southampton, UK
6. Brebbia, C. A. (1978). *The Boundary Element Method for Engineers*. Pentech Press London.
7. Benko, P., Marin, R.R., Varady, T. (2001). Algorithms for reverse engineering boundary representation models. *Computer-Aided Design*; 34 (11): 839-851.
8. Bernardini, F., Bajaj, C.L., Chen, J., Schikore, D. R. (1999). Automatic reconstruction of 3D CAD models from digital scans. *Int J Comp GeomAppl*; 9 (4&5): 327-369.
9. Besl, P. J., Jain, R. C. (1988). Segmentation through Variable-Order Surface Fitting. *IEEE PAMI*; 10 (2): 167-192
10. Boissonnat, J. D. (1984). Geometric structures for three-dimensional shape representation. *ACM Trans. Graph*; 3 (4): 266-286.

11. Burge, J. H., Wyant, J. C. (2004). Use of Computer Generated Holograms for Testing Aspheric Surfaces. *Proc. of the ASPE Winter Top. Meeting*. North Carolina, USA.
12. Campbell, R. J., Flynn, P. J. (2001). A survey of free-form object representation and recognition techniques. *Comput Vision Image Understanding*; 81 (2): 166-210.
13. Cervera, E., Trevelyan, J. (2005). Evolutionary structural optimisation based on boundary representation of NURBS. Part II: 3D algorithms. *Computers and Structures*; 83: 1917–1929.
14. Cha, C.Y., Iyer, S. V., Trevelyan, J. A comparison of convergence and modelling times for Cathode Ray Tube stress analysis with the Finite Element and Boundary Element Methods.
15. Chen, L. C., G. C. I. Lin. (2000). Reverse engineering in the design of turbine blades – a case study in applying the MAMDP. *Robotics and Computer-Integrated Manufacturing*;16: 161-167.
16. Chen, L. C., Lin, G. C. I. (1997). A Vision-aided reverse engineering approach to reconstructing freeform surfaces. *Robotics & Computer-Integrated Manufacturing*; 13 (4): 323-336.
17. Cheng, Y. Y., Lib, J. Y., Fok, S. L., Cheung, W. L., Chow, T. W. (2010). 3D FEA of high-performance polyethylene fiber reinforced maxillary dentures. *Dental Materials*; 26 (9): 211-219.
18. Chivate, P. N., Puntambekar, N. V., Jablokow, A. G. (1999). Extending surfaces for reverse engineering solid model generation. *Computers in Industry*; 38: 285-294.
19. Choi, B., Shin. H., Yoon, Y., Lee, J. (1998). Triangulation of scattered data in 3D space. *Comput Aided Des*; 20: 239-248.
20. Clough, R. W. (1960). The finite element method in plane stress analysis. *In: Proceedings, American Society of civil engineers 2nd conference on electronic computation*; 345–78.

21. Cruse, T. A. (1968). A direct formulation and numerical solution of the general elastodynamic problem II. *Journal of Math. Analysis and Applications*; 22.
22. Curless, B., Levoy, M. (1996). A volumetric method for building complex models from range images. *Proc ACM SIGGRAPH*; 303-312.
23. Danon, D. J., Brebbia, C. A., Adey, R. A. (1982). BEASY. A Boundary Element Analysis System, from Finite Element Systems Handbook. Springer Verlag and Computational Mechanics Publications.
24. Eyup, Bagci. (2009). Reverse engineering applications for recovery of broken or worn parts and re-manufacturing: Three case studies. *Advances in Engineering Software*; 40: 407–418.
25. Fredholm, I. (1903). Sur uneclasse d'equations fonctionnelles. *Acta Math*; 27: 365-390.
26. Goh, J. C. H., Lee, P. V. S., Toh, S. L., Ooi, C. K. (2005). Development of an integrated CAD–FEA process for below-knee prosthetic sockets. *Clinical Biomechanics*; 20: 623–629.
27. Guo, B. (1997). Surface reconstruction: from points to splines. *Computer-Aided Design*; 29 (4): 269-277.
28. Hoppe, H., DeRose, T., Duchamp, T., McDonald, J., Stuetzle, W. (1992). Surface reconstruction from unorganised points. *Comput Graphics (Proc SIGGRAPH)*; 71-78.
29. Hoppe, H., DeRose, T., Duchamp, T., McDonald, J., Stuetzle, W. (1993). Mesh optimization. *Computer Graphics (SIGGRAPH'93 Proceedings)*; 27: 19-26.
30. Hughes, T. J. R., Cottrell, J. A., Bazilevs, Y. (2005). Isogeometric analysis: CAD, finite elements, NURBS, exact geometry and mesh refinement. *Comput. Methods Appl. Mech. Engrg.* 194: 4135–4195.

31. Heinrich, Schwenke., Ulrich, Neuschaefer. Rube. Tilo, Pfeifer., Horst, Kunzmann. (2002). Optical Methods for Dimensional Metrology in Production Engineering. *CIRP Annals – Manufacturing Technology*; 51(2): 685-699.
32. Jarvis, R. A. (1983). A Perspective on Range Finding Techniques for Computer Vision. *IEEE PAMI*; 5 (2): 122-139.
33. Jaswon, M. A. (1963). Integral equation methods in potential theory I. *Proc. Royal Soc. Ser. A*; 275: 23-32.
34. Jun, Y. (2005). A piecewise hole filling algorithm in reverse engineering. *Computer-Aided Design*; 37: 263-270.
35. KubiakSz, J., Segura, J. A., Gonzalez R, G., García, J. C., Sierra E. F., Nebradt, G. J., Rodriguez, J. A. (2009). Failure analysis of the 350MW steam turbine blade root. *Engineering Failure Analysis*; 16: 1270–1281.
36. Lachat, J. C., Waston, J. O. (1976). Effective numerical treatment of boundary integral equations. *International Journal for Numerical Methods in Engineering*; 10: 991-1005.
37. Lee, K. H., Park, H., Son, S. (2001). A Framework for Laser Scan Planning of Freeform Surfaces. *Int J AdvManufTechnol*; 17: 171-180.
38. Lin, Y. P., Wang, C. T. and Dai, K. R. (2005). Reverse engineering in CAD modelreconstruction of customized artificial joint. *J Medical Engineering and Physics*; 27: 189-193.
39. Liu, Z., Wang, L., Lu B. (2006). Integrating cross-sectional imaging based reverse engineering with rapid prototyping. *Computers in Industry*; 57: 131-140.
40. LR-200 system guide. (2004). Leica Grosystems, UK.
41. MacGovern, A.J., Wyant, J.C. (1971). Computer Generated Holograms for Testing Optical Elements. *Applied Optics*; 10: 619-624.

42. Mucke, E. P. (1995). A robust implementation for three-dimensional Delaunay triangulations. *Proceedings of the First International Computational Geometry Software Workshop*; 70-73.
43. M. Salman A. Mansor. Free-Form Surface Models Generation Using Reverse Engineering Technique - An Investigation. University of Manchester, UK
44. Pfeifer, T., Evertz, J., Tutsch, R., Rothe, R. (1993). Testing aspherics without rotational symmetry using a Fizeau interferometer with computer-generated holograms. *Proc. SPIE*; 216-223.
45. Piegl, Les., Tiller, Wayne. (1997). The NURBS book. 2. ed. Springer Verlag, Germany.
46. Rizzo, R. J. (1967). An integral equation approach to boundary value problems of classical electrostatics. *Quarterly of Applied Mathematics*; 25: 83-95.
47. Sang, C. Park., Chang,Minho. (2009). Reverse engineering with a structured light system. *Computers & Industrial Engineering*; 57 (4) : 1377-1384
48. Sansoni, G., Docchio, F. (2004). Three-dimensional optical measurements and reverse engineering for automotive applications. *J Robotics and Computer-Integrated Manufacturing*; 20: 359-367.
49. Savio, E. De Chiffre, L., Schmitt, R. (2007). Metrology of freeform shaped parts. *CIRP Annals – Manufacturing Technology*; 56 (2): 810-835.
50. Schroeder, W. J., Zarge, J., Lorensen, W. E. (1992). Decimation of triangle meshes. *Computer Graphics (SIGGRAPH'92 Proceedings)*; 26: 65-70.
51. Smith, D. R., Kanade, T. (1985). Autonomous Scene Description with Range Imagery. *CVGIP*; 31(3): 322-334.

52. Sokovic, M. and Kopac, J. (2006). RE (reverse engineering) as necessary phase by rapid product development. *Journal of Materials Processing Technology*; 175: 398-403.
53. Symm, G. T. (1963). Integral equation methods in potential theory II. *Proc. Royal Soc. Ser. A*. 275: 33-46.
54. Tai, C. C, Huang, M. C. (2000). The processing of data points basing on design intent in reverse engineering. *International Journal of Machine Tools & Manufacture*; 40: 1913-1927.
55. Turner, M. J., Clough, R. W., Martin, H. C, Topp, L. J. (1956). Stiffness and deflection analysis of complex structures. *J Aero Sci*; 23: 805–24.
56. Varady, T., R. R. Martin, J. Coxt. (1996). Reverse engineering of geometric models – an introduction. *Computer-Aided Design*;29 (4): 255-268.
57. Wolf, K., Roller, D., SchaÈfer, D. (2000). An approach to computer-aided quality control based on 3D coordinate metrology. *Journal of Materials Processing Technology*; 107: 96-110.
58. Woo, H., Kang, E., Wang, S., Lee, K. H. (2002). A new segmentation method for point cloud data. *International Journal of Machine Tools & Manufacture*; 42: 167-178.
59. Xie, Z. X., Zhang, J. G., Zhang, Q. M. (2005). Complete 3D measurement in reverse engineering using a multi-probe system. *International Journal of Machine Tools & Manufacture*; 45: 1474- 1486
60. Xu, L., Lin, M. X., Li, J. Q., Wang, Z. L. Chirende, B. (2008). Three-dimensional geometrical modelling of wild boar head by reverse engineering technology. *J Bionic Engineering*; 5: 85-90.
61. Yau, H., Haque, S., Menq, C. (1995). Reverse engineering in the design of engine intake and exhausts ports. *ManufSciEng*; 64: 139-148.

62. Zeid, I. (1991). CAD/CAM Theory and Practice. *McGraw-Hill, Inc.*

## Appendix 1 Rapidform Polygon Mesh File

```
#Version 2.0
Shell type : GENERIC
Projection Matrix
1.0000000000 0.0000000000 0.0000000000 0.0000000000
0.0000000000 1.0000000000 0.0000000000 0.0000000000
0.0000000000 0.0000000000 1.0000000000 0.0000000000
0.0000000000 0.0000000000 0.0000000000 1.0000000000
Number of Vertices : 238
Number of Faces : 472
Has Vertex Color : 0
Has Face Color : 0

** x, y and z coordinates of point**
283.1026159310 1.0279980084 26.7290456173
212.6700123999 -27.7663368324 11.9906717289
33.8529657392 27.4851489083 -10.4891992269
73.0707033205 -13.7800450853 -26.6290702692
282.9527751894 17.6689794549 -15.7926564777
0.0199729230 11.7617040310 23.7423944317
283.0430764181 -0.0061787391 1.4408027256
205.7408583228 8.5472853364 -28.3891371142
283.0357637131 -4.1232247075 -6.0442450700
111.2440421051 -29.2225543019 -7.6761953427
** x, y and z coordinates of point**
.
.
.
**number of the node in elements**
230 3 39
230 134 3
3 50 39
39 105 230
230 9 134
```

```

134 50 3
50 215 39
39 172 105
105 161 230
230 161 9
.
.
.
**number of the node in elements**

```

## Appendix 2 Matlab Code for Cylinder Repair

%Generate bar BEASY input file, a translation from Rapidform's polygon output

```

%define variables
E=210000000000;           %YOUNGS_MODULUS
v=0;                     %POISSONS_RATIO
P=107000;                 %Load

```

%calculation of mid points on triangle's edges

%open files of elements and points

```

loadbar_elements5.txt;
loadbar_points5.txt;
A = bar_elements5 + 1;
B = bar_points5;
[m,x] = size(A);
[n,y] = size(B);

```

%ordering the new mid points

```

for i = 1:1:n;           %n is the quantity of points
for j = 1:1:n;
matrix(i,j) = 0;
end;
end;

```

```

pp = n;
for i = 1:1:m;           %m is the quantity of elements
temp = A(i,:);
    p1 = temp(1);
    p2 = temp(2);
    p3 = temp(3);
if matrix(p1,p2) == 0
matrix(p1,p2) = pp+1;
matrix(p2,p1) = matrix(p1,p2);

```

```

pp = pp+1;
end;
if matrix(p2,p3) == 0
matrix(p2,p3) = pp+1;
matrix(p3,p2) = matrix(p2,p3);
pp = pp+1;
end;
if matrix(p1,p3) == 0
matrix(p3,p1) = pp+1;
matrix(p1,p3) = matrix(p3,p1);
pp = pp+1;
end;
C(i,:) = [matrix(p1,p2) matrix(p2,p3) matrix(p3,p1)];
end
D = [A,C];           %D is a new matrix contains notes and new midpoints

```

```

%calculate the coodinates of the mid points

```

```

k = n;
for i = 1:1:k;
for j = 1:1:k;
if matrix(i,j)>0
    B(matrix(i,j,:)) = (B(i,:)+B(j,:))/2;
end;
end;
end;

```

```

[k,o]=size(B);

```

```

%optimize model shape

```

```

for i = 1:1:k;
if B(i,1) > 0.005 && B(i,1) < 0.281;
radius = sqrt(B(i,2).^2+B(i,3).^2);
    a = atan(abs(B(i,3))/abs(B(i,2)));
if B(i,2) > 0 && B(i,3) > 0;
B(i,2) = 0.03 * cos(a);
B(i,3) = 0.03 * sin(a);
end
if B(i,2) < 0 && B(i,3) > 0;
B(i,2) = -0.03 * cos(a);
B(i,3) = 0.03 * sin(a);
end
if B(i,2) < 0 && B(i,3) < 0;
B(i,2) = -0.03 * cos(a);
B(i,3) = -0.03 * sin(a);
end
if B(i,2) > 0 && B(i,3) < 0;

```

```
B(i,2) = 0.03 * cos(a);
B(i,3) = -0.03 * sin(a);
end
end
end
```

```
%Boundary condition
```

```
[n,x] = size(B);
[m,y] = size(D);
```

```
q = 1;
r = 1;
h = 0;
for i = 1:1:m;
temp = D(i,:);
    P1 = temp(1);
    P2 = temp(2);
    P3 = temp(3);
    P4 = temp(4);
    P5 = temp(5);
    P6 = temp(6);
    f = 0;
    g = 0;
if B(P1,1) < 0.006
    f = f + 1;
end
if B(P1,1) > 0.2724
    g = g + 1;
end
if B(P2,1) < 0.006
    f = f + 1;
end
if B(P2,1) > 0.2724
    g = g + 1;
end
if B(P3,1) < 0.006
    f = f + 1;
end
if B(P3,1) > 0.2724
    g = g + 1;
end
if B(P4,1) < 0.006
    f = f + 1;
end
if B(P4,1) > 0.2724
```

```

    g = g + 1;
end
if B(P5,1) < 0.006
    f = f + 1;
end
if B(P5,1) > 0.2724
    g = g + 1;
end
if B(P6,1) < 0.006
    f = f + 1;
end
if B(P6,1) > 0.2724
    g = g + 1;
end
if f > 4
W(q,:) = [i h hhhh h];
    q = q + 1;
end
if g > 4
    Q(r,:) = [i P PPPP P];
    r = r + 1;
end
end

[m,x] = size(B);
[n,y] = size(D);

for i = 1:1:m;
F(i,:) = i;
end
B = [F,B];

for i = 1:1:n;
G(i,:) = i;
end
D = [G,D,G];

m = m + 1;
n = n + 1;

%Generate BEASY input file
fid3 = fopen('BEASY_input_file_5barop.txt','w+');
fprintf(fid3,'BEASY %s\n',datestr(now));
fprintf(fid3,'SOLUTION TYPE TE\n');
fprintf(fid3,'FILE ACCESS AND STORAGE\n');

```

```

fprintf(fid3,'DIRECT\n');
fprintf(fid3,'DELETE\n');
fprintf(fid3,'SEQUENTIAL ACCESS SOLUTION FILE 2\n');
fprintf(fid3,'DIRECT ACCESS SOLUTION FILE 2\n');
fprintf(fid3,'SOLUTION CONTROL\n');
fprintf(fid3,'ALL ALL\n');
fprintf(fid3,'PARALLEL SOLVER MEMORY WORDS 16000000\n');
fprintf(fid3,'PARALLEL SOLVER NUMBER THREADS 1\n');
fprintf(fid3,'BLOCK SIZE 81\n');
fprintf(fid3,'NEXT ID FOR NEW ELEMENTS %g\n',n);
fprintf(fid3,'NEXT ID FOR NEW MESH POINTS %g\n',m);
fprintf(fid3,'NEXT ID FOR NEW INTERNAL POINTS 1\n');
fprintf(fid3,'PRODUCE PRINTOUT ALL\n');
fprintf(fid3,'VERIFY DATA TYPES\n');
fprintf(fid3,'ALL\n');
fprintf(fid3,'ELEMENT RESULT POSITION CODE 2\n');
fprintf(fid3,'AVERAGE MESH POINT RESULTS\n');
fprintf(fid3,'LOAD AND B COND SET 1\n');
fprintf(fid3,'GENERAL DATA\n');
fprintf(fid3,'TITLE\n');
fprintf(fid3,'Metal plate stress analysis\n');           %define model title
fprintf(fid3,'MESH POINT COORDINATES\n');
[m,n] = size(B);
for i=1:1:m;
fprintf(fid3,'%g  %.7E %.7E %.7E\n',B(i,:));
end
fprintf(fid3,'DEFINE ZONE 1\n');
fprintf(fid3,'THREE DIMENSIONAL\n');
fprintf(fid3,'ZONE ELEMENTS\n');
fprintf(fid3,'MASTER\n');
[m,n] = size(D);
for i=1:1:m;
fprintf(fid3,'T3  %g %g %g %g %g %g %g %g\n',D(i,:));
end
fprintf(fid3,'LOADING DATA\n');
fprintf(fid3,'LOAD SET 1\n');
fprintf(fid3,'DEFINE BOUNDARY AND INTERFACE CONDITIONS\n');
[m,x] = size(W);
[n,y] = size(Q);
%DISPLX
for i=1:1:m;
fprintf(fid3,'DISPLX1 %g  %.7E %.7E %.7E\n          %.7E %.7E %.7E\n',W(i,:));
fprintf(fid3,'DISPLX2 %g  %.7E %.7E %.7E\n          %.7E %.7E %.7E\n',W(i,:));
fprintf(fid3,'DISPLX3 %g  %.7E %.7E %.7E\n          %.7E %.7E %.7E\n',W(i,:));
end
%TRAC

```

```

for i=1:1:n;
fprintf(fid3,'TRACTX3 %g  %.7E %.7E %.7E\n          %.7E %.7E %.7E\n',Q(i,:));
end
fprintf(fid3,'ZONE PROPERTIES\n');
fprintf(fid3,'ZONE ID 1\n');
fprintf(fid3,'YOUNGS MODULUS %.7E\n',E);
fprintf(fid3,'POISSONS RATIO %.7E\n',v);
fprintf(fid3,'END LOAD SET\n');
fprintf(fid3,'END\n');
fclose('all');

```

### Appendix 3 BEASY Input File

```

BEASY 22-Jul-2010 20:15:58
SOLUTION TYPE TE
FILE ACCESS AND STORAGE
DIRECT
DELETE
SEQUENTIAL ACCESS SOLUTION FILE 2
DIRECT ACCESS SOLUTION FILE 2
SOLUTION CONTROL
ALL ALL
PARALLEL SOLVER MEMORY WORDS 16000000
PARALLEL SOLVER NUMBER THREADS 1
BLOCK SIZE 81
NEXT ID FOR NEW ELEMENTS 1369
NEXT ID FOR NEW MESH POINTS 2739
NEXT ID FOR NEW INTERNAL POINTS 1
PRODUCE PRINTOUT ALL
VERIFY DATA TYPES
ALL
ELEMENT RESULT POSITION CODE 2
AVERAGE MESH POINT RESULTS
LOAD AND B COND SET 1
GENERAL DATA
TITLE
Metal plate stress analysis
MESH POINT COORDINATES
1  1.0577252E-002 1.6570467E-003 4.2195889E-002
2  1.3819000E-002 3.3469591E-004 5.4063801E-002
3  8.2271223E-003 1.1145715E-002 3.6848869E-002
4  2.2464199E-002 8.6691505E-004 5.4063801E-002
5  2.4424101E-002 6.1756001E-003 5.4063801E-002
6  1.3125664E-002 1.4904076E-004 4.1458000E-002
7  8.8354111E-003 1.2253015E-002 2.2862759E-003

```

8 7.0941086E-003 1.3654500E-002 1.2522176E-004  
9 3.2878284E-002 8.3481674E-003 2.6470882E-002  
10 8.2007132E-003 4.7305031E-003 3.2363270E-002

.  
.  
.

DEFINE ZONE 1  
THREE DIMENSIONAL  
ZONE ELEMENTS  
MASTER

T3 1 157 490 103 687 688 689 1  
T3 2 157 75 490 690 691 687 2  
T3 3 490 473 103 692 693 688 3  
T3 4 103 411 157 694 695 689 4  
T3 5 157 582 75 696 697 690 5  
T3 6 75 553 490 698 699 691 6  
T3 7 490 553 473 699 700 692 7  
T3 8 473 286 103 701 702 693 8  
T3 9 103 364 411 703 704 694 9  
T3 10 411 333 157 705 706 695 10

.  
.  
.

LOADING DATA  
LOAD SET 1

DEFINE BOUNDARY AND INTERFACE CONDITIONS

DISPLX1 538 0.0000000E+000 0.0000000E+0000.0000000E+000  
0.0000000E+000 0.0000000E+0000.0000000E+000  
DISPLX2 538 0.0000000E+000 0.0000000E+0000.0000000E+000  
0.0000000E+000 0.0000000E+0000.0000000E+000  
DISPLX3 538 0.0000000E+000 0.0000000E+0000.0000000E+000  
0.0000000E+000 0.0000000E+0000.0000000E+000  
DISPLX1 539 0.0000000E+000 0.0000000E+0000.0000000E+000  
0.0000000E+000 0.0000000E+0000.0000000E+000  
DISPLX2 539 0.0000000E+000 0.0000000E+0000.0000000E+000  
0.0000000E+000 0.0000000E+0000.0000000E+000  
DISPLX3 539 0.0000000E+000 0.0000000E+0000.0000000E+000  
0.0000000E+000 0.0000000E+0000.0000000E+000  
DISPLX1 540 0.0000000E+000 0.0000000E+0000.0000000E+000  
0.0000000E+000 0.0000000E+0000.0000000E+000  
DISPLX2 540 0.0000000E+000 0.0000000E+0000.0000000E+000  
0.0000000E+000 0.0000000E+0000.0000000E+000  
DISPLX3 540 0.0000000E+000 0.0000000E+0000.0000000E+000  
0.0000000E+000 0.0000000E+0000.0000000E+000  
DISPLX1 541 0.0000000E+000 0.0000000E+0000.0000000E+000  
0.0000000E+000 0.0000000E+0000.0000000E+000

```

DISPLX2 541  0.000000E+000 0.000000E+0000.000000E+000
              0.000000E+000 0.000000E+0000.000000E+000
DISPLX3 541  0.000000E+000 0.000000E+0000.000000E+000
              0.000000E+000 0.000000E+0000.000000E+000
.
.
.
NORMALTRAC 1  1.0003197E+005 1.3894788E+005 1.3100294E+005
              1.1909064E+005 1.3497541E+005 1.1530354E+005
NORMALTRAC 2  1.0003197E+005 1.3377857E+005 1.3894788E+005
              1.1662659E+005 1.3636322E+005 1.1909064E+005
NORMALTRAC 3  1.3894788E+005 1.8069914E+005 1.3100294E+005
              1.5922852E+005 1.5483319E+005 1.3497541E+005
NORMALTRAC 4  1.3100294E+005 8.8499364E+004 1.0003197E+005
              1.0942217E+005 9.4265665E+004 1.1530354E+005
NORMALTRAC 5  1.0003197E+005 9.3843166E+004 1.3377857E+005
              9.6937566E+004 1.1347044E+005 1.1662659E+005
NORMALTRAC 6  1.3377857E+005 1.8416861E+005 1.3894788E+005
              1.5802644E+005 1.6088622E+005 1.3636322E+005
NORMALTRAC 7  1.3894788E+005 1.8416861E+005 1.8069914E+005
              1.6088622E+005 1.8243387E+005 1.5922852E+005
NORMALTRAC 8  1.8069914E+005 1.7404745E+005 1.3100294E+005
              1.7737329E+005 1.5165502E+005 1.5483319E+005
NORMALTRAC 9  1.3100294E+005 1.2643956E+005 8.8499364E+004
              1.2872125E+005 1.0724694E+005 1.0942217E+005
NORMALTRAC 10 8.8499364E+004 6.5725916E+004 1.0003197E+005
              7.6011455E+004 8.1043137E+004 9.4265665E+004
.
.
.
ZONE PROPERTIES
ZONE ID 1
YOUNGS MODULUS 2.1000000E+011
POISSONS RATIO 3.0000000E-001
END LOAD SET
END

```

**Appendix 4      Paper Published in International Conference  
on Manufacturing Research 2010**

**AN APPLICATION OF FREEFORM SURFACE MODELLING  
BY LASER SCANNING TECHNIQUE AND REVERSE ENGINEERING**

Bing Ru Yang  
Qing Wang  
Jon Trevelyan  
Roger S. Crouch

Durham University  
School of Engineering and Computing Sciences  
Science Laboratories, South Road  
Durham, DH1 3LE, UK

**ABSTRACT**

Freeform shaped parts have played an important role in many applications. These parts are difficult to measure by conventional measurement techniques. With the rapid development of laser scanning technique, reverse engineering has become an effective tool to meet these demands. This paper presents a method of applying a laser scanning technique and reverse engineering in freeform surface measurement and modelling, particularly in turbine blade modelling. The entire process comprises surface digitizing, point clouds pre-processing and surface model reconstruction. A rapid prototyped model was produced, and the measurement error analyzed in this research.

Keywords: laser metrology, reverse engineering, blade geometry modelling, freeform surfacing

**1 INTRODUCTION**

Freeform shaped parts are of great interest in many applications, either for functional or aesthetical reasons. Their relevance for industry is well-known in the design and manufacturing of products having complex functional surfaces. These parts are important components in industries such as automotive, aerospace, household, consumer products and others. However, with highly complex and freeform shaped parts being used in industry more and more, the conventional measurement machine is insufficient to meet the measurement demand of both accuracy and time-saving. Therefore, the reverse engineering (RE) technique was widely recognized and became a strong tool which meets the demands of freeform surface measurement.

The design of a turbine blade plays a crucial role in turbine technology for obtaining reliable machine performance. Over the years, many efforts have been made to improve turbine efficiency; finite element analyses (FEA) based on existing turbine CAD models have been developed to calculate the stress concentrations which could lead to low cycle thermal fatigue. The energy transfer from the steam to the rotor was also improved. All of these indicate that the blade geometry has a great effect on turbine performance. For this reason, RE of a turbine blade plays a crucial role in reconstructing the geometry and improving the blade performance. Figure 1 shows a typical use of RE in the blade design cycle (Chen and Lin, 2000).

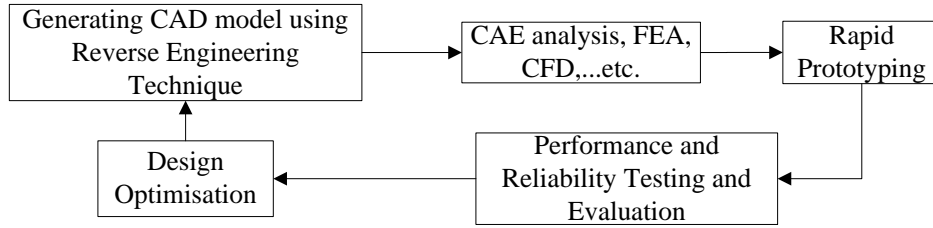


Fig 1: RE in turbine blade design cycle

Several authors have applied RE to freeform surface measuring and modelling in different areas. Sansoni and Docchio (2004) described a special example of applying optical measurement and reverse engineering to generate the surface model of automotive components. Lin, Wang and Dai (2005) used a contact measurement method and reverse engineering technique to reconstruct the CAD model of an artificial joint in order to meet their customized demands. Xu and Lin (2008) presented a novel application of RE in bionic research to model a wild boar head for a biomimetics study of the ridger and Chen and Lin (2000) reported an early study of RE to extract the geometry of a turbine blade.

A review of published literature reveals that very few studies have been made on freeform shaped part measurement and modelling, especially the turbine blade. The mesh and surface images (and their error) lacked detail and no scanning reliability and stability were given. This paper presents a method of applying a laser scanning technique and reverse engineering in freeform surface measurement, particularly in turbine blade modelling. The measurement quality and the stability and reliability of the scan process were investigated. The surface information was captured by a Leica LR-200 laser radar and the surface was reconstructed by using RE software Rapidform.

The entire process comprises surface digitizing, point clouds pre-processing and surface model reconstruction. A rapid prototyped model was produced, and the measurement error analyzed in this research. Figure 2 shows a turbine blade used as a case study of three dimensional freeform surface modelling by RE.



Fig 2: Sample turbine blade

An overview of the measurement process is shown in Figure 3, starting from capturing the surface information of the blade by a laser scanning technique, then point cloud filtering and alignment was carried out in the Spatial Analyzer software, and finally the CAD model was reconstructed in Rapidform XOS and Solidworks environments.

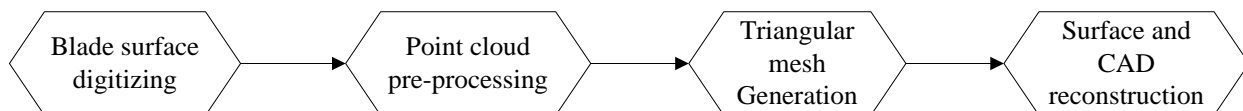


Fig 3: Overview RE process of turbine blade

## 2 EXPERIMENTAL APPROACH

### 2.1 Surface digitization

In RE, the quality of the data acquisition process is crucial to the accuracy of the resulting CAD model. There are many methods to capture the geometric information of a part. These methods can be divided into two types: contact and non-contact method. Sacio and De Chiffre (2007) presented a detailed conclusion of the state of the art in the metrology of freeform shapes with focus on the freeform capabilities of the most important measuring techniques.

The measurement process was carried out using the Leica LR-200 laser radar. The LR-200 uses coherent laser radar technology to measure the distance precisely from the mirror of the instrument to the surface point on which the laser is focused. The laser radar beam is directed using a mirror mounted on two axes, which moves the beam in the horizontal and vertical directions. The beam is focused to the smallest possible spot by a high-speed optical device. The measurement range of this system is 1-25 metres, the maximum scan speed is 1000 pts/s in Pseudo Vision Mode. The scan errors based on absolute range are:  $\pm 0.025\text{mm}$  between 0.3 to 10m, and  $\pm 2.5\text{ppm}$  when the range exceeds 10m (LR-200 system guide). The resolution can be changed on both point spacing and line spacing. The system integration is shown in Figure 4.

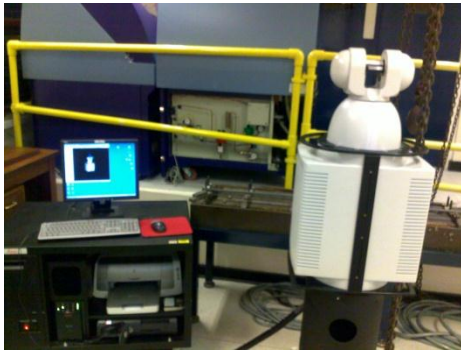


Fig 4: LR-200 measurement system

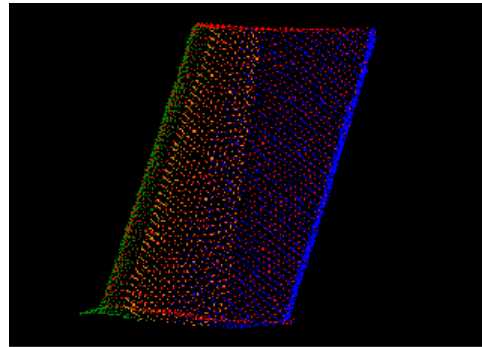


Fig 5: Alignment of 5 point clouds

Three sample point clouds were obtained at resolutions of  $0.5 \times 0.5\text{mm}$ ,  $1 \times 1\text{mm}$  and  $2 \times 2\text{mm}$  respectively on both point spacing and line spacing during measurement.

### 2.2 Point cloud alignment

In order to digitize the entire surface of the turbine blade, the model was rotated and scanned five times from different angles. The blade cannot be scanned in just one setup to obtain the full surface information, since it has a complex geometry with hidden surfaces when viewing in one direction. The point clouds captured from different locations were aligned with the method of three-point best-fit. A reference tooling ball was used here. The position of the centre of the tooling ball was determined, knowing the ball's radius. The turbine blade was surrounded by three such tooling balls. These balls' coordinates reflect the information of relative position in different locations. The tooling balls were measured on the first blade position and set these tooling balls as reference group. Once the scan had been completed on the first position, the laser radar was moved to the second position. The tooling balls need to be scanned again on each new position of the laser radar.

After finishing all the scans, the different views of the point cloud were aligned by translating these tooling balls to the reference group by the relative position. The combined point clouds are shown in Figure 5 (point cloud 1 – green, point cloud 2 – orange, point cloud 3 – red, point cloud 4 – blue, point cloud 5 – purple), and the error in each alignment is shown in Table 1.

Table 1 : Point cloud alignment error based on 1mm resolution

Best-fit transformation	Align 1	Align 2	Align 3	Align 4
Max error (mm)	0.0090	0.0043	0.0089	0.0119
RMS error (mm)	0.0066	0.0034	0.0064	0.0091
StdDev error (mm)	0.0080	0.0041	0.0079	0.0111

RMS error: Root mean square error; StdDev error: Standard deviation error.

### 2.3 Point cloud pre-processing

Point cloud pre-processing is the key stage before generating a good quality surface model, as the initial scanned data usually contain spikes, outliers and poor quality regions. These noisy data directly affect the surfacing quality and they are also the major contributor to large errors. Thus the poor quality points need to be removed at the earliest opportunity. In this work, the points were removed by an automatic function in the Rapidform XOS software. Any points exhibiting a small error, which were hard to detect automatically, were deleted manually.

### 2.4 Mesh generation and surface reconstruction

There are two ways to create the surface from the measurement data using freeform feature modelling: the curve method and the surface method (Zhang, 2003). In the first method the curves are generated from measurement data first, and then the surface can be created through the construction curve mesh generated. In the second method the surface is generated directly from the measurement data based on mesh generation.

The reverse engineering software Rapidform XOS was employed to reconstruct the NURBS surface model of the turbine blade. The procedure was as follows:

1. An initial mesh was constructed that roughly represents the blade geometry.
2. From the initial mesh, optimized triangular meshes were generated with an adaptive algorithm based on curvature and multiple density settings.
3. A NURBS surface was constructed with variable surface number setting and control point setting. The NURBS surfaces were generated based on a 0.5×0.5mm resolution point cloud, a 1×1mm resolution point cloud and a 2×2mm resolution point cloud separately. The whole surface geometry of the turbine blade could not be generated with the 2×2mm resolution point cloud as it lacked sufficiently detailed point information. Both the 0.5×0.5mm resolution point cloud and 1×1mm resolution point cloud generated surfaces which represented the fine geometry of the blade. The triangular mesh result and a fitted NURBS surface based on 1×1mm resolution point cloud are shown in Figure 6 and Figure 7.

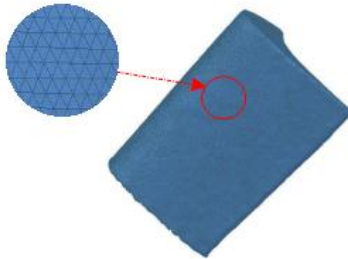


Fig 6: Mesh construction



Fig 7: 8-control point NURBS surface

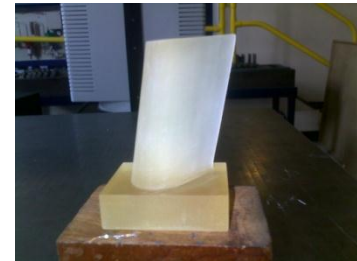


Fig 8: Rapid prototyped model

After getting the NURBS surface model of the turbine blade, a 1:1 scaled rapid prototyped model of turbine blade obtained from 1×1 mm resolution point cloud with 8-control points surfacing was produced (shown in Figure 8), this rapid prototyped model was used for a repeatability test later in this research. The duration of each process of the experiment shows in Table 2.

Table 2 : Duration of each process in the reverse engineering of turbine blade

Resolution	0.5×0.5mm	1×1mm	2×2mm
Surface scanning and point clouds alignment	21.5 min	14.85 min	9.5min
Point clouds pre-processing and mesh generation	12 min	8 min	5min
Surface reconstruction (5-control points)	5 min	4 min	N/A
Surface reconstruction (8-control points)	6 min	4.5 min	N/A
Surface reconstruction (12-control points)	8 min	7 min	N/A
Rapid prototyping	N/A	200 min	N/A
Total	N/A	238.35 min	N/A

### 3 SURFACE QUALITY ANALYSIS

In order to evaluate the quality of the surface model of the turbine blade in this research, three NURBS surface models were generated with 5,8 and 12 control points setting using a 1mm resolution point cloud in Rapidform XOS. A deviation map (shown in figure 9) shows the distance between the 1×1mm point cloud and the 5-control points surfacing result. In the 5 control-points model, 90% of the NURBS surface deviations are within ±0.04mm, 70% within ±0.01mm. The quality of the NURBS surfaces is much better in the 8 control-points model. Here, 90% of the NURBS surface deviations are within ±0.02mm, 80% within ±0.01mm. In the 12 control-points model, the surface quality was still high but the simulation time was more than three times that the 8 control-points model and here the NURBS surface quality only slightly increased.

### 4 REPEATABILITY OF THE SCAN PROCESS

In order to test the accuracy and variation of the scanning process, the rapid prototype model of the blade was scanned repetitively under the same resolution setting. The resolution was set to 1mm on point spacing and 1mm on line spacing. The five samples of the point cloud were fitted to the same surface model respectively, and then the errors between each sample point cloud and the CAD model were analyzed. The colour deviation map between the first scanned sample of point cloud and the surface model of the blade is shown in Figure 10, and the full error distribution of five scanned samples is listed in Table 3.

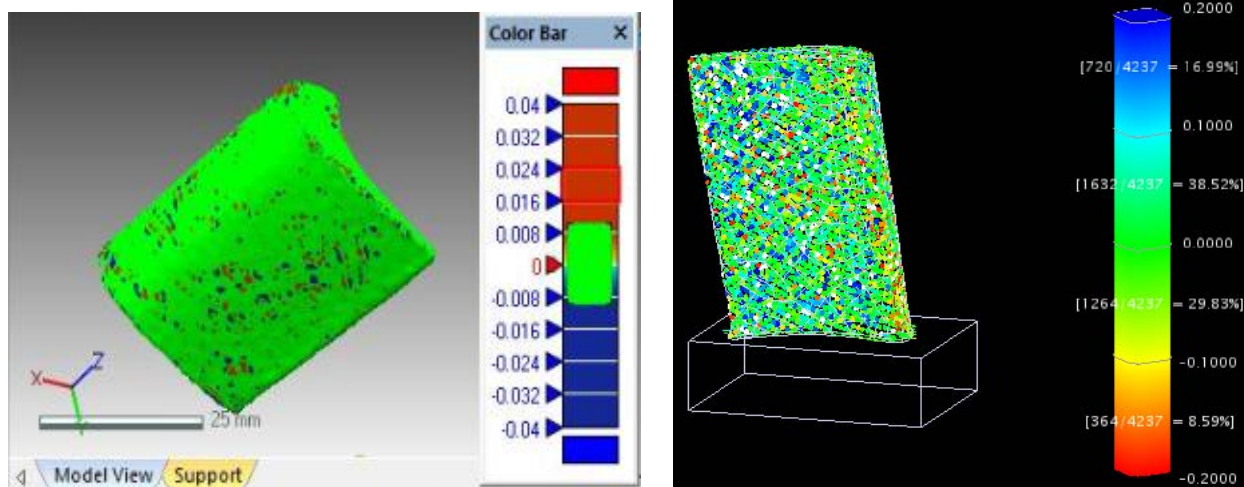


Fig 9 (left): Deviation map of 5-control points surfacing result  
 Fig 10 (right): Deviation map between point cloud and the CAD model

Table 3: Error distribution of five scanned samples

Measurement results	Number of points	Points within tolerance range of $\pm 0.2\text{mm}$	Points within tolerance range of $\pm 0.1\text{mm}$	Standard deviation (mm)	Max error (mm)
Scan 1	4237	93.93%	68.35%	0.10	0.61
Scan 2	4134	95.72%	68.51%	0.11	0.44
Scan 3	4154	93.62%	67.89%	0.11	0.54
Scan 4	4148	92.87%	66.83%	0.11	0.71
Scan 5	4195	94.00%	70.39%	0.11	0.89

The result shows the maximum errors of the five scans are more than twice that for the normal tolerance range. There are many reasons that are likely to have caused these errors during data acquisition, such as machine calibration, measurement accuracy, noisy data, alignments of multiple views (Varady and Martin, 1996). Some alignment errors cannot be avoided. However, as the results have shown, the alignment errors in this research are negligibly small. After checking the sample point clouds, it was found that the major problem causing the maximum error was noise in the data. These noisy data are difficult to detect and delete completely using an automatic function in the software. Manually removing those points is time consuming.

## 5 CONCLUSION

In this paper, a novel study into rapid and complete turbine blade modelling by using laser radar and Rapidform XOS was presented. The methodology and the experimental process were described. The blade surface model was obtained within 4 hours. The results show that the point clouds obtained from a laser scanning technique is rapid and maintains a high accuracy. The modelling surface generated in Rapidform XOS is in good agreement with the point clouds. In a test of the repeatability of the process, more than 65% points are found to be within the tolerance range of  $\pm 0.1\text{mm}$  and more than 90% points are within  $\pm 0.2\text{mm}$ , which shows the laser scanning technique is stable and accurate.

The method demonstrated in this research can be successfully applied in freeform model reconstruction of a good quality in a short time. These freeform models generated by the method shown in this work can be applied to further CAE analysis, such as manufacturing quality inspection, finite element analysis and computational fluid dynamic analysis for product redesign and performance improvement. These can bring benefits such as reducing the design lead time and cost.

## REFERENCES

- Chen, L. C., and G. C. I. Lin. 2000. Reverse engineering in the design of turbine blades – a case study in applying the MAMDP. *Robotics and Computer-Integrated Manufacturing* 16: 161-167.
- Lin, Y. P., C. T. Wang, and K. R. Dai. 2005. Reverse engineering in CAD model reconstruction of customized artificial joint. *Medical Engineering & Physics* 27: 189-193.
- LR-200 system guide. 2004. Leica Geosystems, UK.
- Sacio, E., L. De Chiffre, and R. Schmitt. 2007. Metrology of freeform shaped parts. *Annals of the CIRP – Manufacturing Technology* 56, 2: 810-835.
- Sansoni, G., and F. Docchio. 2004. Three-dimensional optical measurements and reverse engineering for automotive applications. *Robotics and Computer-Integrated Manufacturing* 20: 359-367.
- Varady, T., R. R. Martin, and J. Cox. 1996. Reverse engineering of geometric models – an introduction. *Computer Aided Design* 29, 4: 255-268.
- Xu, L., M. X. Lin, J. Q. Li, Z. L. Wang, and B. Chirende. 2008. Three-dimensional geometrical modelling of wild boar head by reverse engineering technology. *Journal of Bionic Engineering* 5: 85-90.
- Zhang, Y. 2003. Research into the engineering application of reverse engineering technology. *Journal of Material Processing Technology* 139: 472-475.